Volatile signatures in the Sudbury Igneous Complex magmatic Ni-Cu-PGE deposits: Implications for sulfide melt differentiation and precious metal mineralization

Kelsie Ojaste

A thesis submitted to the University of Ottawa
in partial fulfillment of the requirements for the
Master of Science in Earth Sciences

Department of Earth and Environmental Sciences
Faculty of Science
University of Ottawa

uOttawa

© Kelsie Ojaste, Ottawa, Canada, 2025

Abstract

The offset dykes of the Sudbury Igneous Complex (Ontario, Canada) host significant magmatic Ni-Cu-PGE deposits rich in precious metals (e.g., platinum-group elements, gold), making them superlative sites for understanding metal solubility in fluids and magmatic sulfide differentiation. Despite extensive study, the origin(s) and character of volatile components and their impact on precious metal distribution in the Sudbury sulfide ores remain controversial. Here we aim to evaluate the evidence for volatile activity in differentiated sulfide ores from the distal Podolsky North Zone in the Whistle offset dyke, at the northeast margin of the Sudbury Igneous Complex. We have examined a ~43 cm long channel-cut section, including massive sulfide, chloritic alteration/reaction rim and host gneiss, across the margin of a ~2 m thick sulfide vein. Our integrated analytical approach includes utilizing optical petrography, mineral chemistry (by scanning electron microscopy and microprobe) and stable sulfur isotope measurements.

Petrographic observations revealed a diverse mineralogy of aggregated platinum-group minerals, and accessory Ag±Bi tellurides within the chalcopyrite-dominated sulfide vein material. Fractured surfaces from the interior of the vein expose decrepitated fluid inclusions, observed as salt evaporate haloes (evaporated 'liquid' phase), together with solid halides and ferropyrosmalite [$(Fe^{2+},Mn)_8Si_6O_{15}(OH,Cl)_{10}$] daughter phases. It is noteworthy that there is trace Pd present in a few of the halides, and chlorargyrite (AgCl) is commonly observed associated with the fluid inclusions. Epidote occurs in separate parallel bands within the vein, interpreted to have formed late in the veins crystallization history or during a later regional hydrothermal event. Chlorite exhibits a minor decrease in Fe-Ni concentrations away from the vein. Sulfur isotope measurements (on chalcopyrite) indicate relatively heavy but homogeneous $\delta^{34}S$ compositions within the vein and chloritic rim and host rock.

Our findings suggest that chloride complexation played a key role in the localization and enrichment of precious metals within the highly differentiated sulfides in the Podolsky North Zone. By providing new insights into the relationship between volatile components, metal solubility and fluid chemistry, this study contributes to broader models of magmatic-hydrothermal systems, with potential applications for guiding exploration for precious metal-enriched deposits.

Acknowledgements

Foremost, I thank my supervisor, Dr. Brian O'Driscoll who initiated this project and provided their guidance and detailed feedback throughout. Brian's patience and openness allowed me to take the time I needed to understand the complexities of this subject and work through more unconventional ideas.

We thank Dr. Michael Lesher, Dr. Jacob Hanley, and Dr. Patricia Clay for their assistance in proposing this project to gain funding. I thank Dr. Lesher at Laurentian University for coordinating with KGHM in Sudbury to grant access to the Podolsky North property and detailed comments. I am grateful to Dr. Hanley at Saint Mary's University for their assistance and discussions in understanding fluid inclusions and the fluid chemistry of Sudbury sulfides. I also appreciate Dr. Clay for helping prepare samples for NI-NGMS for a future project.

Finally, I thank my friends and family who supported me during the completion of this thesis.

Table of Contents

Statement of Research Contributions

Results from this thesis are currently in preparation for submission to the *Journal of Petrology* or *The Canadian Journal of Mineralogy and Petrology* a multi-author manuscript. The author, Kelsie Ojaste, wrote all text, drafted all figures and performed all calculations relating to the analyses presented here. Dr. Brian O'Driscoll aided with the formulation of ideas and provided edits on the document's drafts. Dr O'Driscoll, along with the Targeted Geoscience Initiative (TGI) Grant program with Natural Resources Canada, provided the funding for the project. Dr. Michael Lesher of Laurentian University, Dr. Jacob Hanley of Saint Mary's University, and Dr. Patricia Clay of Manchester University assisted in proposing the project to TGI. Dr. Lesher coordinated with KGHM to grant entry to the Podolsky North property for sampling and reviewed the document's draft. Dr. Hanley provided access to their laboratory in Halifax and offered guidance on interpreting fluid inclusion chemistry. Dr. Clay assisted in preparing samples for NI-NGMS analysis. Additional contributions from the University of Ottawa were from Glenn Poirier in operating the microprobe, and Dr. Paul Middlestead in overseeing the stable isotope analyses.

1. Introduction

The Sudbury Igneous Complex (SIC) represents one of Earth's most important natural laboratories for investigating magmatic Ni-Cu-platinum-group element (PGE) sulfide ore systems (Naldrett, 2004; Lightfoot, 2016). Its significance lies not only in its immense economic importance – contributing substantially to Canada's nickel and PGE production – but also in its unique and complex magmatic and hydrothermal origin and evolution. The SIC hosts several styles of sulfide mineralization, including contact-type massive sulfide ores and footwall-type vein and disseminated ores, providing an exceptional record for examining the processes that govern ore formation. Although the initial segregation and accumulation of magmatic sulfide melts are relatively well understood (e.g., Dare et al., 2014; Mansur et al., 2021), the role of volatile loss during sulfide differentiation, particularly the fractionation and redistribution of halogens (Cl, Br, I), remains underexplored, despite its potential influence on ore tenor and base- and precious-metal zoning (Fleet and Wu, 1993; Hanley et al., 2005; Tuba et al., 2014).

Previous studies have identified alkali- and halogen-enriched alteration haloes around footwall-type sulfide ores in the SIC (Springer, 1989; Farrow and Watkinson, 1992; Li et el., 1992; McCormick et al., 2002; Hanley and Mungall, 2003; Hanley et al., 2004), implying exsolution of alkali- and halogen- phases from sulfide melts, followed by fluid-rock interaction, played a significant role in metal mobilization and concentration. However, systematic, quantitative data on alkali and halogen behaviour during sulfide crystallization remain scarce, partly due to analytical challenges in detecting these elements at ultra-trace levels. Given the strong complexing capacity of halogens, particularly chlorine, with chalcophile and siderophile metals including the PGE (Gammons et al., 1992; Wood, 2002; Sullivan et al., 2022), understanding their partitioning among sulfide, silicate, and fluid phases is critical for reconstructing the complete magmatic-hydrothermal evolution of ore systems such as at the SIC. Despite increasing recognition of the important role of heavy halogens (Cl, Br, I; Molnar et al., 2001; Hanley and Mungall, 2003; Mungall and Brenan, 2003; Hanley et al., 2004; Hanley, 2006; Boudreau, 2016; Parker et al., 2019; Parker et al., 2022), no study has yet comprehensively quantified the partitioning of halogen during sulfide crystallization in the SIC, leaving a key gap in current ore-forming models. Any connections that can be established between halogen and volatile behaviour and mineralization, even if indirect or qualitative, therefore remain highly valuable to advancing our understanding of ore-forming processes.

This study focuses on the footwall-style mineralization of the SIC, where sulfide-rich veins, characterized by elevated Cu/Ni and Pd/Ir ratios, are interpreted to reflect internal differentiation of an initially homogeneous sulfide melt (Molnar et al., 2001; Nelles, 2012; Tuba et al., 2014; Lightfoot, 2016). When surrounded by halogen-rich alteration haloes, these deposits provide an ideal natural setting to investigate the fate of volatiles during sulfide crystallization and degassing. Specifically, that the progressive crystallization of monosulfide solid solution (MSS), intermediate

solid solution (ISS), and base-metal sulfides selectively depletes the residual melt in Cl and Br relative to I, potentially altering the melt's physical properties (e.g., density, viscosity) and its capacity to retain or expel precious metals (Mungall and Brenan, 2003; Hanley et al., 2004). While this hypothesis cannot be directly tested with the available data, this thesis will provide new constraints on the behavior of volatile phases, including potential evidence for devolatilization, and will contribute indirect insights into volatile-metal relationships through detailed petrography, mineral chemistry and sulfur isotopic signatures.

The Podolsky North Zone, situated within the Whistle Offset dyke at the northeastern margin of the SIC, offers a useful site for probing these questions. Unlike many offset dyke exposures which are obscured by overburden or surface staining, the proximal part of the Whistle dyke was stripped, pressure washed and partially sandblasted during INCO Ltd.'s reclamation of the Whistle open pit mine in the early 2000s. This process revealed exceptionally well-preserved massive sulfide veins and their host-rock interactions at the surface, providing a rare opportunity for direct field observation. Detailed mapping of these outcrops was completed and reported by Poulin et al. (2010) and Carter (2005) and has since supported numerous investigations into offset dyke formation and sulfide ore genesis (e.g., Farrow et al., 2005; Lafrance et al., 2014; MacInnis et al., 2014).

The research presented in this thesis aims to resolve outstanding questions in the petrogenesis of magmatic sulfide ore deposits, focusing particularly on the role of late stage devolatilization in driving precious metal enrichment and remobilization. Specifically, it tests the hypothesis that volatile mobility during MSS and ISS crystallization drives selective precious metal enrichment and addresses the following: (1) How do volatile-rich mineral phases vary between sulfide and silicate phases? (2) What microstructural evidence is preserved for volatile mobility? (3) How does volatile distribution correlate with observed metal zoning?

By integrating detailed petrographic and microstructural analyses of the massive sulfides, alteration haloes, and host silicate rocks with mineral chemistry and stable isotope data, this study aims to constrain the immiscible crystallization sequence, the evolution of the volatile budget, and the timing and sources of ore-mobilizing fluids at Podolsky North. Ultimately, these findings will not only advance our understanding of the SIC but also refine broader exploration models and genetic frameworks applicable to magmatic sulfide deposits globally.

2. Brief Overview of Magmatic Ni-Cu-PGE Sulfide Formation in the Sudbury Igneous Complex

The Sudbury Igneous Complex (SIC) hosts one of the world's most economically significant Ni-Cu-PGE sulfide ore systems, formed through complex magmatic and post-magmatic processes. Although early models emphasized crustal contamination and sulfide segregation during the cooling of an impact melt sheet (e.g., Hawley, 1965), more recent work has highlighted the evolving nature of sulfide melts and their interaction with volatiles, especially halogen- and sulfur-rich magmatic fluids (e.g., Farrow et al., 1994; Mungall and Brenan, 2003; Hanley and Mungall, 2003; Hanley et al., 2005). Understanding the formation and evolution of monosulfide solid solution (MSS), intermediate solid solution (ISS), and residual sulfide liquids, alongside volatiles, is critical for interpreting metal partitioning, PGE mineralization, and sulfide ore textures observed in Sudbury deposits. This section synthesizes key literature on offset dyke emplacement, sulfide liquid formation, crystallization pathways, and volatile involvement.

The formation of metal-rich sulfide mineralization in the SIC is broadly tied to early sulfide saturation in the impact melt sheet, which formed following the 1.85 Ga bolide impact that produced the Sudbury Basin (Hawley, 1965; Li and Ripley, 2005). The SIC is compositionally diverse, but dominantly noritic to granophyric, representing a differentiated impact melt sheet that assimilated Archean and Proterozoic footwall lithologies (Naldrett, 2004; Lightfoot, 2016).

Sulfide saturation was likely triggered by either the assimilation of country-rock clasts concentrated in the embayment structures by convection currents (Keays and Lightfoot, 2004), or sulfur-rich melting wall rock protores incorporating into the cooling lower melt sheet and scavenging Ni-Fe-Cu from the impact melt. The latter process reduced the sulfur solubility in the silicate melt, leading to the segregation of an immiscible sulfur-rich Fe-Ni-Cu xenomelt (Lesher, 2017). Once incorporated, the sulfide scavenged chalcophile and siderophile elements (e.g., Ni, Cu, Co, and PGE; Fig. 2.1A) from the silicate melt due to their strong partition coefficients (Keays, 1995). The xenomelt continued to upgrade along the melting base of the impact structure (Lesher, 2017). Adjustments in the footwall, caused by the cooling SIC, formed fractures that allowed early, undifferentiated quartz dioritic melt to be injected into the footwall, followed quickly by an injection of the same melt containing xenolithic inclusions and sulfide xenomelt (Therriault et al., 2002; Lightfoot et al., 1997; Pilles et al., 2022).

Fractional crystallization of the MSS from a sulfide melt was first proposed by Hawley (1965) to explain the sulfide mineralogical zoning at the Frood-Stobie deposit. Subsequent studies built on Hawley's work to incorporate ISS crystallization (e.g., Keays and Crocket, 1970; Chyi and Crocket, 1976; Li et al., 1992), the effects of circulating hydrothermal fluids in footwall rocks (e.g., Farrow and Watkinson, 1992; Molnar et al., 2001), and early movement of precious metals as a fluid into the footwall (Farrow and Lightfoot, 2002; Hanley et al., 2005). The crystallization

processes described below integrate and build on these studies to provide a broad overview of fractional crystallization in the offset dykes.

The sulfide melt, once separated from the silicate melt, underwent fractional crystallization as the system cooled (Hawley, 1965). Crystallization of MSS is envisaged to begin at high temperatures (typically above ~1100°C), forming a Fe-Ni-rich phase that preferentially sequesters Ni, Co, and iridium-group PGEs (IPGEs: Os, Ir, Ru) into early forming pyrrhotite and pentlandite (e.g., Li et al. 1996; Mungall, 2005; Ballhaus et al., 2001; Mansur et al., 2021). The crystallization of MSS in the contact deposits preferentially removed these elements from the sulfide melt, allowing for subsequent fractionation of the remaining melt (Fig. 2.1B).

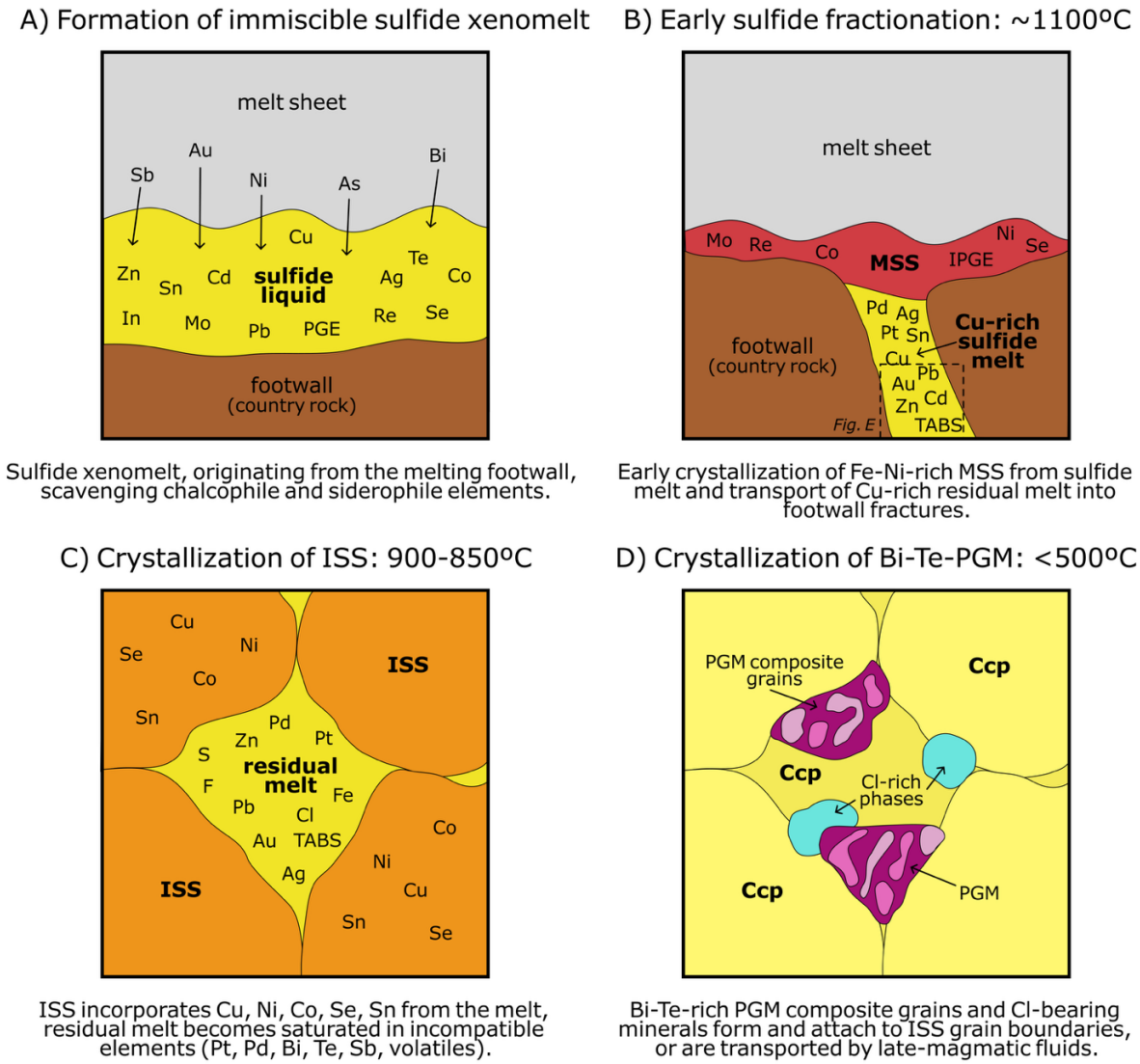

Figure 2.1 Simplified schematic model for the crystallization history of the MSS and ISS ore in the Sudbury Igneous Complex offset dykes. Figure A) shows the upgrading of the sulfide xenomelt, and B) to D) shows the fractionation processes of MSS to ISS and residual melt. Based on Lesher (2017), Dare et al. (2014), and Mansur et al. (2021).

The ISS appears to crystallize once the melt reaches ~32 wt.% Cu saturation (Dutrizac, 1976; Naldrett et al., 1997), and at lower temperatures (~900-1000°C), preferentially incorporates Cu, Ni, Co, Se, Sn and IPGEs, leaving a melt that is further enriched in Cu, Pt, Pd, Bi, Te, Sb (Fig. 2.1C; Nelles, 2012; Mansur et al., 2021) and volatiles such as Cl and F (Dare et al., 2014). As MSS and ISS sequentially crystallize, the remaining sulfide melt becomes progressively enriched in incompatible elements (Fig. 2.1C; Mungall et al., 2005; Dare et al., 2014). The composition of this residual melt plays a key role in forming discrete platinum-group minerals (PGM), many of which precipitate directly from the late-stage melt or from fluid phases exsolving from it (Mansur et al., 2021).

PGM such as Pd-Te-Bi minerals often form in low-temperature conditions (<500°C) from evolved sulfide melts or sulfide-bearing fluids (Fig. 2.1D; Dare et al., 2014). The exact timing and mechanism of PGM formation remains debated, but many studies emphasize the link to fluid activity, particularly halogen-rich fluids that can remobilize and reprecipitate the PGE within discrete phases (Farrow and Lightfoot, 2002; Mungall and Brenan, 2003).

Many workers have highlighted the importance of volatiles and halogens in the evolution of magmatic sulfides at Sudbury (e.g., Molnar et al., 2001; Mungall and Brenan, 2003; Hanley et al., 2011). Fluid inclusions within sulfide-associated silicates and the occurrence of halogen-bearing minerals (e.g., amphibole, biotite, apatite) suggest the presence of late-magmatic to magmatic-hydrothermal fluids. Most fluid-related studies have focused on disseminated sulfides of the Sudbury and footwall breccias and metabreccia to determine fluid origins in the North Range footwall deposits, specifically in the McCreedy deposits and Strathcona Deep Copper Zone (Farrow and Watkinson, 1996; Hanley et al., 2004; Hanley et al., 2011), often neglecting the enriched sulfide melt zones in the offset dykes.

Halogens such as Cl are known to partition preferentially into sulfide melts as exsolving magmatic fluids where they can form stable metal-halide complexes with Pt and Pd (Mungall and Brenan, 2003; Sullivan et al., 2022). The experimental studies demonstrated that these metal-halide complexes significantly enhance the solubility and transport capacity of the PGE in magmatic fluids. The interaction between sulfide melts and exsolving fluid can induce local re-equilibration, remobilization, or enrichment of metals, particularly the PGE, at relatively low temperatures.

Similar fluid-related mechanisms have been proposed for other magmatic Ni-Cu-PGE deposits, including those in the Bushveld Complex (Ballhaus and Stumpfl, 1986; Kanitpanyacharoen and Boudreau, 2013), Stillwater Complex (Hanley et al., 2008; Boudreau, 2016), and Noril'sk-Talnakh mining district (Wood, 2002; Duran et al., 2017). These systems provide useful analogs for understanding volatile-metal behavior and post-magmatic modification of sulfide ores in Sudbury.

Understanding the timing, evolution, and interaction of MSS, ISS, and residual sulfide liquid – together with the activity of late-stage halogen-bearing fluids – is essential for interpreting the formation and modification of Ni-Cu-PGE ores in Sudbury. The partitioning behavior of metals and volatiles during sulfide crystallization sets the initial metal budget, but subsequent fluid involvement may redistribute, concentrate, or modify sulfide assemblages and PGM mineralogy.

3. Sudbury Geological Setting

3.1 Archean North Range Country Rock

The 1.85 Ga elliptically shaped Sudbury Structure is located between the Paleoproterozoic Southern Province (2.5 Ga) and the northern Archean Superior Province (2.7 Ga) in southern Ontario (SS, Fig. 3.1.1; Dressler, 1984; Grieve et al., 1991). The North Range's Archean country rocks, mainly the Levack Gneiss Complex (LGC), include gneisses, tonalites, granodiorites, as well as ultramafic to anorthositic intrusions metamorphosed to upper amphibolite-lower granulite facies (Card, 1994; Wodicka, 1997), with U-Pb zircon ages of 2711 ± 7 Ma and 2657 ± 3 Ma reported for the tonalitic gneisses and the leucosome layers, respectively (Krogh et al., 1984).

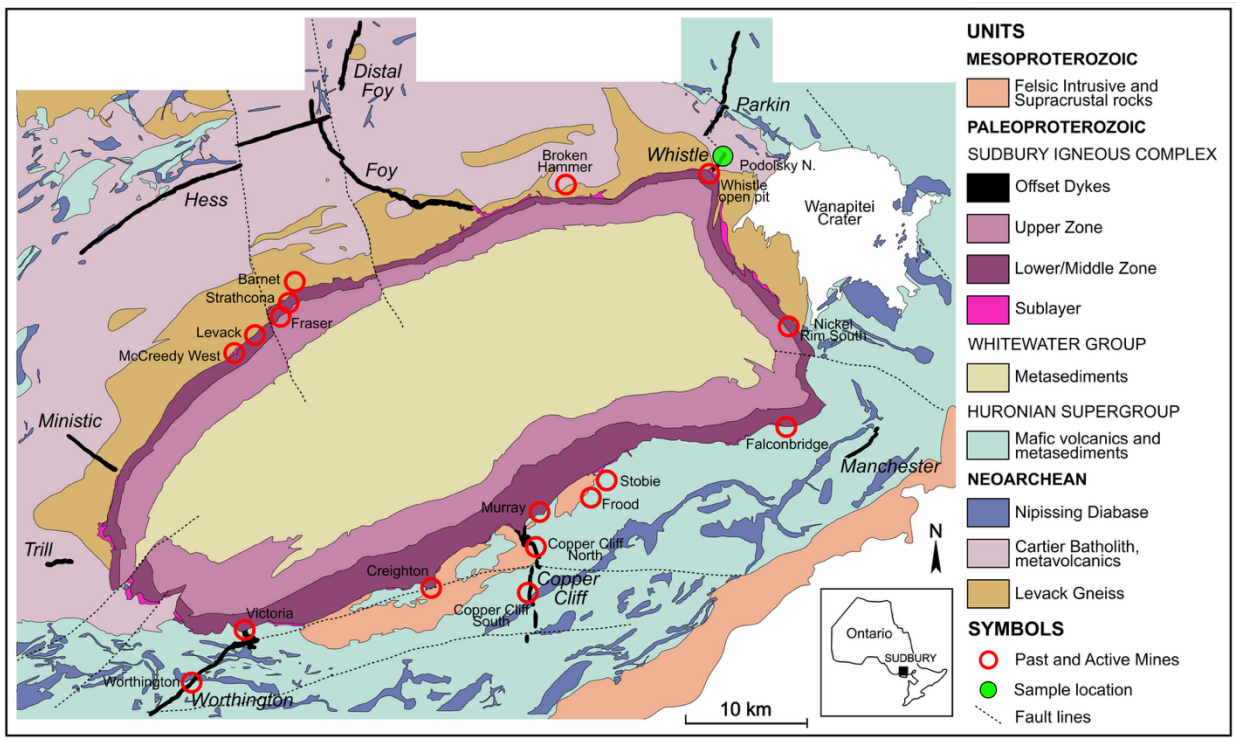

Figure 3.1.1 Simplified geologic map of the Sudbury Structure, Canada, showing the major lithological units and relevant faults in the Sudbury region, past and producing mines, and the sample locality of this study. Based on Ames and Farrow (2007).

The late Archean Cartier Batholith, a monzogranitic and granodioritic intrusion formed by partial melting of the LGC (Meldrum et al., 1997), has a U/Pb zircon crystallization age of 2642 ± 1 Ma (Krogh et al., 1984). These rocks, exposed at the southern margin of the Superior Province, may reflect late-stage Archean collision with the Southern Province (Card, 1994; Wodicka, 1997). The Southern Province rocks overlie the Superior rocks unconformably, forming the country rocks for the South Range of the SS and dominated by metasedimentary and metavolcanic rocks of the Huronian Supergroup. This includes intrusions such as the Murry pluton (2477 Ma; Krogh et al.,

1996), the Creighton pluton (2420 Ma; Scott and Spray, 1999) and the 2219 Ma Nipissing dykes (Corfu and Andrews, 1986).

3.2 The Sudbury Impact Event and Sudbury Igneous Complex

The Sudbury Structure is now widely accepted to be the erosional remnants of a much larger transient impact crater (Grieve et al., 1991; Deutsch et al., 1995). During the 1850 Ma Sudbury Event, a bolide approximately 12 km in diameter, traveling at a velocity of about 25 km/s, impacted the Sudbury area and created a transient crater about 100 km in diameter and roughly 30 km deep (Petrus et al., 2015). The collapse of the crater rims along normal faults expanded the crater to a larger diameter of approximately 200-260 km (Krogh et al., 1984; Grieve, 1994).

The impact generated a 3-6 km thick sub-horizontal melt sheet by *in situ* flash melting of highly fragmented basement rocks (Grieve et al., 1991; Deutsch et al., 1995; Zieg and Marsh, 2005). The most convincing evidence of this impact includes radially distributed shatter cones around the SIC, an abundance of pseudotachylite within a unit known as the Sudbury Breccia, and high-pressure shock metamorphic polymorphs of quartz (e.g., coesite and stishovite), all of which decrease in abundance moving further from the SIC (Thompson et al., 1998; Rousell et al., 2003; Reimold and Gibson, 2005; Ames and Farrow, 2007; Lafrance et al., 2008). The cooling of this sheet resulted in the formation of the differentiated body referred to as the Main Mass of the Sudbury Igneous Complex (SIC).

The nearly 2.5 km thick SIC is divided into the Main Mass and the Sublayer. The igneous units of the SIC differ slightly between the North and South Ranges but generally consist of the following: (1) a discontinuous Sublayer of ultramafic-felsic anteliths and xenoliths in a noritic matrix that overlie fragmented anatectic country rocks (footwall breccia), (2) a discontinuous layer of mafic norites in the North Range and quartz norites in the South Range, (3) a transitional rock unit of quartz gabbro, and (4) granophyre, an amphibole- and biotite-bearing monzogranite with well-developed granophyric texture. These units have been variably interpreted as representing the crystallization of an originally heterogeneous impact melt sheet (Grieve et al., 1991; see review by Lightfoot et al., 1997b) through closed-system fractional crystallization (e.g., Ariskin, 1999), density-driven segregation of mafic and felsic clasts (Golightly, 1994), or density-driven segregation of an emulsion of mafic and felsic melts (Zieg and Marsh, 2005).

The SIC includes ten known impact event-related offset dykes (Fig. 3.1.1) emplaced into the basement along fractures formed during the modification of the crater walls (Naldrett and Hewins, 1984). Most offset dykes connect with the Sublayer through funnel-like embayments and can extend outward from these embayments for several kilometers. Many offset dykes also contain economic Ni-Cu-PGE deposits (Wood and Spray, 1998).

Two styles of offset dyke have been identified in Sudbury, radial and concentric, each characterised by subtle differences in chemical composition. Radial offsets can extend up to 20 km from the SIC and have compositions between quartz monzodiorite-granodiorite-tonalite, locally known as quartz diorite (QD; Wood and Spray, 1998; Lightfoot et al., 2001). These radial dykes often contain inclusion-rich quartz diorite (IQD) and are locally mineralized in their cores. Concentric offset dykes can extend outward for 15-20 km from the lower contact of the SIC and are dominated by Sudbury Breccia with quartz diorite that tends to be less chemically evolved than the QD of the radial dykes (Wood and Spray, 1998; Lightfoot, 2016).

The compositional variability of the radial dykes may be attributed to contamination from assimilated country rock fragments (Lightfoot et al., 1997b), or they may represent a more evolved melt composition that pooled at the base of the SIC following Main Mass fractionation (Wood and Spray, 1998). Some QD is similar to the felsic SIC norite of the North Range; both are thought to represent the initial compositions of the Main Mass (e.g., Thomson, 1935; Lightfoot et al., 1997a; Wood and Spray, 1998).

The Main Mass is overlain by the Whitewater Group, including the Onaping Formation, Onwatin Formation, and Chelmsford Formation, which consist of fall-back and suevitic breccias, pelagic argillite, and siltstone and turbiditic sandstone, respectively (e.g., Rousell, 1984; Ames et al., 2002).

3.3 Metamorphism and Deformation

Multiple metamorphic and deformation events have altered the Sudbury Structure both before and after the impact event. In the North Range, country rocks initially metamorphosed to lower granulite facies, were retrogressively metamorphosed to the upper amphibolite facies before and/or during impact (Card, 1994; Wodicka, 1997). The cooling of the SIC produced contact aureoles radially around the SIC. The aureole on the South Range is much thicker than that on the North Range (Dressler, 1984; Boast and Spray, 2006; Jorgensen et al., 2018). A summary of the contact thicknesses and metamorphic grades is provided in Table 3.3.

Post-impact deformation during the Penokean Orogeny event (1.9-1.7 Ga) resulted in a regional greenschist facies overprint on the entire Sudbury Structure (Card et al., 1984; Mukwakwami et al., 2012). Although the initial shape of the impact crater was roughly circular, the most notable post-impact deformation event was the Penokean Orogeny (Sims et al., 1989). This event is believed to have caused the northwest-directed shortening of the SS, resulting in its present-day elliptical shape (Shanks and Schwerdtner 1991). The Penokean Orogeny likely also caused the “decoupling” of the North Range from the South, preventing any further deformation in the North (Boerner and Milkereit 1999).

Table 3.3 Widths and estimated temperatures for contact metamorphic aureoles on the North and South Ranges of the SIC.

	Anatectic Zone	Pyroxene Hornfels	Pyroxene Granofels	Hornblende Hornfels	Plagioclase Recrystallization
North Range[1]		0-100 m ≥ 600ºC		100-300 m ~540ºC	300-1200 m ~400ºC
North Range[2]	≤ 25 m	< 180 m		≤ 900 m	
South Range[3]	~1000ºC > 20% melt	0-500 m ≥ 885ºC 10-20% melt	500-750 m ≥ 740ºC	750-1000 m ≥ 680ºC	

References: [1]Dressler, 1984; [2]Boast and Spray, 2006; [3]Jorgensen et al., 2018.

3.4 Mineralization in the Sudbury Structure

Mineralization in the SIC occurs in two primary styles: Ni-Cu-rich contact-style ores and Cu-(Ni-)PGE-rich footwall-style ores. The contact ores, localized in troughs and depressions along the basal contact, range from disseminated in the sublayer norites to semi-massive pyrrhotite-pentlandite-chalcopyrite bodies.

Footwall ores, consisting of veinlets to massive chalcopyrite ± millerite ± bornite and precious metals (PGE, Au, Ag, Te, Bi, Se), are emplaced into the fractured Sudbury Breccia and footwall breccia below the sublayer (Pattison, 1979; Ripley et al., 2015). The most productive mines in the Sudbury region rarely contain just one style of mineralization. Notable past and present producers such as Creighton, Levack-Coleman, and Victor-Nickel Rim South, have yielded both contact- and footwall-style ores. A common feature among these deposits is their spatial association with embayment structures located along the margins of the SIC (Lightfoot, 2016). The offset dykes, which extend from these embayments, typically contain the Cu-(Ni-)PGE-rich footwall ore representative of the residual sulfide liquid fractionated from the evolving sulfides at the base of the melt sheet (Dare et al., 2014). Offset dykes show transitional mineralization, shifting from contact-style in the embayment to footwall-style distally (Pilles et al., 2018).

Since the late 19th century, Sudbury evolved into one of the world's most prolific mining districts, producing substantial quantities of nickel, copper, cobalt, platinum group elements (PGE), gold and silver. Early mining operations at deposits such as Creighton and Frood-Stobie exploited exceptionally high-grade ores, with some zones averaging 5-8% Ni and 4-6% Cu (Lightfoot, 2016). As surface resources were depleted, advancements in exploration and mining technologies enabled the development of deeper, lower-grade, and more geologically complex deposits, characteristic of modern operations.

4. The Whistle Embayment, Offset, and Podolsky North Zone

4.1 Whistle Embayment and Whistle-Parkin Offset

The Whistle-Parkin radial offset dyke is located approximately 32 km northeast of the city of Sudbury, within Norman Township. This offset dyke connects to the Main Mass of the SIC through the funnel-shaped Whistle embayment (Fig. 4.1.1). At its intersection with the SIC, the embayment structure is approximately 250 m wide and 1 km thick, and is predominantly composed of Sublayer norite (Pattison, 1979; Lightfoot et al., 1997b; Murphy and Spray, 2002). Within the embayment and associated offset dyke, clasts of various sizes, shapes, and compositions are present, including material derived from the Levack Gneiss Complex, Grey Gabbro, Sudbury Breccia, as well as Nipissing and Matachewan diabase dykes (Lightfoot et al., 1997b; Murphy and Spray, 2002). Gneiss and diabase are the most abundant clast types. Collectively, this material is referred to as footwall breccia and is thought to have significantly contributed to the chemical composition of the magma which formed the Sublayer matrix (Lightfoot et al., 1997b; Lightfoot and Zotov, 2005).

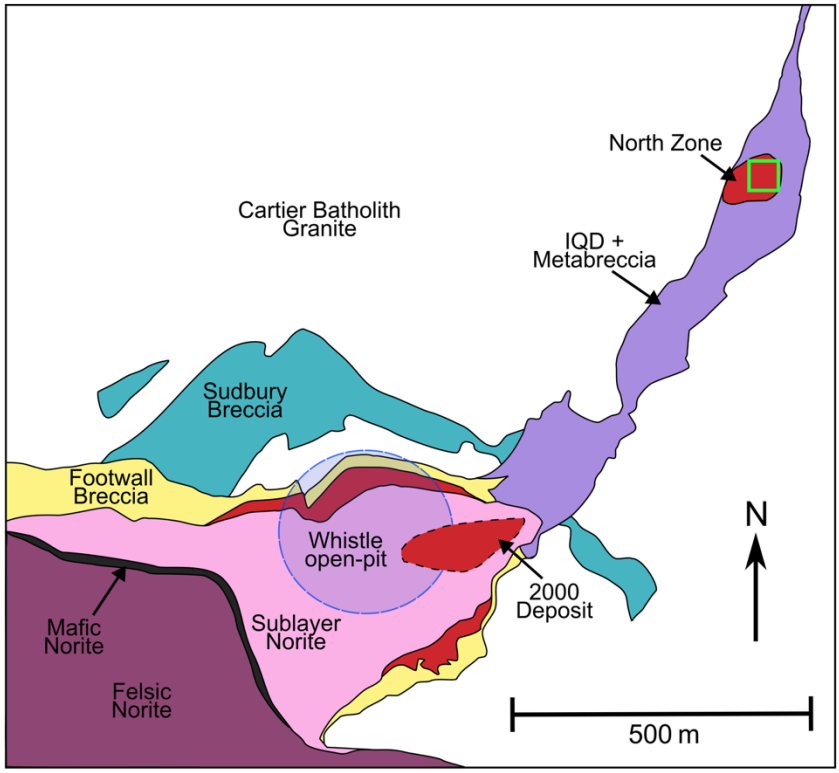

Figure 4.1.1 Simplified geological map of the Whistle Embayment and Whistle Offset within the northeastern Sudbury Igneous Complex (SIC). The embayment structure (pink and yellow units) contains Sublayer norite surrounded by footwall breccia, which transitions northeastward into the Whistle Offset dyke (light purple) composed of inclusion-rich quartz diorite (IQD) and metabreccia, intruding the Cartier Batholith granites and later the Levack Gneiss Complex. The Main Mass of the SIC is represented by felsic and mafic norite (dark purple and black). The

extent of the Whistle open pit mine is outlined by the shaded blue circle, an approximate surface projection for mineralization in the 2000 Deposit (dashed outline), and the North Zone occurring further along the offset dyke, near surface (solid lines). Green box indicates the location of the Podolsky North Zone outcrop in Figure 4.3.1. Modified from Lightfoot et al. (1997b) and Carter et al. (2009).

Extending 10 km to the northeast from the embayment, the Whistle-Parkin offset dyke cuts through the Archean Cartier Batholith and Levack Gneiss Complex that form the basement rocks in the North Range of the SS (Pattison, 1979). Less than 50 m from the base of the embayment and roughly parallel to the SIC, the offset intersects a discontinuous zone of impact-related Sudbury Breccia (Lightfoot et al., 1997b). The offset dyke consists of three quartz dioritic phases: mineralized inclusion-rich quartz diorite (IQD), quartz diorite (QD), and leucocratic quartz diorite (LQD). The LQD is unique to the North Range, where assimilation of the Archean basement rocks is believed to have contributed to its distinctive leucocratic character (Carter, 2005). The footwall breccia and IQD comprise the majority of the Whistle structure with small pods of QD dispersed throughout.

The Whistle embayment to offset dyke transition has been described by Carter et al. (2009) based on proximity to the Cu-Ni contact ore of the Whistle open pit within the embayment, with the following subdivisions recognized: a proximal zone (0-250 m), intermediate zone (250-500 m) and distal zone (>500 m). The proximal zone is characterized by pods of LQD occurring along the exterior of the offset; the intermediate zone contains smaller LQD pods, whereas the distal zone lacks LQD entirely.

The Whistle-Parkin offset has historically been divided into two segments, distinguished by fault zones that are oriented perpendicular to the strike of the offset dyke. The first segment, known as the Whistle offset, extends 2 km from the base of the SIC, through the embayment, and terminates at the Post Creek Fault Zone. The second segment, the Parkin offset, is a ~8 km portion of the same offset that has been displaced 2 km northwest of the Whistle offset along the Post Creek Fault. However, recent work by Pilles et al. (2022) found no evidence of a connecting fault between the two segments and concluded they represent separate, unassociated offset dykes.

North and South Range offset dykes are commonly classified according to either ‘multiple injection’ or ‘single injection’ emplacement models. In the North Range, most radial offset formation models generally support a single, possibly flow-differentiated injection of melt, where fine-grained marginal or contact QD formed along the footwall breccia, and internal flow and convection concentrated clasts and sulfide melt toward the dyke center, forming IQD (Lightfoot et al., 1997a; Murphy and Spray, 2002; Pilles et al., 2018). In contrast, South Range dykes are often interpreted as the product of multiple injections, where an initial pulse of QD, originating from the early fractionating Main Mass melt sheet, was followed by a second pulse of IQD melt injected into the core (Lightfoot and Farrow, 2002; Scott and Benn, 2002; Therriault et al., 2002). In both

models, the clastic footwall breccia was partially melted and recrystallized by the latent heat of the melt during its transport, producing the metabreccia (Farrow et al., 2005; Lafrance et al., 2014; Pilles et al., 2022).

The Whistle offset dyke, however, does not wholly conform to either model: QD occurs only as small, discontinuous pods within a dominantly IQD dyke. Geochemical analysis by Carter (2005) confirms that these QD pods share chemical characteristics with the surrounding IQD matrix. In support of the interpretation by Pilles et al. (2022), the Parkin offset displays QD and IQD distributions consistent with other North Range dykes, making the Whistle offset unique within the SIC.

4.2 Podolsky Mine Property Mineralization

The Whistle embayment hosts the contact-style mineralization that is believed to have formed as a result of density and gravitational settling of the rapidly convecting main SIC melt sheet, with sulfide and footwall breccia accumulation at the basal contact (Murphy and Spray, 2002; Lightfoot and Zotov, 2005). The historic Whistle open-pit located within the embayment at the Podolsky Mine property was mined by INCO from 1988 to 1993, producing 5.7 Mt of ore with grades of 0.95% Ni, 0.33% Cu, and <500 ppb platinum-group elements (PGE) from the pyrrhotite-pentlandite-rich ore (Lightfoot et al., 1997b).

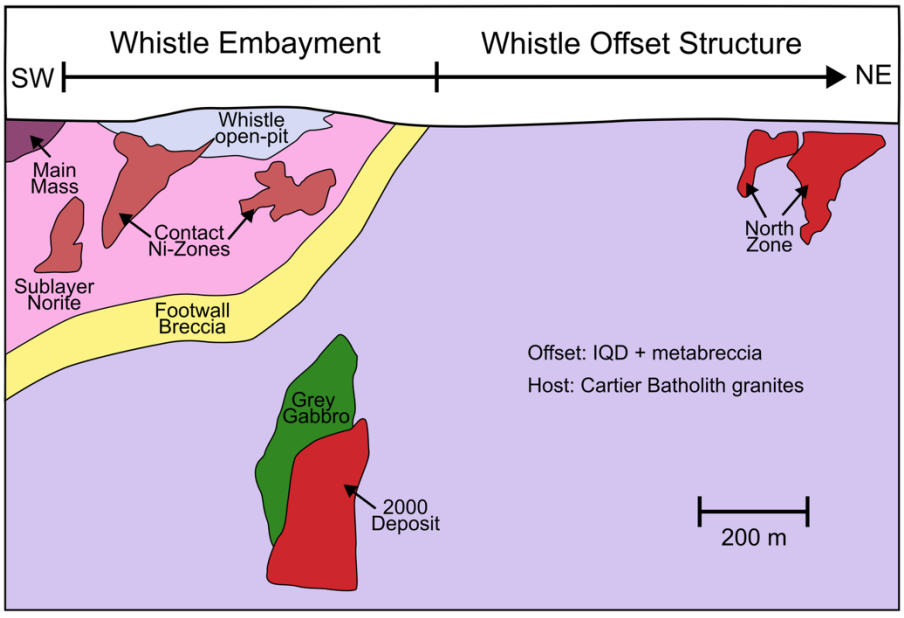

Figure 4.2.1 Simplified schematic cross-section of the Podolsky Mine property illustrating the distribution of mineralization at depth across the Whistle embayment (SW) into the Whistle offset dyke (NE). Contact Ni-Cu-(PGE) zones are localized near the base of the Whistle open-pit within the Sublayer, with additional mineralization hosted in the North Zone and 2000 Deposit. The 2000 Deposit is spatially associated with the Grey Gabbro unit hosting disseminated

sulfides. The offset dyke comprises inclusion-rich quartz diorite (IQD) and metabreccia, hosted within the Cartier Batholith granites. The approximate surface extent of the Whistle open pit mine is also shown. Modified from Carter et al. (2009) and Magna Mining Inc (2025).

The Cu-Ni-PGE Podolsky Mine properties are located in the proximal and distal zones of the Whistle offset (Fig. 4.2.1). The deposits contain a hybrid of contact and footwall ore within the past-producing "2000 Deposit" and advanced Podolsky North Zone. The Cu-(Ni-)-PGE-rich 2000 Deposit occurs ~200 m from the base of the embayment and ~650 m below the surface. This deposit includes massive sulfide mineralization within the IQD, and disseminated sulfides in the adjacent Grey Gabbro, a unit interpreted as a large fragment of the Archean gabbroic basement (MacInnis, 2019). Collectively, the 2000 Deposit was mined by FNX from 2007 to 2013, yielding 1.75 Mt of ore, grading 3.9% Cu, 0.3% Ni, and 3.9 g/t PGMs (Magna Mining Inc, 2025). The North Zone has been historically explored for its economic potential but remains undeveloped at the time of the present study.

4.3 Podolsky North Sampling Locations

Located approximately 800 metres northeast of the 2000 Deposit, the Podolsky North Zone (Fig. 4.3.1), informally referred to as "The Yellow Brick Road" by FNX Mining, hosts exceedingly Cu-rich footwall mineralization exposed in outcrops across the property. The primary objective of fieldwork in this area associated with the current study was to document the lithological and structural relationships of the sulfide veins observed at surface, and to collect representative samples of Cu-PGE ore along with their host rock material.

At the surface, the chalcopyrite-rich veins are intensely tarnished, and irregular in both shape and size, ranging from millimetre-scale stringers to massive veins approximately 3 metres wide. These veins are hosted in both inclusion-rich quartz diorite (IQD) and footwall breccia. Those within the IQD generally trend northwest-southeast, while veins in the footwall breccia exhibit a northeast-southwest orientation. The sulfide vein morphology exhibits evidence of ductile deformation and appears to exploit structural pathways at lithological boundaries between the footwall breccia and IQD, as well as along the margins of metabreccia clasts (Farrow et al., 2005; Carter et al., 2009), forming a complex, interconnected network at the surface.

Massive sulfide veins bearing platinum-group elements (PGE) are commonly associated with halogen-rich alteration halos (Molnar et al., 2001; Hanley and Mungall, 2003; Hanley et al., 2004). In the North Zone, such alteration is typically concentrated around chalcopyrite-rich veins and manifests as epidote- and chlorite-rich selvages ranging from a few millimetres to metres in width. Alteration zones not directly associated with sulfides are also common and include assemblages of epidote, chlorite, amphibole, carbonate, and quartz (Farrow et al., 2005; Carter et al., 2009). In some areas, thin magnetite rinds occur adjacent to the massive sulfide veins and are interpreted as products of late-stage alteration of chalcopyrite (Carter, 2005).

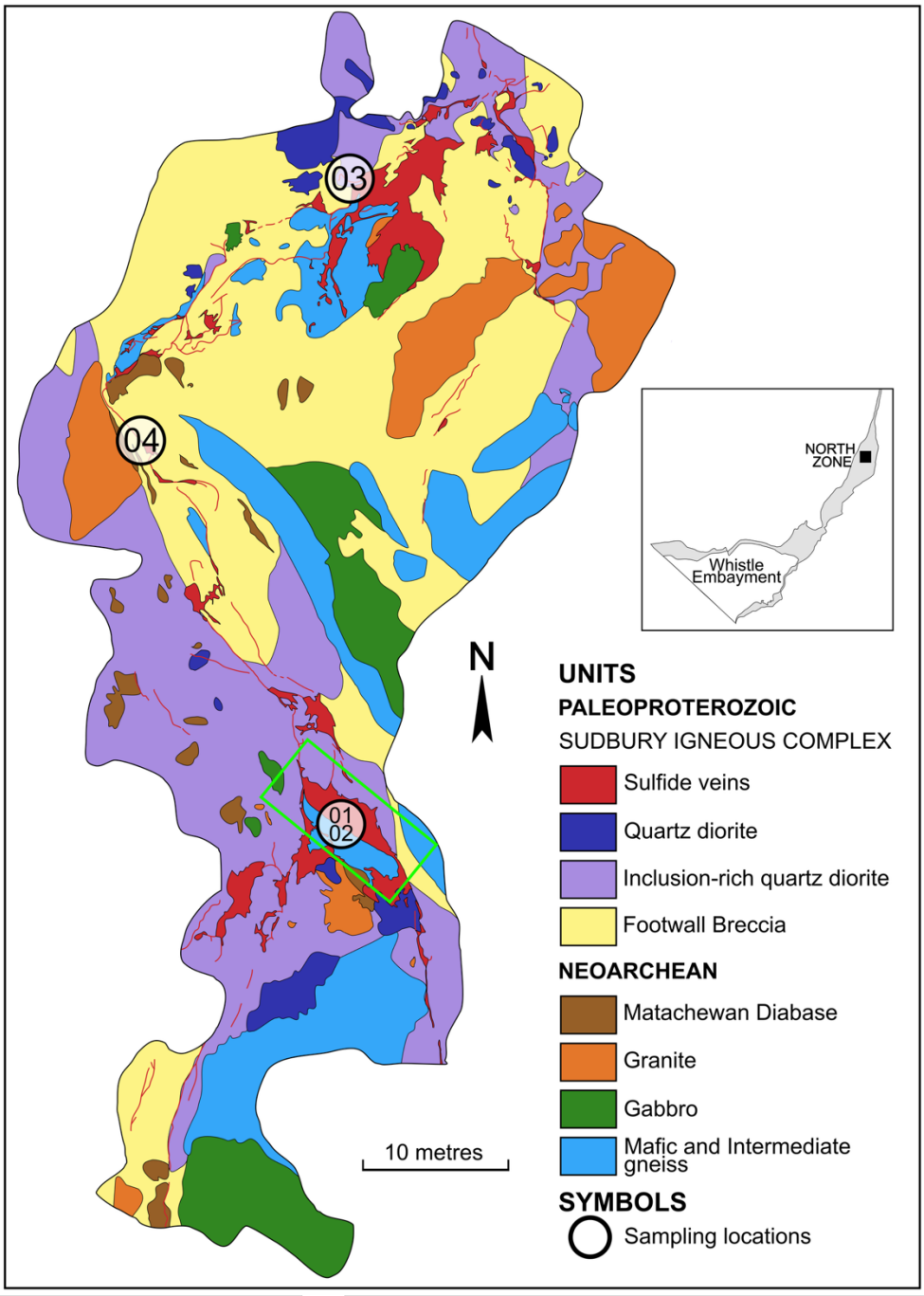

Figure 4.3.1 Geological map of the surface exposure from Podolsky North Zone in the northeastern Whistle offset dyke (modified from Carter, 2005), ~800 m from the 2000 Deposit. Map illustrates the distribution of lithologies, sulfide veins, and sampling locations. Metabreccia in the inclusion-rich quartz diorite include the clasts of gneisses, gabbro, and Matachewan diabase. Country rock in this location is the granite of the Cartier Batholith. Black circles indicate sample sites P23-X, where X represents the number within the circle. The green box indicates the location of images in Fig. 4.3.2. Inset map shows the position of the Podolsky North Zone relative to the Whistle Embayment and Whistle Offset detailed in Fig. 4.1.1.

To better understand the relationship between volatile-rich minerals, PGE-bearing sulfide veins, associated alteration haloes, and the host rock, samples were collected from multiple locations within the North Zone, as shown in Fig. 4.3.1. Channels were cut across vein margins, through their respective chloritic alteration haloes, and into the adjacent rock. Typical channel dimensions averaged ~40 cm in length and ~7 cm in depth. The aim was to obtain continuous samples incorporating each lithological and alteration domain to aid in tracing mineralogical and textural changes across a vein-halo-host transition. One channel sample, from location P23-02 was selected for detailed thin sectioning and analytical work, its exact location and channel orientation shown in Fig. 4.3.2.

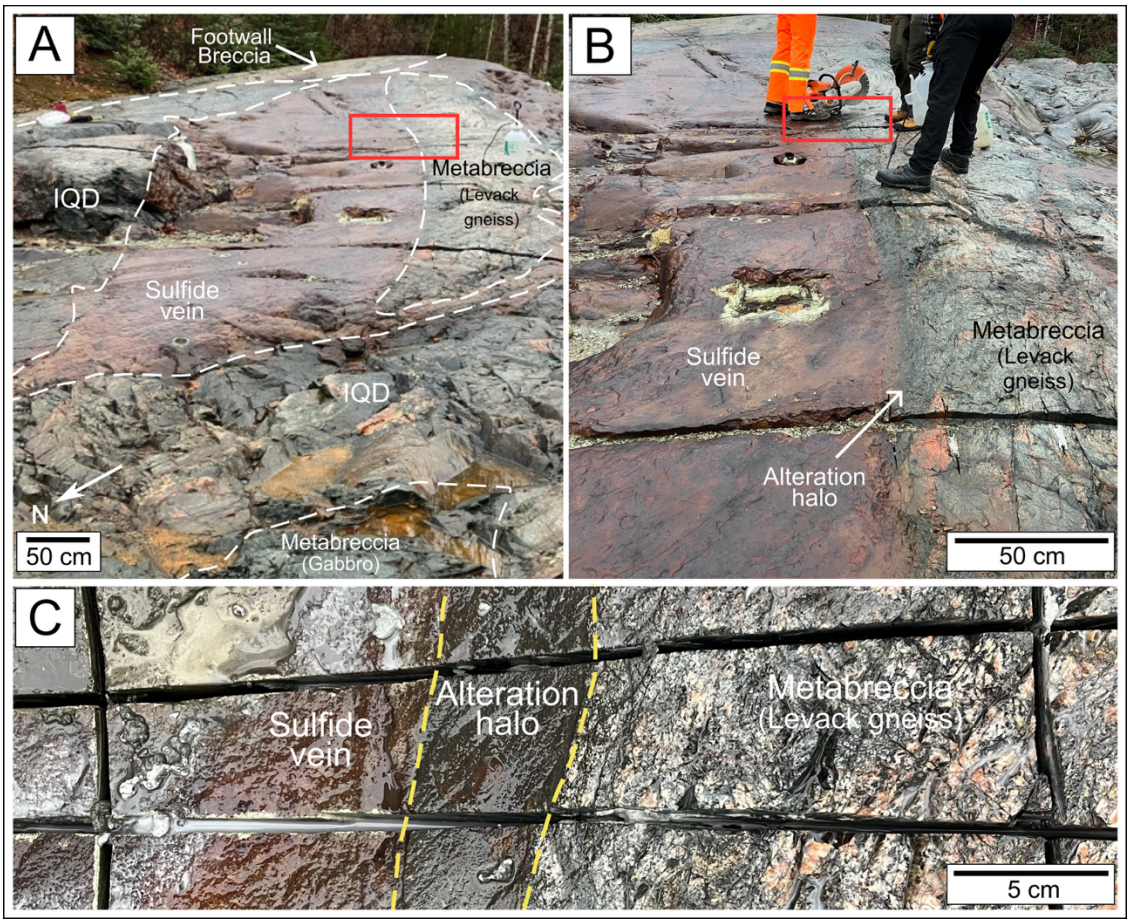

Figure 4.3.2 Outcrop images of the sampling location for P23-02 (green box in Fig. 4.3.1) at the surface of the Podolsky North Zone. The north directional arrow in A is the same for all images. The red box in A and B show the location of image C. A) Massive chalcopyrite-rich sulfide vein in contact with a clast of Levack gneiss metabreccia contained within inclusion-rich quartz diorite (IQD). Image also shows the close proximity of Levack gneiss and gabbroic metabreccia clasts. B) Closer image of A showing the chloritic alteration halo formed between the sulfide vein and Levack gneiss. Some areas along the contact display a less defined chloritic zone. C) Image of the surface of channel sample P23-02 showing the highly tarnished sulfide vein, defined chloritic alteration halo enclosed by the yellow dashed lines, and Levack gneiss metabreccia displaying a fine-scale granophyric texture on its surface.

5. Analytical Methods

Sixteen representative polished thin sections were produced from the P23-02 channel for petrographic and chemical analysis. Microscopy was carried out in transmitted and reflected light in order to fully characterize the mineralogy and microstructure of the massive sulfide vein and its gneissic host rock (metabreccia). For thin section locations (TS #), see Chapter 6.1.

5.1 Scanning Electron Microscopy (SEM) and Field-Emission SEM

Mineralogy was examined using semi-qualitative scanning electron microscopy (SEM) on six polished thin sections and field-emission SEM (FE-SEM) on the fractured surfaces from three associated chips of those six thin sections. Polished thin sections were selected from key lithological units and mineralized zones in P23-02 to capture the range of textures, alteration styles and sulfide assemblages observed in reflected light. Three sections are from the massive sulfide vein (TS 1, 2, 5), two from the chloritic Contact Zone (TS 7, 8) and one from the gneissic host rock (TS 14). Fractured chips were taken from the edges of the corresponding samples – two from the vein (TS 1, 6) and one from the Contact Zone (TS 7). Each SEM is fitted with backscattered electron detectors (BSE) for imaging, which was also carried out.

The polished sections were analyzed at the University of Ottawa on a JEOL JSM-6610LV SEM equipped with an Oxford INCA X-max 20 mm^2 silicon drift detector (SDD) capable of qualitative microanalysis using energy dispersive spectroscopy (EDS) at a working distance of ~10 mm, accelerating voltage of 20 kV and 5 nm spot size. Raw data were processed using the EDAX APEX software package.

Slivers of the sample chips were cut and mounted using carbon tape before cracking open to reveal a fresh surface. The fractured surfaces were analyzed at Saint Mary's University (Halifax, Nova Scotia) with a TESCAN MIRA 3 LMU Variable Pressure Schottky field emission SEM, equipped with an Oxford INCA 80 mm^2 SDD for EDS at a working distance of ~17 mm, accelerating voltage of 20 kV and 5 nm spot size. Raw data and element maps were processed using the AZtec software package. Due to the uneven surface of samples analyzed, compositions have a higher error for Cu+Fe+S impurities. Data were corrected to remove impurities using the empirical formula of chalcopyrite [$CuFeS_2$], in Microsoft Excel.

5.2 Electron Probe Micro-Analysis (EPMA)

Four polished sections were selected to quantify the composition of epidote and chlorite across the channel. One section was taken from the massive sulfide vein (TS 6), where a band of epidote-chlorite-quartz is present, two from the chloritic Contact Zone (TS 7, 8), and one from the gneissic host rock (TS 10). These sections were used for both epidote and chlorite quantitative

analyses, with spot analysis locations tracked spatially along three stacked traverses from the vein into the host rock. Quantitative compositions were determined using the JEOL JXA-8230 SuperProbe at the University of Ottawa. A total of 10-16 grains of epidote and 15-20 grains of chlorite per traverse were targeted.

The analysis was conducted with an accelerating voltage of 20 kV and probe current of 20 ηA, with a beam size of 5 μm. The following standards were used for both minerals: albite (Na$K\alpha$); diopside (Ca$K\alpha$, Mg$K\alpha$); sanidine (Si$K\alpha$, Al$K\alpha$, and K$K\alpha$); hematite (Fe$K\alpha$); rutile (Ti$K\alpha$); tephroite (Mn$K\alpha$); pentlandite (Ni$K\alpha$); tugtupite (Cl$K\alpha$); chromite (Cr$K\alpha$). Peak counting times for each analyzed element were 20-30 seconds.

Raw data were converted to elemental weight percent by the Cameca PAP matrix correction program. Analyses are accurate to 1-2% relative for major elements, 3-5% relative for minor elements (<1 wt.%). Oxygen was calculated by stoichiometry with a formula based on 13 atoms of O for epidote and 18 atoms of O for chlorite. Data were plotted using the Matplotlib package in Python.

5.3 Micro-X-Ray Florescence Spectrometry (μXRF)

False color elemental distribution maps were created from the surface of a hand sample containing the sulfide vein-gneiss contact on the opposite side from which thin sections were cut (TS 7, 8). Maps were produced using a Bruker M4 Tornado^{PLUS} Micro-X-ray fluorescence (μXRF) spectrometer at Saint Mary's University. Analysis was conducted under vacuum using an Rh source at an accelerating voltage of 50 kV, a beam current of 600 μA and a spot size of 20 μm, with a counting time of 10 ms/pixel. Raw data were processed with the M4 software to produce relative intensity maps and modal abundances. Interference from peak overlaps was deconvoluted based on the Bayesian approach. All colour scales shown in the maps are linear.

5.4 Sulfur Isotopes

Nine thin section chips from the massive sulfide vein (TS 1-6), chloritic Contact Zone (TS 7, 8) and the gneiss (TS 9) were polished and photographed to identify relatively clean areas of chalcopyrite, free of other sulfides. Samples were cleaned with ethanol and drilled using an automated microdrill to a depth of 500 μm. Approximately 0.14 mg of powder was weighed into tin capsules in order to collect the amount of sulfur required from the chalcopyrite.

About 1 mg of sucrose was added to the tin capsule to help combustion and provide a constant oxygen source, minimizing $O1^{8/16}$ effects on ^{34}S. Samples were loaded into an Elemental Analyser Isotope Cube in S mode (Elementar, Germany) to be flash combusted at 1800˚C. The gases released were carried by helium through the EA where water was chemically removed and

SO_2 separated from CO_2 and N_2 by a trap and purge column. The SO_2 gas was carried into the Delta Plus XP isotope ratio mass spectrometer (ThermoFinnigan, Germany) via a conflo IV interface for ^{34}S determination. Because samples were consumed during analysis, analytical precision was assessed using repeated measurements of international and in-house standards interspersed throughout the session. Precision is reported as ±0.3‰ (1σ), based on the standard deviation of the analyses of these reference materials. Data were plotted using the Matplotlib package in Python.

6. Sample Observations and Analytical Results

6.1 Petrography

The following sections provide a detailed petrographic description of the domains defined in Fig. 6.1. For this study, the massive sulfide vein is subdivided into an Inner Vein and an Outer Vein based on mineralogical variations and textural changes. The Inner Vein (TS 1-3) comprises the core of the sulfide body, dominated by chalcopyrite with minor abundances of Ni-bearing minerals and precious metal minerals (PMM). The Outer Vein (TS 4-7) is distinguished by a reduction in the abundance of these phases, an increase in deformation textures, and the presence of localized silicate mineral-rich bands. The boundary between the Outer Vein margin and host rock (in TS 7) is a sharp contact between the sulfide vein and the surrounding silicate rocks; however, a "Contact Zone" extends approximately 6 cm outward from this boundary, characterized by foliated chlorite-rich rock with accessory sulfides (TS 7, 8). Beyond this, the host rock consists of partially melted, metamorphosed metabreccia of the Levack Gneiss Complex (TS 9-16), exhibiting mineralogical and microstructural characteristics interpreted to result from contact metamorphism and hydrothermal alteration. This metabreccia clast has been classified as an intermediate gneiss of the Levack Gneiss Complex (Carter et al., 2009). A complete list of the minerals observed, their abbreviations and ideal chemical formulae are given in Table 6.1. A schematic cross section of the channel displaying the notable trends described throughout this chapter is provided in Chapter 7.1.

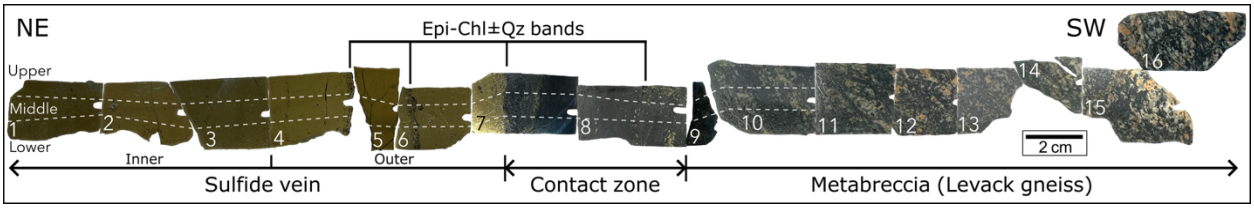

Figure 6.1 Photo of polished sample chips over the ~43 cm channel sample P23-02 defined by lithology: Inner Vein, Outer Vein, Contact Zone, and host gneiss (Metabreccia). Numbers coincide with thin sections (TS) referred to in text and figure captions. Dashed horizontal lines represent the bounds of the Upper, Middle, and Lower transects used for EPMA and sulfur isotope analysis.

Table 6.1 List of minerals observed in thin section and identified with SEM (Chapter 6.2). Formulas given are the ideal stoichiometric formulas. Calculated average formulas for each mineral analyzed by SEM are provided in Appendix Table A6.

Mineral	Abbr.	Formula	Mineral	Abbr.	Formula
Major and minor minerals					
Chalcopyrite	Ccp	$CuFeS_2$	Quartz	Qz	SiO_2
Pyrrhotite	Po	Fe_7S_8	Chlorite	Chl	$(Fe,Mg,Al)_6(Si,Al)_4O_{10}(OH,O)_8$
Magnetite	Mag	Fe_3O_4	Epidote	Epi	$Ca_2(Al_2Fe)Si_2O_7(SiO_4)O(OH)$
Violarite	Vio	$FeNi_2S_4$			
Marcasite	Mrc	FeS_2			
Mineral	**Abbr.**	**Formula**	**Mineral**	**Abbr.**	**Formula**
Trace and rare minerals					
Fe-, Ni-bearing			*Cl-bearing*		
Millerite	Mlr	NiS	Halite	Hl	NaCl
(Ni-)Pyrite	Py	$(Fe,Ni)S_2$	Chlorargyrite	Cag	AgCl
Siegenite	Seg	$CoNi_2S_4$	Cotunnite	Cot	$PbCl_2$
Hematite	Hem	Fe_2O_3	Hibbingite	Hib	$Fe_2(OH)_3Cl$
Goethite	Gth	FeO(OH)	Ferropyrosmalite	Pys-Fe	$(Fe,Mn)_8Si_6O_{15}(OH,Cl)_{10}$
Cu-bearing			*Ti-bearing*		
Covellite	Cv	CuS	Rutile	Rt	TiO_2
Cubanite	Cbn	$CuFe_2S_3$	Ilmenite	Ilm	$FeTiO_3$
Co-, Ni-arsenides			Titanite	Ttn	$CaTiSiO_5$
Cobaltite	Cbt	CoAsS	*Phosphates*		
Gersdorffite	Gdf	NiAsS	Apatite	Ap	$Ca_5(PO_4)_3F$
Sn-bearing			Monazite-Ce	Mnz	$Ce(PO_4)$
Cassiterite	Cst	SnO_2	*Sulfates*		
Other base metal minerals			Barite	Brt	$Ba(SO_4)$
Sphalerite	Sph	ZnS	Anhydrite	Anh	$Ca(SO_4)$
Galena	Gn	PbS	*Silicates*		
Bi-, Te-bearing			Plagioclase	Plg	$(Na,Ca)AlSi_3O_8$
Tsumoite	Tsm	BiTe	K-feldspar	Ksp	$KAlSi_3O_8$
Hedleyite	Hdl	Bi_7Te_3	Muscovite	mica	$KAl_2(Si_3Al)O_{10}(OH)_2$
Tetradymite	Ttd	Bi_2Te_2S	Zircon	Zrn	$ZrSiO_4$
Kawazulite	Kaw	Bi_2Te_2Se	Kaolinite	mica	$Al_2Si_2O_5(OH)_4$
Sulphotsumoite	Stsm	Bi_3Te_2S			
Tellurite	Tlr	TeO_2			
Native bismuth		Bi			
Precious metal minerals (Ag, Au)					
Hessite	Hes	Ag_2Te			
Matildite	Mtd	$AgBiS_2$			
Bohdanowiczite	Boh	$AgBiSe_2$			
Acanthite	Aca	Ag_2S			
Naumannite	Nau	Ag_2Se			
Native gold		Au			
Native silver		Ag			
Platinum-Group Minerals (Pd, Pt)					
Sperrylite	Spy	$PtAs_2$			
Merenskyite	Mrk	$PdTe_2$			
Kotulskite	Ktu	Pd(Te,Bi)			
Michenerite	Mch	PdBiTe			

6.1.1 Sulfides and Oxides

The Podolsky North sulfide vein is composed predominantly (~95 vol.%) of massive chalcopyrite, with the remaining 5% consisting of a diverse array of base-metal sulfides and PMM. Outside of the vein, chalcopyrite in the Contact Zone appears as disseminated blebs and rare inclusions in the gneiss. Pyrrhotite occurs as strongly anisotropic anhedral blebs up to 100 μm in size and as thin veinlet exsolutions within the chalcopyrite. The larger blebs are commonly surrounded by voids, while the veinlets are evenly distributed throughout the host chalcopyrite. Pyrrhotite exhibits a distinctive reaction texture with magnetite that produces marcasite (Fig. 6.1.1A, B). The marcasite is micaceous in habit. Rounded to anhedral magnetite grains can be enclosed within either marcasite or unaltered pyrrhotite (Fig. 6.1.1B). This texture diminishes toward the outer part of the sulfide vein.

Pyrite is present in minor amounts, occurring as small cubic aggregates (≤75 μm) or as relatively large (≤1 mm) isolated crystals with compositional zoning from core (pale yellow reflectance) to rim (pale pink reflectance; Appendix A1). Overall, the abundance of pyrite decreases while grain size increases from the Inner Vein toward the Outer Vein.

Two Ni-rich minerals, violarite and millerite, are observed. Violarite occurs in two distinct microstructural forms. Only violarite II is associated with PMM. One variety of violarite I appears smooth and unaltered, always in association with other Ni-bearing phases, most commonly millerite. The violarite-millerite assemblage forms narrow (<25 μm wide) vertical to sub-vertical veinlets crosscutting the minerals of the Inner Vein (Appendix A1). The other form of violarite II appears as isolated blebs, typically in contact with quartz ± chlorite (Fig. 6.1.1C). Violarite II is highly fractured along distinct planes and surrounded by black haloes. Discrete aggregates of additional (suspected) Ni-bearing phases occur within chalcopyrite blebs in the outer Contact Zone, closest to the gneiss contact.

Other base-metal sulfides and oxides occur in lesser amounts. Sphalerite and cassiterite occur in trace amounts, adjacent to or surrounding magnetite. Covellite appears as blue tarnished patches also surrounding magnetite and filling small fractures in the Outer Vein. Galena occurs as minute inclusions within granular pyrite and quartz in the Contact Zone. Hematite is closely associated with magnetite or pyrite, while goethite forms colloform-like textures within large fractures in the chalcopyrite.

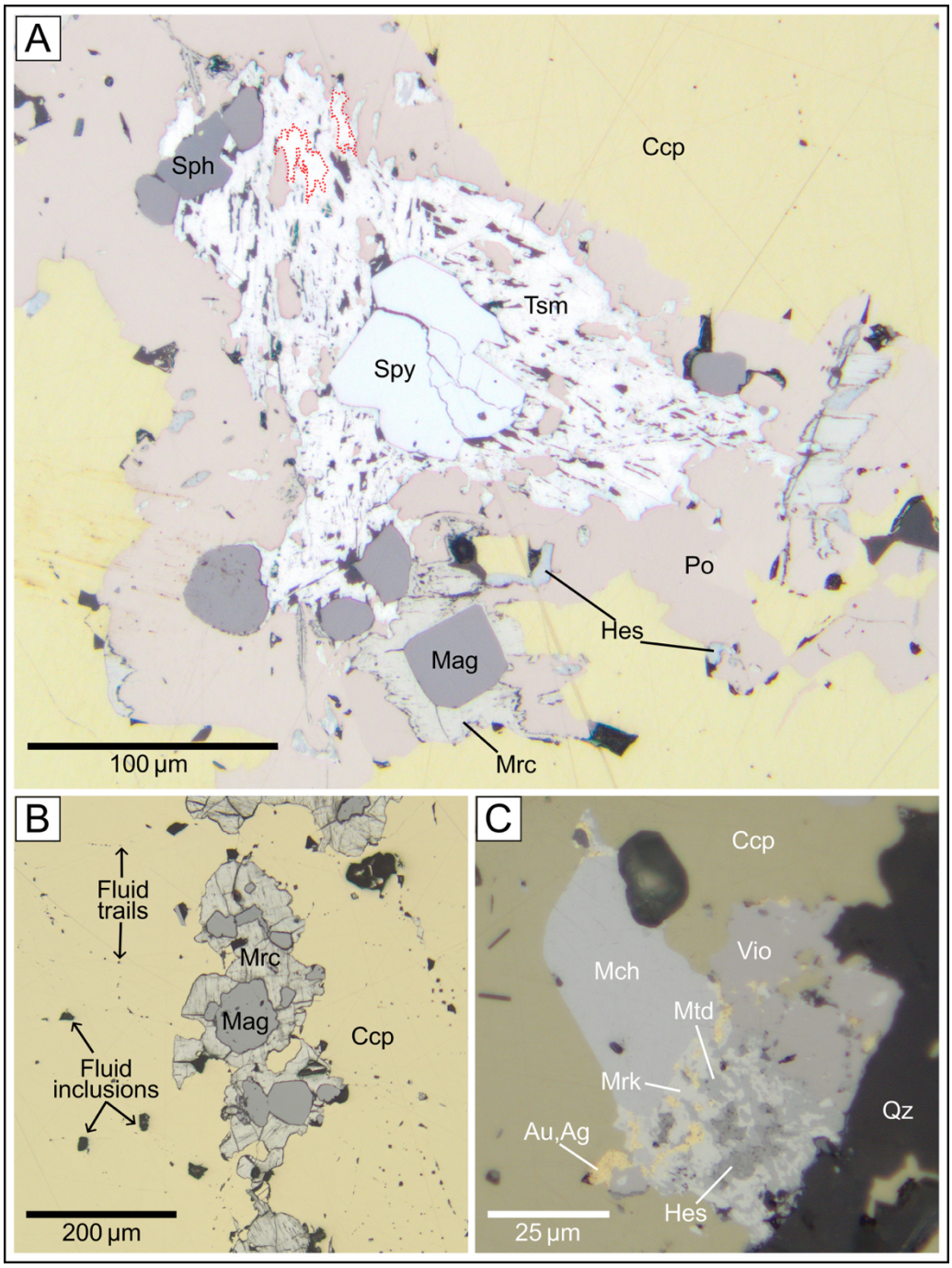

Figure 6.1.1 Reflected light photomicrographs from the massive sulfide vein. A) Large sperrylite grain within a complex aggregate from TS 2. Note that pyrrhotite is being replaced by marcasite at magnetite grain boundaries. Tsumoite and hedleyite, partially outlined in red, surround the sperrylite and form small intergrowths with hessite; B) Large anhedral magnetite enclosed within marcasite from the inner vein (TS 1). The marcasite is associated with fluid inclusion trails that radiate outward and exhibit a preferential orientation trending subvertical with an inclination toward the northeast. Large empty fluid inclusions are also related to these trails; C) Palladium-bearing phases michenerite and merenskyite intergrown with hessite, matildite, and Au, hosted by violarite II in the immediate contact (TS 7). See Table 6.1 for mineral abbreviations.

6.1.2 Precious Metal Minerals (PMM)

Various Ag-Te-Bi-PGE-bearing minerals occur as complex composite grains containing two or more precious metal phases. The most common platinum group minerals (PGM) are michenerite and sperrylite (Fig. 6.1.1), both appearing as individual, well-polished cubic to cubo-octahedral grains. Most grains are <10 μm in size, except for one sperrylite grain measuring ~80 μm (Fig. 6.1.1A). Subtle differences in reflectance make distinguishing these PGM difficult; michenerite has a slightly higher relief and a whiter appearance than sperrylite in reflected light when found within the chalcopyrite. Sperrylite is rarely associated with other precious metal minerals (PMM), whereas michenerite more commonly coexists with hessite and other PGM (Fig. 6.1.1C). Merenskyite and kotulskite, along with hessite and more rarely, michenerite, form composite intergrowths up to 110 μm in size. These intergrowths are found within violarite II near Si-rich inclusions of undeformed quartz and fine-grained micaceous chlorite within the vein (Fig. 6.1.1C). Larger individual and composite grains occur in the Inner Vein, decreasing in size toward the Contact Zone. Restricted to the Upper transect of TS 7 at the immediate contact where the Outer Vein touches the Contact Zone, composite grains also include native gold and matildite, also hosted by violarite II (Fig. 6.1.1C). A few small euhedral sperrylite grains are also found within chlorite in the Contact Zone.

The five major Ag±Bi+Te phases include tsumoite and associated hedleyite, hessite, matildite, and acanthite. Tsumoite is the most abundant, occurring as irregularly shaped elongated inclusions within the massive chalcopyrite. The highly reflective tsumoite is frequently cored by a brighter white phase, hedleyite (Fig. 6.1.1A) and native bismuth. These masses are often adjacent to pyrrhotite and hessite, occasionally including minor Bi-bearing minerals such as tetradymite and two unidentified phases. Notably, tsumoite and hedleyite were never observed in proximity to Pd-Bi-Te minerals, though one instance was observed where they surrounded a large sperrylite grain (Fig. 6.1.1A).

Hessite is often associated with PGM as small, irregular grains or intergrown with them. Matildite blebs display an anomalous pale mint-green bireflectance when not intergrown with other PMM. Acanthite appears heavily tarnished and fills fractures and voids within the chalcopyrite. Additional fine-grained minerals were observed in reflected light but were only identified through SEM analysis (see below). Native gold was found in an isolated region of the Outer Vein at the immediate contact (Appendix A1). It is exclusively hosted by violarite II and associated PMM and likely contains a higher Ag ratio due to its pale-yellow colouring.

Fluid inclusions are abundant in the Inner Vein (Fig. 6.1.1B), forming large voids with smaller trails extending outward vertically through the vein toward its topographic surface and in a generally northeast direction. Moving toward the Outer Vein, the inclusions decrease in size but increase in abundance and density. They become less randomly distributed and thin, vertically

oriented fluid inclusion-poor bands of chalcopyrite are observed parallel and adjacent to the silicate-rich bands (Appendix A5). The inclusions are generally restricted to being hosted in chalcopyrite and semi-transparent sphalerite and are absent from minor sulfides and PMM. Because minerals that form within fluid inclusions are often highly soluble, further investigation into their mineralogy was conducted and is detailed in Chapter 6.2.3.

6.1.3 Silicates and Related Phases

In the most interior sample (TS 1), a single grain of a mineral suspected to be pyrosmalite was identified based on its transparency and high third-order interference colours. Although pyrosmalite is not a halide, it typically contains significant chlorine (up to 4 wt.%). The presence of this mineral suggests that the abundant voids in the sample were originally occupied by fluid inclusions containing additional halides and/or liquid.

The Outer Vein contains two parallel bands of epidote and chlorite, each approximately 3-4 mm wide. These bands consist of thin epidote-rich marginal strips which transitions into an epidote-chlorite-quartz assemblage in the band centre (Fig. 6.1.2A). The first band occurs ~3.2 cm from the contact in TS 6, while the second, closer to the Inner Vein, is located ~5.5 cm from it (TS 4). The epidote in these bands is sub-rounded to euhedral and average 200 μm in size while chlorite forms elongated micaceous sheets ~75 μm in length and quartz occurs as anhedral masses, lacking undulose extinction. The Contact Zone contains two less distinct epidote-rich bands bounding either side of the vein-contact-host transitions. These epidote bands are dissimilar to those within the sulfide vein, containing coarser, more randomly oriented and deformed grains (Fig. 6.1.2B). These epidotes show poikilitic texture and unusual grain morphologies usually associated with recrystallization deformation. Unlike the well-defined bands in the vein, the epidote-rich bands in the Contact Zone appear diffuse, gradually transitioning into quartz-rich domains (Fig. 6.1.2B, C; Appendix A5).

Minor (<10 μm) intergrowths of hessite and tsumoite hosted by violarite II are observed in the Si-rich bands in the Outer Vein but lack PGM. In contrast, the epidote in the Contact Zone hosts the Au-bearing composite PGM grains in violarite II described previously in Chapter 6.1.2 (Fig. 6.1.1C). The outermost epidote-rich band contain a minor increase in the abundance of Ni-bearing sulfides compared to the rest of the chlorite-rich surroundings.

In addition to the chlorite occurring as inclusions within the vein, a very fine-grained, Fe-rich chlorite, which exhibits anomalous green interference colours under crossed-polarized light (Fig. 6.1.2C), dominates (~85 vol.%) the matrix of the Contact Zone body. Evidence of ductile deformation is observed throughout this zone, affecting both the included mineral phases and the chlorite matrix. A well-developed schistose foliation occurs oriented subparallel to the contact. A darker green chlorite forms anastomosing veinlets within the body, ranging from <1 to 4 mm wide,

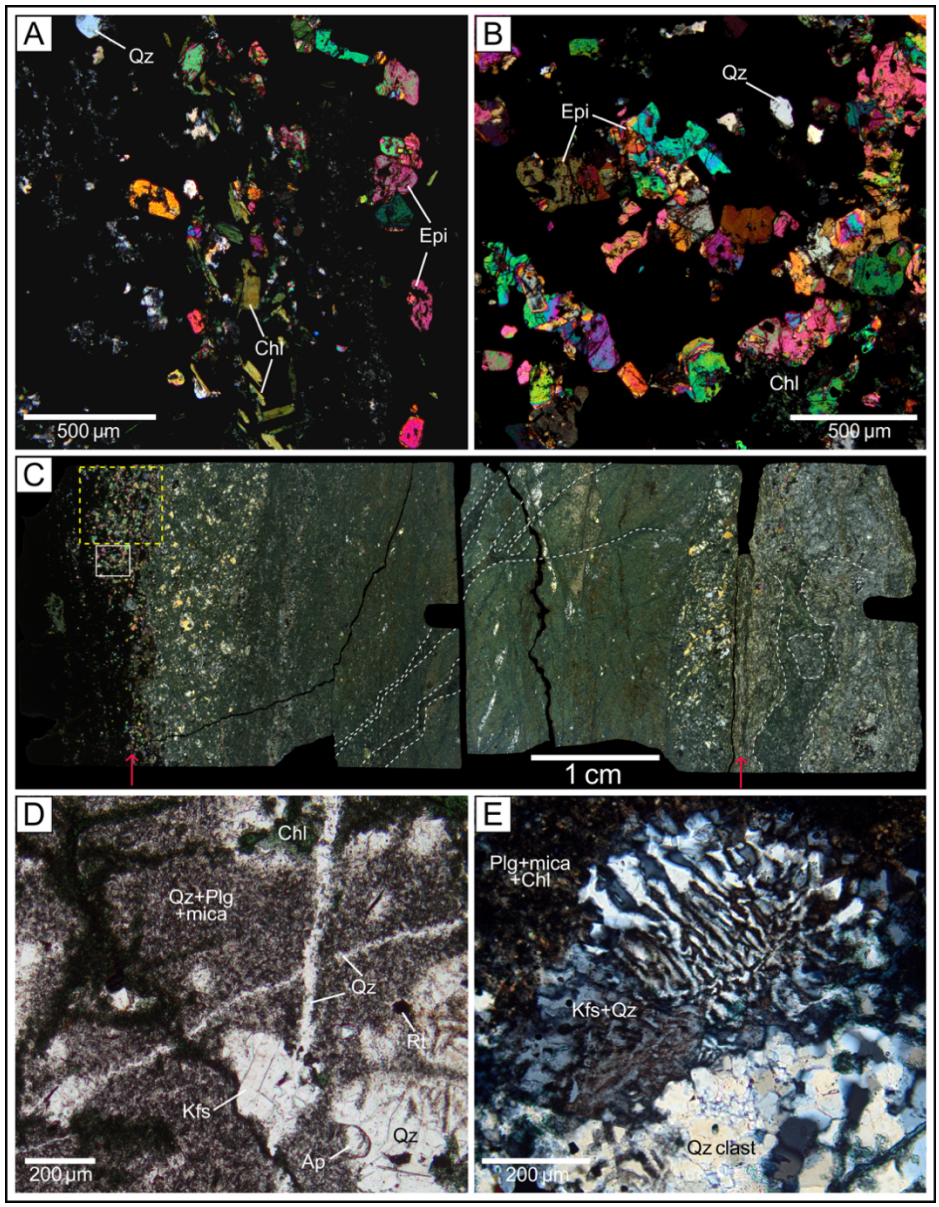

Figure 6.1.2 Photomicrographs of the silicate textures. Images are in crossed polarized light unless specified. A) Epidote, chlorite, and quartz from within the vein (TS 6) showing growth in a vertical direction. B) Epidote located at the immediate contact (TS 7). Epidote is more anhedral and poikilitic than those shown in A with a horizontal orientation. White box in C highlights the location where B was taken. C) Scans of TS 7 and 8 showing the entire Contact Zone from sulfide vein to gneiss. Red arrows indicate the locations of the Contact Zone epidote bands. White dashed lines highlight the pathways of the darker green chlorite that overprints the foliation and sinistral shear. Yellow box indicates the location of the Au ± PGM in the immediate contact band (Fig 6.1.1C). D) Plane polarized image of intensely altered gneiss in TS 10. A single lath of alkali feldspar is preserved in a small clast. Two micro-quartz veins intrude the fine-grained quartz and sericitized plagioclase and clast. Chlorite crosscuts the quartz veins and deflects around the clast. E) Common appearance of the granophyric intergrowths nucleating from a quartz-rich clast within the gneiss (TS 15). See Table 6.1 for mineral abbreviations.

(Fig. 6.1.2C) and vertically to sub-vertically crosscut the primary foliation. Pervasive chlorite veining in the gneissic host is optically similar to this darker-coloured chlorite and generally follows the same pathways, weakly crosscutting and deflecting around quartz-rich "clasts" in the gneiss (Fig. 6.1.2D). Moving further outward away from the contact, chlorite in these veins exhibits an anomalous deep blue interference colour under crossed-polarized light (Appendix A2), suggesting a compositional difference relative to the main Contact Zone body but compositional similarity to the darker chlorite veins.

Quartz within the Contact Zone displays deformation microstructures indicative of subsolidus strain accommodation, including undulose extinction, grain boundary migration, and the development of quartz ribbons aligned with the sinistral shear planes (Fig. 6.1.2C). The quartz "clasts" within the gneiss show undulose extinction and grain boundary migration but lack obvious kinematic indicators. These clasts contain few well-preserved alkali feldspar crystals (Fig. 6.1.2D), and two preserved plagioclase laths that exhibit simple twinning. The gneiss shows intense recrystallization related to partial melting with abundant granophyric intergrowths nucleating from the clasts (Fig. 6.1.2E). Potassium feldspar, which typically appears transparent to slightly pinkish, exhibit an anomalous brown hue in plane transmitted light, likely due to the effects of multiple hydrothermal events. The fine-grained plagioclase component of the gneiss appears to have been pervasively sericitized (Fig. 6.1.2D, E), and in some areas has been completely replaced by muscovite. Micro-quartz veins are also present (Fig. 6.1.2D), crosscutting both the intensely altered groundmass and quartz clasts, but are overprinted by the later chlorite (blue) veining, indicating multiple generations of fluid flow events.

Accessory phases include apatite and zircon, both of which appear evenly distributed throughout the rim and the gneissic host. Apatite inclusions in the Contact Zone are large (up to 300 μm) and frequently exhibit deformation textures, including shearing, fracturing, and boudinage, often forming elongated, fish-like morphologies. Apatite in the gneiss is subhedral and does not exceed 100 μm in size (Fig. 6.1.2D). It does not show any similar evidence for deformation as the apatite in the Contact Zone. Zircons, in contrast, are small (<50 μm) and rounded in the Zone, and larger (up to 250 μm) in the gneiss. Aggregates of Ti-bearing minerals are commonly associated with the chloritic veins within the gneiss. Within these assemblages, euhedral rutile is commonly enclosed by ilmenite or titanite and chlorite, with fine-scale ilmenite lamellae observed within rutile.

6.2 Scanning Electron Microscopy (SEM-EDS)

Six thin sections were analyzed to confirm the compositions of minerals identified through optical microscopy and to characterize previously unrecognized or concealed phases. Additionally, fractured surfaces of thin section pieces corresponding to TS 1, 6, and 7 were examined using field-emission SEM to investigate the *in-situ* mineralogy of fluid inclusions. In total,

approximately 55 mineral phases were identified through these analyses. A complete list of minerals (Table 6.1) and their calculated typical formulae by SEM spot analysis is given in Appendix Table A6.

6.2.1 Sulfides and Oxides

The majority of common base metal sulfides and oxides exhibit compositions consistent with their ideal formulas, with two notable exceptions. Some pyrite grains display compositional zoning, with Ni-rich rims [$(Fe_{0.85}Ni_{0.15})S_2$] and Ni-poor cores [$(Fe_{1.01}Co_{0.01})S_2$]. However, this zoning does not correlate with any specific textures or mineral associations. Marcasite compositions are identical to that of pyrite ($Fe_{0.99}S_2$). Violarite was analyzed in its two forms: violarite I is Ni-rich, and violarite II is Ni-and slightly Co-enriched. Pentlandite is apparently absent from the transect despite a thorough examination of all thin sections.

Four Ni-bearing phases (<1% modal abundance) were identified within the aggregates hosted by the chalcopyrite blebs in the Contact Zone. These phases included siegenite and cobaltite-gersdorffite intergrown with millerite, pyrite, and galena (Fig. 6.2.1A), though notably, no violarite is present in these aggregates. The siegenite is particularly Ni-rich, containing 41 wt.% Ni and only 8 wt.% Co, but has characteristic optical properties (i.e., violet-grey reflectance). Galena is identified as a trace phase, occurring exclusively within the siegenite. Cobalt-bearing minerals display cubic morphology with compositions intermediate between cobaltite and gersdorffite, with ~15 wt.% each of Ni and Co.

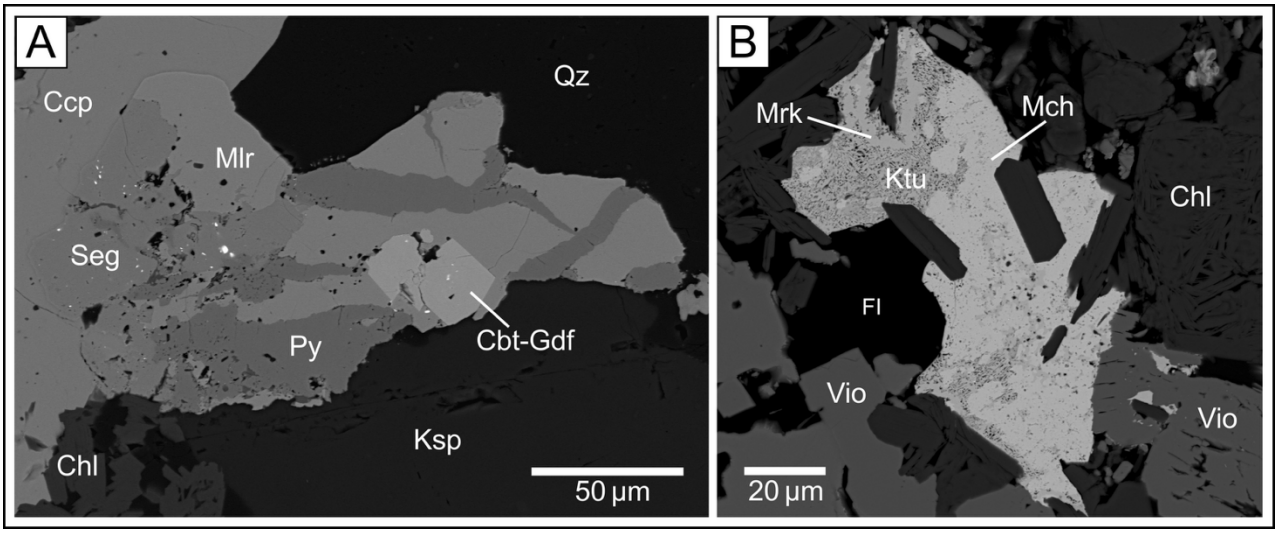

Figure 6.2.1 Backscattered electron (BSE) images of A) a Ni-rich aggregate within the exterior of the Contact Zone, highlighting the fractured cubic cobaltite-gersdorffite and bright phase (galena) within the siegenite (TS 8); B) one of the complex composite grains containing the intergrowth of Pd-Bi-Te minerals adjacent to a fluid inclusion within the Inner Vein (TS 2). See Table 6.1 for mineral abbreviations.

6.2.2 Precious Metal Minerals (PMM)

Although many PMM are readily identifiable through optical microscopy, a detailed characterization of their elemental abundances is necessary to understand precious metal enrichment within the studied vein.

As previously noted, the platinum-group minerals (PGM) identified include sperrylite, michenerite, merenskyite, and kotulskite. Sperrylite consistently exhibits its ideal formula ($PtAs_{1.98}$) regardless of grain size or location within the transect. In contrast, Pd-bearing phases (Fig. 6.2.1B) display minor compositional variations depending on their associated minerals and spatial distribution. Michenerite, the most compositionally variable, is more Bi-poor (~43 wt.%) when present in complex composite grains and more Bi-rich (~48 wt.%) when occurring as isolated grains within chalcopyrite. Among the three Pd-bearing phases, michenerite contains the lowest Pd content (~24 wt.%).

Merenskyite primarily hosts intergrowths of kotulskite and/or hessite, both of which are Te-rich, or matildite, which is Bi-rich. When intergrown with other PGM, merenskyite lacks detectable bismuth. However, when associated exclusively with hessite and matildite, it contains up to 8 wt.% Bi. Notably, hessite and matildite do not incorporate bismuth or tellurium, respectively. Kotulskite is the most Pd-rich phase, containing up to 42 wt.% Pd, and also tends to be Bi-rich. It was observed exclusively intergrown with merenskyite and michenerite, without hessite or matildite.

Regarding Bi-bearing phases, tsumoite consistently exhibits its ideal composition ($Bi_{1.03}Te_{0.98}$). Additionally, hedleyite was revealed as Te-rich (~22 wt.%), and minute occurrences of native bismuth were identified in backscattered electron (BSE) imaging. Other rare Bi-Te phases were identified exclusively through BSE, including sulphotsumoite, which was observed as a single grain within chalcopyrite, and tellurite, the latter an oxidation product of hessite.

The composition of matildite is more commonly between matildite (S-rich) and its other endmember, bohdanowiczite (Se-rich). Similarly, tetradymite typically formed compositions intermediate with kawazulite, the Se-rich endmember. A few fractures in chalcopyrite were filled with acanthite and more rarely, its Se-endmember naumannite, were intergrown with covellite. No notable spatial relationship was observed between the S±Se endmembers and their distribution within the channel. The purity of the native gold observed at the vein contact varied from 70 to 93 wt.% Au with 7 to 30 wt.% Ag, with an average ratio of $Au_{0.67}$:$Ag_{0.33}$.

6.2.3 Fluid Inclusions

Five distinct Cl-bearing phases were identified in association with base metal sulfides and oxides. The spatial distribution of inclusions across the vein was previously described in Chapter 6.1. Both primary fluid inclusions and daughter minerals are observed within the massive chalcopyrite. Among the fractured samples, that associated with TS 1 exhibits the highest abundance of inclusions and textures. This section also contained ferropyrosmalite, initially identified through optical microscopy and subsequently confirmed via SEM-EDS.

The chalcopyrite displays a notably porous texture, which may be a consequence of inclusion decrepitation. This texture forms distinct trails leading to or from the daughter minerals, suggesting their involvement in the release and entrapment of vapour phases within the sulfide. Minute cross-cutting exsolution lamellae are observed on the fractured surfaces of TS 7. SEM-EDS analysis revealed that these exsolutions had a composition nearly identical to the analyzed chalcopyrite, with minor but consistent deviations in copper and iron (39 wt.% Cu, 25 wt.% Fe, ~35 wt.% S). Based on these compositional variations and the exsolution textures, we interpret these lamellae as Cu-enriched cubanite exsolving from chalcopyrite. A photomicrograph of this texture is provided in Appendix A3. Small, rounded grains (< 5 μm) of ideal cubanite were also identified within the massive chalcopyrite with a typical formula of $Cu_{1.1}Fe_{2.1}S_3$. No cubanite was confirmed in TS 1 or TS 6.

A limited number of primary liquid-filled inclusions were identified (Fig. 6.2.2A), primarily in TS 1, with fewer observed in the other two samples. Upon fracturing, these inclusions precipitated rims of irregular thickness within the open cavities. Spot analysis of these precipitates revealed a composition enriched in Na, Cl, Fe, Zn, and Ca with trace amounts of Pb, Mn, and K. These inclusions also contain solid phases, most commonly sphalerite or galena, with one instance of halite. Optical microscopy confirmed the presence of both vapour and solid phases within semi-transparent sphalerite.

Daughter minerals are secondary phases that crystallize from the fluid or melt released during decrepitation of a fluid inclusion, forming within the vacant cavity. Five Cl-bearing phases are consistently associated with one or more base metal sulfides and oxides as daughter minerals, with less than 30% of the total number of inclusions being Cl-free. The sulfides and oxides exhibit well-defined euhedral morphologies and largely retained their expected stoichiometric compositions. The most commonly associated phases are sphalerite, magnetite, cassiterite, pyrrhotite, and chlorite. Sphalerite typically forms tetrahedral or tabular grains and is often Cd-bearing, up to 2 wt.%. Magnetite is observed as modified dodecahedral crystals, occasionally flattened, while pyrrhotite occurs as large, anhedral masses with striated faces (Fig. 6.2.2C). Cassiterite is observed in fragile acicular laths. Where chlorite is present within inclusions, it forms thin platy prisms or fills the remaining cavity space.

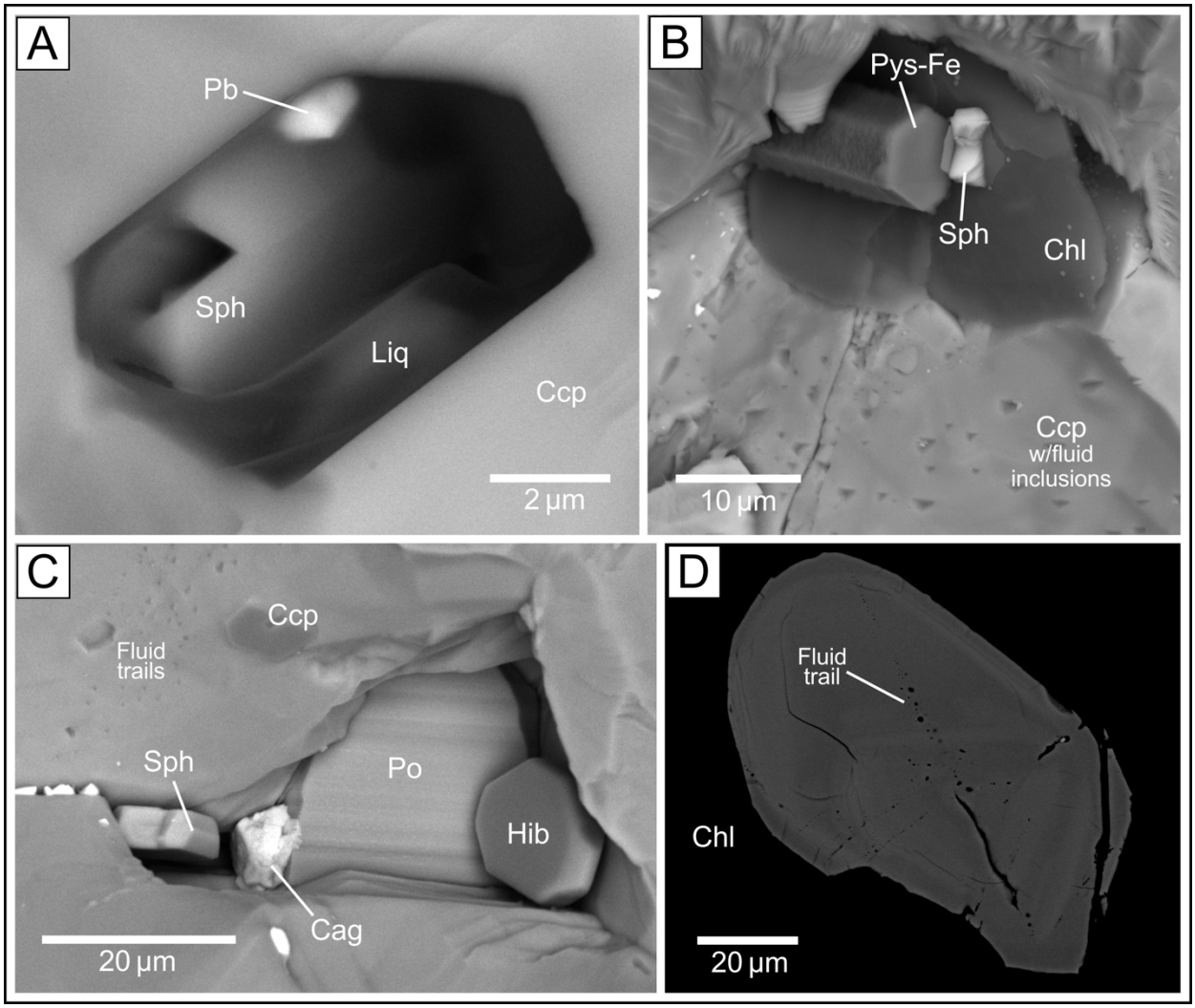

Figure 6.2.2 Backscattered electron (BSE) images of A) a liquid-filled inclusion showing the precipitated rim, labeled as Liq. Lead and sphalerite were both found within this inclusion; B) Euhedral ferropyrosmalite with associated sphalerite and chlorite as daughter minerals; C) Massive pyrrhotite with euhedral hibbingite and sphalerite with chlorargyrite; D) Zircon from TS 14 showing weak zoning and fluid trails radiating from its center.

The identification of large pyrrhotite masses is consistent with optical observations where pyrrhotite hosted tsumoite and sperrylite. Although no PGM were identified in the fractured surfaces or within the fluid inclusions, their presence may be indirectly inferred by their incorporation within larger base metal sulfides in the daughter minerals.

Among the Cl-bearing minerals, ferropyrosmalite (Fig. 6.2.2B) is the most abundant and exhibits the largest grain sizes, ranging from <5 µm to approximately 50 µm, with one exceptional grain reaching 250 µm in size, identifiable with a hand lens as a hexagonal stubby prism. The chlorine content in ferropyrosmalite averaged around 5 wt.%, consistent with previously reported

values for ferropyrosmalite from McCreedy East (Dare et al., 2014). Ferropyrosmalite in TS 1 closely matches the chlorine content identified in fluid inclusions, containing 4.9 wt.% Cl. The second most abundant Cl-bearing phase was cubic halite, which is compositionally dominated by chlorine but also contains minor metals, most commonly ~2 wt.% Ca and <1 wt.% Mn. Halite locally contains up to 3 wt.% Ag, as well as palladium enrichment in two instances (4.1 wt.% and 0.6 wt.%). Element mapping of a third grain suggests palladium enrichment, though the accompanying spot analysis yields conflicting results (Appendix A4). Given the limited sampling area, it is considered likely that Ag- and Pd-bearing halite is more widespread throughout the massive sulfide.

Hibbingite was the third major halide phase identified, occurring as tabular grains of daughter minerals (Fig. 6.2.2C). SEM-EDS analysis confirmed its composition with iron and chlorine as the dominant elements [$Fe_{1.9}(OH)_{2.7}Cl_{1.4}$], consistent with previously reported occurrences of hibbingite in hydrothermal environments (e.g., Saini-Eidukat et al., 1994). Notably, ferrous hydroxychloride has been identified in other sulfide-rich settings within Sudbury, including the Strathcona Deep Copper Zone, where it occurs as an alteration product associated with chloride-bearing hydrothermal fluids (Springer, 1989; Farrow et al., 1994).

Chlorargyrite is observed as a minor Cl-bearing daughter mineral, occurring as small crust- or film-like coatings nucleating on or near base sulfides within the fluid inclusions. Analysis revealed a typical composition of ~80 wt.% Ag and ~20 wt.% Cl. One irregular grain has a composition of ~80 wt.% Ag, ~14 wt.% Cl, and ~5 wt.% I (Fig. 6.2.2C), suggesting the incorporation of iodine into the structure. The presence of iodine is noteworthy, as halide substitutions in chlorargyrite are typically limited, and I-bearing silver halides are rarely documented in magmatic-hydrothermal systems. Although Ag-Cl phases have been identified in other hydrothermal systems, no previous studies have reported chlorargyrite in Sudbury ore deposits. This may therefore represent the first documented occurrence of chlorargyrite within the Sudbury Igneous Complex.

The least abundant and smallest halide identified is cotunnite, occurring as floret-like aggregates of flattened, tabular crystals within smaller inclusions. These aggregates are typically less than 5 μm in size and were not observed to be associated with other halide phases. Other non-halide minerals that were found within these inclusions include thin prismatic anhydrite and kaolinite surrounding the interior of the cavity.

6.2.4 Silicates and Related Phases

Due to the fine-grained nature of the Levack gneiss, accurately determining the mineral compositions was challenging. Identification relied on the rare well-preserved grains and petrographic textures.

In the vein, epidote, chlorite, and quartz dominate the silicate assemblage, each exhibiting minimal compositional variation from their ideal formulas. In the gneiss, analysis of the granophyric intergrowths confirms the presence of microcline and quartz. Outside these intergrowths, a few plagioclase grains were analyzed and confirm that the matrix is primarily composed of fine-grained plagioclase, muscovite, and quartz. The two preserved plagioclase laths analyzed within the gneiss gave compositions of $Ab_{95}An_5$ and $Ab_{65}An_{35}$. Both showed a depletion in Al and Si, with 59 and 51 wt.% SiO_2, and 20 and 25 wt.% Al_2O_3, respectively, likely due to its intense sericitization.

Some zircons showed weak concentric zoning in BSE with what appears to be overprinting fluid trails radiating outwards from the zoned core (Fig. 6.2.2D). The location of these zircons is not restricted to just the fine-grained chlorite area of the Contact Zone but are also found within the gneiss. Accessory apatite in both the Contact Zone and gneiss is F-rich (~3 wt.%) with no detectable chlorine.

The Ca-Ti aggregates, confirmed to contain rutile, titanite, and ilmenite within the gneiss contain significant barite and trace amounts of monazite-Ce. Titanite frequently contain up to 1.5 wt.% F while the other Ti-bearing phases are F-poor. In one instance, barite forms the interstitial material binding multiple rutile grains within a ~100 μm diameter area. Monazite-Ce occurs in a former cavity within the gneiss as acicular splays radiating from a rutile grain and in close proximity to apatite. The monazite exhibits a rare earth element (REE) composition of 22 wt.% Ce, 13 wt.% La, 8 wt.% Nd, and 1 wt.% Sm, typical of this mineral.

6.3 Micro-XRF Mapping

A micro-XRF (μXRF) phase map was produced across the chlorite-rich Contact Zone between the massive chalcopyrite vein and the adjacent gneissic metabreccia (Fig. 6.3). Additional phase and element maps are provided in Appendix A9.

The Zone is dominated by chlorite which forms the matrix for much of the mapped area. Chlorite defines a penetrative foliation that encloses quartz blebs, titanite grains, and sulfide aggregates. The orientation of the foliation is broadly consistent across the map, with local deviations within the sulfide vein.

The massive chalcopyrite vein contains localized epidote at its margin. These epidote veinlets extend no more than ~0.5 cm into the sulfide with limited deformation features that likely occurred synchronous or slightly post-kinematic to sulfide crystallization and strain localization. Outside of the main sulfide vein, chalcopyrite displays a lobate morphology aligned parallel to both the immediate contact and the chloritic foliation. Violarite is concentrated along the Lower transect (Fig. 6.1) of the map, primarily between the main sulfide body and its parallel chalcopyrite

stringers. The sulfides are associated with elevated concentrations of accessory minerals, including titanite and apatite, relative to the broader chloritic matrix.

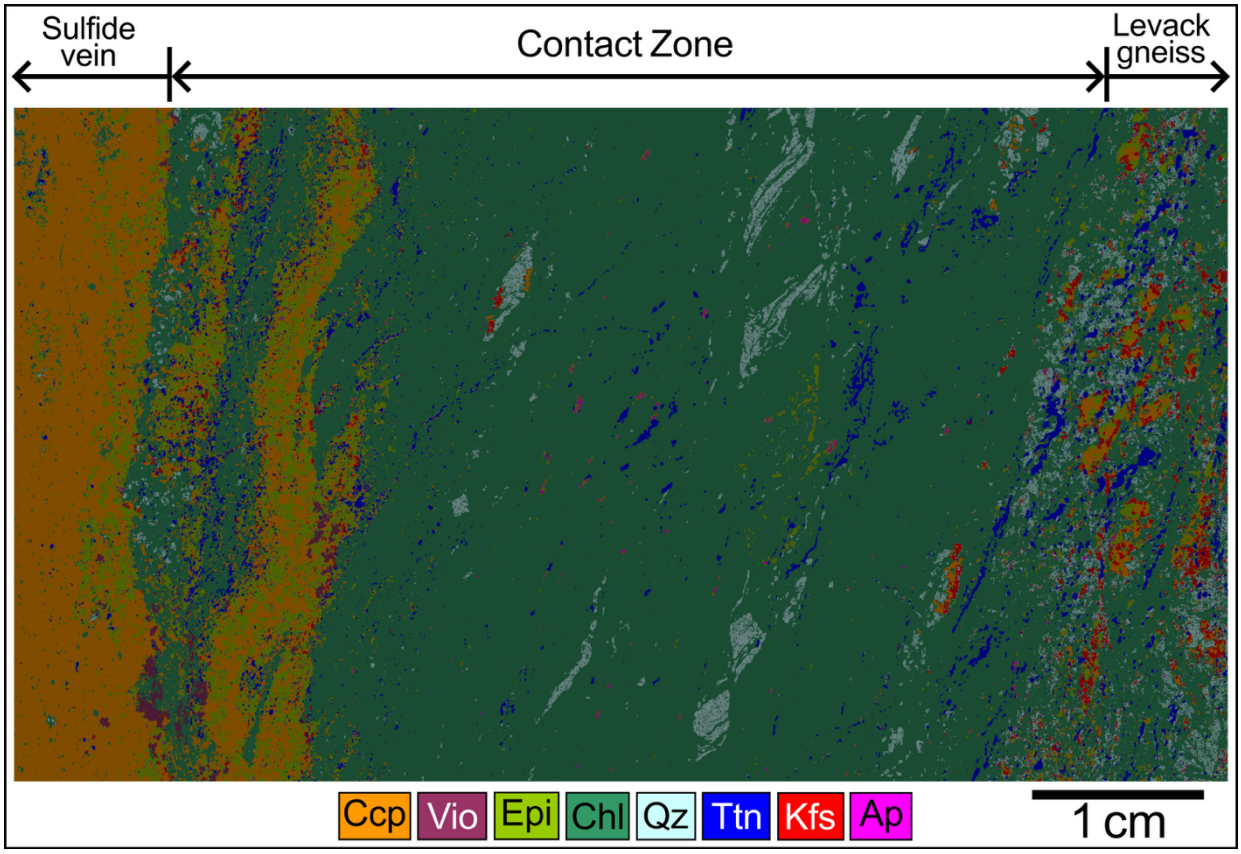

Figure 6.3 Micro-XRF phase map of the chlorite-rich Contact Zone between the massive chalcopyrite vein and gneissic metabreccia.

Epidote occurs as diffuse patches and irregular streaks, particularly within or adjacent to sulfide-rich domains. Quartz is present as foliation-parallel grains, ribbon-like pods, and elongate blebs distributed throughout the chlorite matrix. Titanite appears intergrown with the chloritic matrix, often branching outward from sulfide margins and, in some cases, aligning with the foliation. These branching textures correspond to areas of anastomosing darker chlorite observed in Chapter 6.1.3. Apatite occurs as scattered grains within the chloritic matrix, with occasional enrichment near the sulfide margins. Alkali feldspar, although largely relict, exhibits a weak alignment to the foliation.

The mineralogical assemblage reflects a strong alteration signature associated with sulfide vein emplacement, characterized by chlorite-dominant replacement of original silicate phases and localized enrichment in epidote, titanite, and apatite.

6.4 Electron Probe Micro-Analysis (EPMA)

Three lateral transects across the vein contact were set up in four thin sections (TS 6, 7, 8, 10) to analyze the compositional variation of chlorite and epidote. Each transect, Upper, Middle, and Lower (Fig. 6.1), measures approximately 0.8 cm in thickness and is evenly distributed along the short axis of each section. Spot locations were chosen via optical microscopy to ensure the analysis focused exclusively on chlorite and epidote and avoided the inadvertent analysis of other phases. The full datasets for both chlorite and epidote, as well as transect point locations, are provided in Appendix Tables A7 and A8.

6.4.1 Chlorite

The chemical composition of chlorite was characterized across 44 grains: Upper (n=17), Middle (n=12), and Lower (n=15). The analyses yielded a composition consistent with chamosite, the Fe-rich variety of chlorite. Most elements exhibit a relatively homogeneous distribution over the transect, with elemental variations not exceeding 3 wt.% for SiO_2, Al_2O_3, FeO, MgO, NiO, MnO, TiO_2, CaO, K_2O, Cl^-, and H_2O. The variation in the calculated empirical formula of chamosite for each of the transects is given in Table 6.4.1.

Table 6.4.1 Ranges for the calculated empirical formula for chamosite split by transect location. Formula based on 18 O.

Transect location	Calculated Formula
Upper	$(Fe_{3.3\text{-}3.9}Mg_{0.8\text{-}1.4}Al_{1.1\text{-}1.4}Ni_{0\text{-}0.1})_6\,(Si_{2.5\text{-}2.7}Al_{1.3\text{-}1.5})_4\,O_{10}(OH)_{8.0\text{-}8.6}$
Middle	$(Fe_{3.2\text{-}4.1}Mg_{0.6\text{-}1.6}Al_{0.9\text{-}1.5}Ni_{0\text{-}0.1})_6\,(Si_{2.6\text{-}2.8}Al_{1.2\text{-}1.4})_4\,O_{10}(OH)_{8.0\text{-}8.2}$
Lower	$(Fe_{3.4\text{-}4.2}Mg_{0.5\text{-}1.3}Al_{1.1\text{-}1.3}Ni_{0\text{-}0.1})_6\,(Si_{2.6\text{-}2.7}Al_{1.3\text{-}1.4})_4\,O_{10}(OH)_{8.1\text{-}8.2}$

A key trend observed involves MgO, FeO and NiO (Fig. 6.4.1A). The Mg# $\left(\text{Mg\#} = \frac{\text{MgO}}{\text{FeO+MgO}}\right)$ averages 0.16, exhibiting two anomalous points and a gradual increase towards the gneiss. The lower Mg# values correspond to chlorite inclusions within the massive sulfide, outside of the epidote-chlorite bands. These points show an inverse relationship with nickel, i.e., lower Mg# values coincide with elevated Ni concentrations.

At the Contact Zone, Mg# values remain relatively consistent. Moving outward towards TS 10 (from ~24 cm), Mg# shows a gradual increase to 0.22. It is worth noting that this trend is also visible optically, as interference colors in crossed-polarized light shift from green in the Contact Zone to deep blue in the gneiss, suggesting an increase in magnesium content.

Overall, chlorite exhibits a decrease in nickel, following a negative trend, with higher nickel concentrations at the exterior of the Contact Zone. The nickel peak coincides with the

location of the clast-rich margin at the boundary between the Zone and the gneiss. As noted in Chapter 6.1, this area also shows a slight increase sulfide abundance, which may explain the nickel anomaly. However, no direct correlation was observed between Ni and Mg# in this context.

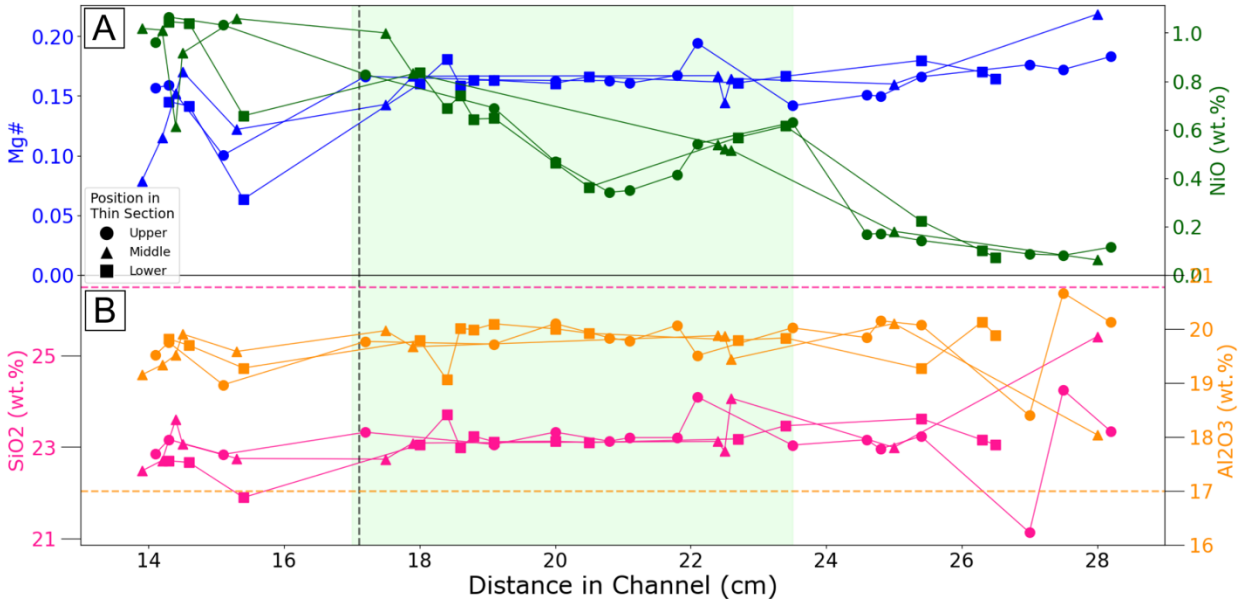

Figure 6.4.1 EPMA data for chlorite by distribution of spot analysis along channel from TS 6 to 10. Green shaded box indicates the extent of the Contact Zone and vertical dashed line, the location of the sulfide-gneiss contact. Horizontal pink and orange dashed lines show the typical wt.% for SiO_2 and Al_2O_3 in chamosite, respectively.

Another notable variation is the consistent enrichment in aluminum and depletion in silica relative to the ideal chamosite formula shown by the corresponding horizontal lines (Fig. 6.4.1B). Outside the Contact Zone, SiO_2 and Al_2O_3 exhibit parallel trends, increasing and decreasing in unison. Within the Contact Zone, these elements are relatively homogeneous, except for a single inverted anomaly per transect, each corresponding to a quartz-rich zone within the chlorite.

Chlorite is often analyzed for its chlorine content in fluid-related studies, which was a primary motivation for this analysis. However, chlorine concentrations in the studied chamosite were negligible, with values consistently <0.03 wt.% or below detection limits.

6.4.2 Epidote

A total of 42 analytical points were collected to determine epidote compositions across the three transects: Upper (n=15), Middle (n=10), and Lower (n=17). The results yield an average empirical formula approximating $Ca_{2.03\text{-}2.04}Al_{2.00}(Fe_{0.91\text{-}0.93}Al_{0.22\text{-}0.24})(SiO_4)(Si_{2.08}O_7)O(OH)_{1.04}$ closely aligning with ideal epidote stoichiometry.

CaO concentrations remain relatively constant throughout the channel, exhibiting only minor fluctuations (Fig. 6.4.2A). Fe_2O_3 follows a similarly consistent trend, and no distinct correlation with CaO is observed. The minimal variability in these elements suggests a lack of significant compositional zoning within the epidote. In contrast, SiO_2 and Al_2O_3 display greater variability (Fig. 6.4.2B), though no systematic inverse or direct relationship is observed. While localized fluctuations occur, no clear compositional trend emerges across the channel for epidote.

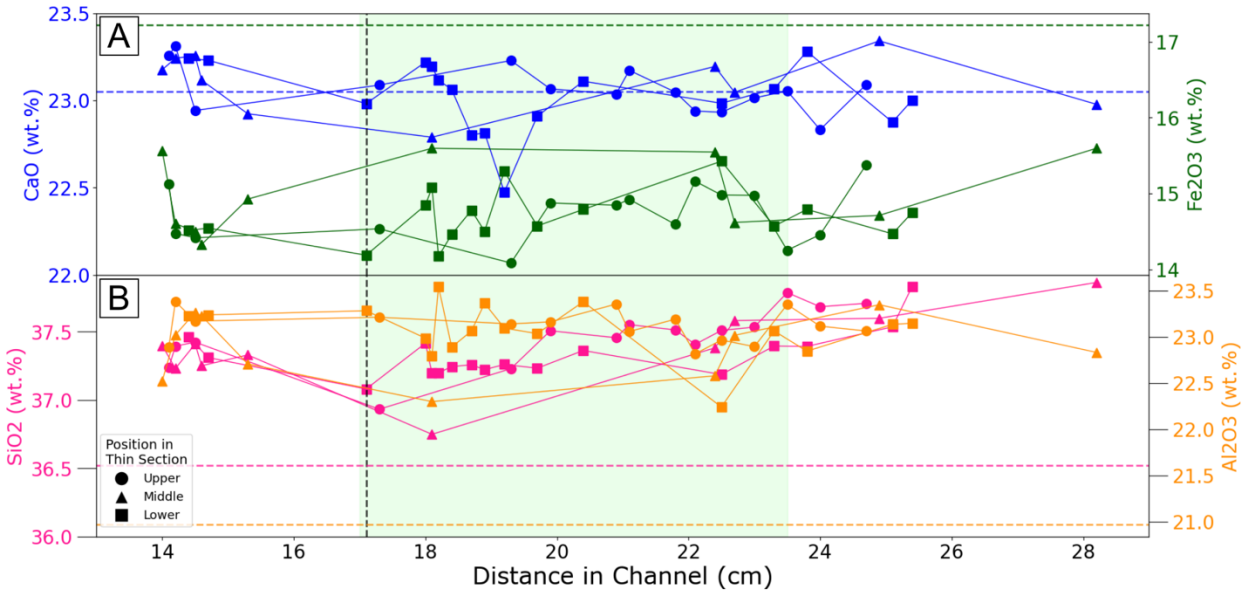

Figure 6.4.2 EPMA data for epidote by distribution of spot analysis along channel from TS 6 to 10. Green shaded box indicates the extent of the Contact Zone and vertical dashed line, the location of the sulfide-gneiss contact. Horizontal blue and green dashed lines show the typical wt.% for CaO and Fe_2O_3, and pink and orange lines for SiO_2 and Al_2O_3, respectively in epidote.

Minor deviations in element concentrations are observed at specific distances (~16 cm and ~22-24 cm in the Contact Zone), potentially reflecting subtle compositional heterogeneities or microstructural influences. However, the overall consistency in Ca-Fe-Al-Si proportions indicates that the epidote is compositionally homogeneous, with no evidence of major cationic substitution trends.

6.5 Sulfur Isotopes

Chalcopyrite was sampled in 44 locations corresponding to the opposing thin section faces, along the same transects as the EPMA analyses (Fig. 6.1), dividing the channel into three paths – Upper, Middle, and Lower – spanning the massive sulfide vein (TS 1-7), the Contact Zone (TS 7-8), and a single section within the gneiss (TS 9). Sampling within the gneissic host was limited due to low chalcopyrite abundance. The full dataset for $\delta^{34}S$, as well as transect locations, are provided in Appendix Table A10.

The measured $\delta^{34}S$ values range from approximately 4‰ to 6‰, with an analytical precision of ±0.3‰ (Fig. 6.5.1), yielding an average of 5‰ ± 0.3‰. Most values fall slightly above the upper limit of the $\delta^{34}S$ range reported by Ripley et al. (2015) for footwall silicates in the Whistle mine, indicated by the shaded grey region in Fig. 6.5.1, but do fall within the range reported by MacInnis et al. (2014) for chalcopyrite in the Podolsky 2000 deposit (blue shaded box). However, several data points, particularly between ~11 and 24 cm, exceed these upper bounds, with distinct peaks at ~12 cm and ~22 cm. Given that sampling conditions, including consistent sample weights and conscientious avoidance of silicate phases, this anomaly cannot be attributed to analytical or procedural error. A pronounced drop to 2.3‰ at ~16 cm marks the lowest $\delta^{34}S$ value recorded in this study. This anomaly is likely due to sub-surface epidote inclusions and is disregarded from further consideration. Overall, the $\delta^{34}S$ values exhibit a weak increasing trend across the channel, interrupted by localized fluctuations.

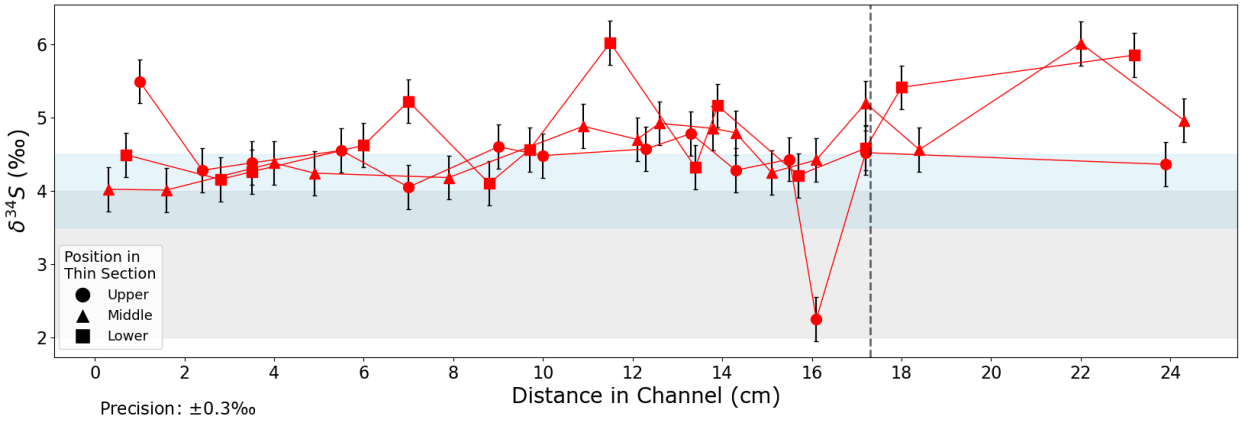

Figure 6.5.1 $\delta^{34}S$ isotope data for chalcopyrite by distribution of drill points along the channel from vein to Contact Zone, TS 1 to 9. Grey shaded area indicates the range of 2‰ to ~4‰ reported by Ripley et al. (2015) and the blue area is the range of 3.5‰ to ~4.5‰ reported by MacInnis et al. (2014). The vertical dashed line indicates the location of the sulfide-gneiss contact. Error bars indicate analytical precision of ±0.3‰.

7. Discussion

7.1 Crystallization history of the massive sulfide vein

Although the crystallization history of monosulfide solid solution (MSS) is relatively well constrained (e.g., Barnes et al., 1997; Ballhaus et al., 2001; Mungall et al., 2005; Dare et al., 2010; Dare et al., 2011), the lower temperature evolution of intermediate solid solution (ISS) and, in particular, the late-stage, volatile- and metal-enriched residual sulfide liquid remains less well understood (Dare et al., 2014; Mansur et al., 2021). Tensional zones in the Podolsky North Zone, such as those at the margins of metabreccia clasts enclosed by IQD, provided conduits and open spaces for the accumulation and rapid crystallization of Cu-rich massive sulfide melts (Carter, 2005). This section outlines the crystallization sequence of these massive sulfide veins, focusing on post-emplacement processes and prior to the influence of exsolved magmatic or hydrothermal fluids. A schematic illustration summarizing the mineralogical and textural changes from Inner Vein to Contact Zone described in Chapter 6, is provided in Fig. 7.1.1.

Crystallization at the North Zone began with the ISS, where an intercumulus sulfide melt became trapped between growing ISS grains. Due to their low partition coefficients into MSS and ISS (Barnes et al., 1997; Ballhaus et al., 2001), the intercumulus liquid was progressively enriched in highly incompatible chalcophile elements, including Pd, Pt, Ag, Au, TABS (Te, As, Bi, Sb, Sn), and volatiles such as Cl and F, which could not be accommodated within the crystallizing ISS lattice (Mungall and Brenan, 2003; Mungall et al., 2005; Dare et al., 2014; Mansur et al., 2021). This elemental exclusion set the stage for extensive differentiation between the crystallizing ISS and the evolving intercumulus melt.

As ISS continued to crystallize and exsolve chalcopyrite, residual sulfide liquid flowed inward toward the center of the vein (Fig.7.1.2A). This migration produced the observed higher concentration of accessory ore minerals in the Inner Vein relative to the Outer Vein margins of the studied channel. The migration may also explain the Contact Zone's observed deformation (see descriptions in Chapter 6.1.3 and 6.3). Centralized lateral flow of the liquid center caused tension on the semi-solid chalcopyrite vein margin, causing recrystallization of the chalcopyrite to occur, contributing to parallel fractures (now filled with epidote) in the Outer Vein and the strain-related features of silicates observed in the μXRF map of the Contact Zone.

At approximately 900°C, magnetite began to crystallize from the intercumulus melt. The occurrence of magnetite as inclusions within pyrrhotite suggest its relatively early precipitation from the Cu- and Fe-rich residual melt phase (Fig. 7.1.2B; Naldrett, 1969; Dare et al., 2014). In general, the timing of sphalerite formation is not well constrained in the ISS. While early crystallization is possible (Kojima and Sugaki, 1984), the presence of sphalerite as a dominant daughter mineral in the observed fluid inclusions raises the possibility that most sphalerite in these samples crystallized later during fluid exsolution stages and not from the intercumulus melt.

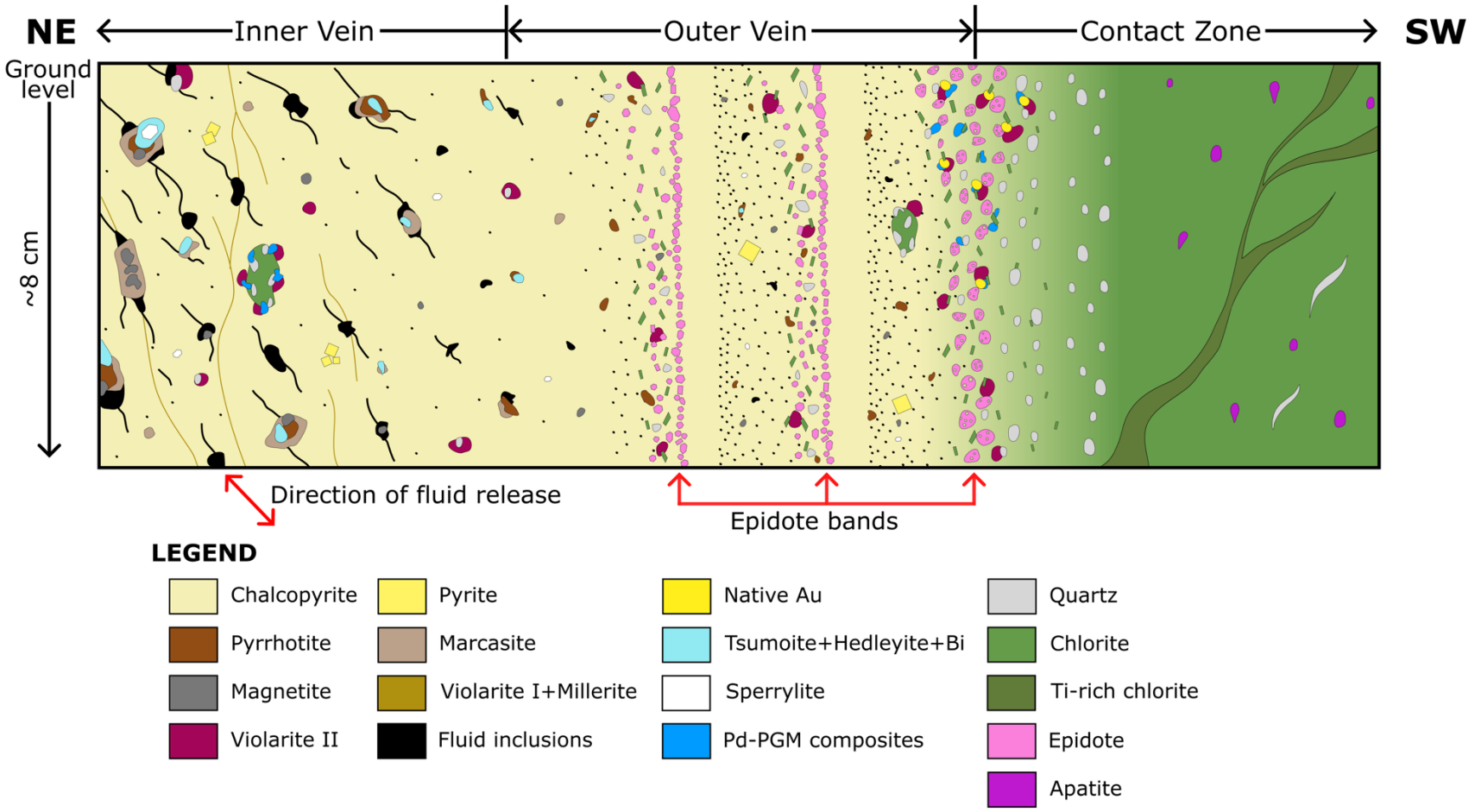

Figure 7.1.1 Schematic illustration demonstrating the mineralogical and textural changes from the Inner to Outer Vein and Contact Zone described in Chapter 6. Image is not to scale but size variations and abundances are proportional to trends observed. Note that the large fluid inclusions in the Inner Vein contain the Cl-rich daughter minerals, sphalerite and cassiterite, and additional magnetite and pyrrhotite. The fluid-related textures also include fluid trails (black lines) and empty inclusions (small black dots).

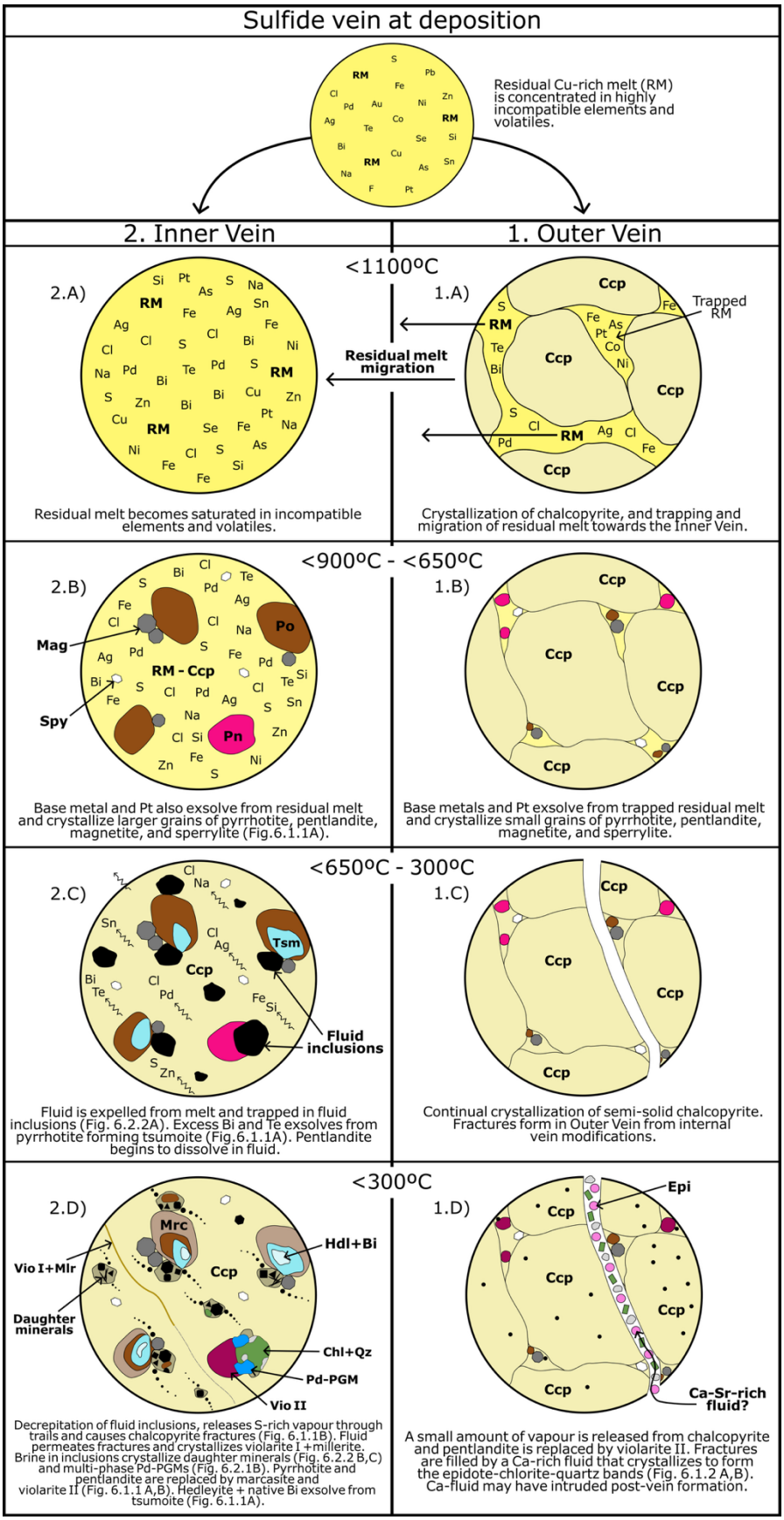

Figure 7.1.2 Schematic illustration for the crystallization sequence of the sulfide vein, separated by the processes occurring simultaneously in the Outer Vein (1.A-1.D) and the Inner Vein (2.A-2.D) at the given temperature ranges. Figures referenced within the panels indicate photomicrographs from Chapter 6. Figure uses same legend as 7.1.1. See text for further discussion.

Simultaneous with ISS crystallization, PGE partitioned into the residual sulfide melt leading to the crystallization of PGM, notably sperrylite (Fig. 7.1.2B). Euhedral sperrylite grains are distributed throughout the vein, with notably larger grains in the Inner Vein, consistent with a greater volume of residual melt in this area. The ability of sperrylite to crystallize in a fractionated sulfide melt at lower temperatures (<900ºC) is favoured by lower oxygen fugacity and higher transition metal concentrations (Fe, Ni; Bai et al., 2017). This supports its origin and distribution in the vein, forming from the trapped Cu-Fe-rich residual melt between ISS grains and the migration of this residua into the Inner Vein.

As crystallization continued, the evolving sulfide liquid appears to have undergone exsolution of Fe-Ni sulfides (e.g., Barnes et al., 2020). These elements subsequently formed pyrrhotite and pentlandite (observed in the present samples as violarite II and referred to as henceforth). The distribution of pyrrhotite, characterized by larger and more abundant grains in the Inner Vein relative to the Outer Vein, supports its derivation from the residual melt (Fig. 7.1.2B). In contrast, violarite II is randomly distributed throughout the vein, suggesting that it formed as an exsolved phase from ISS at lower temperatures (<650°C). The slight Ni- and Co-enrichment observed in violarite II, a late-magmatic alteration product of pentlandite, is consistent with the model proposed by Dare et al. (2014) to explain the partitioning behavior of nickel and cobalt between ISS and the residual melt. Experimental studies by Sinyakova and Kosyakov (2007) have shown that nickel and cobalt should become mildly enriched in the intercumulus melt from which PGM crystallize, leading to the expectation that Ni- and Co-bearing PGM would form within the composite grains. However, neither the samples analyzed in this study nor those examined by Dare et al. (2014) contain Ni-rich PGM. It was therefore suggested by Dare et al. (2014) that nickel and cobalt concentrated in small volumes of trapped residual liquid reacted with and enriched the ISS, from which later pentlandite exsolved, rather than crystallizing directly from the residual melt. This aligns with our presented samples, providing the mechanism to account for the observed textural differences and the Co-depletion in violarite I compared to violarite II, where violarite I-millerite veins were instead formed from the residual melt or a late-magmatic fluid.

Subsequent cooling of the residual sulfide melt to between approximately 600°C and 300°C facilitated the formation of complex PGM assemblages within violarite II, and PGE-poor precious metal minerals (PMM) phases (e.g. hessite and tsumoite) in pyrrhotite ± marcasite. This could have been achieved by either one or a combination of the following ways: (1) co-crystallization with pyrrhotite and violarite II; (2) PMM were initially present as nano-inclusions which were melted and migrated within the grains by circulating late-magmatic fluids; or (3) PMM were initially crystallized directly from the residual melt and were locally remobilized by late-magmatic fluids.

Based on the observed spatial distribution of Bi-tellurides within pyrrhotite, it is suggested that their formation is most consistent with option 2 (Fig. 7.1.2C). Tsumoite is frequently located

in the center of pyrrhotite grains, often enclosing hedleyite and native bismuth, thereby increasing the bismuth concentration within the core. This pattern may result from inward, low-temperature melting – initiated by magmatic fluids – of PGE-poor PMM nano-inclusions within pyrrhotite. This process would facilitate the removal of these inclusions from the grain boundaries, allowing bismuth and some tellurium to migrate toward regions with lower temperature gradients and subsequently crystallize there (Fig. 7.1.2D). The typical composition of the Pd-Bi-Te minerals analyzed during this study are plotted on the Pd-Bi-Te phase system at 489ºC in Fig. 7.1.3. These same fluids may also have induced the replacement of pyrrhotite by marcasite. If the PMM had formed by either of the other two proposed mechanisms, a distinct zonation of bismuth within pyrrhotite would not be expected.

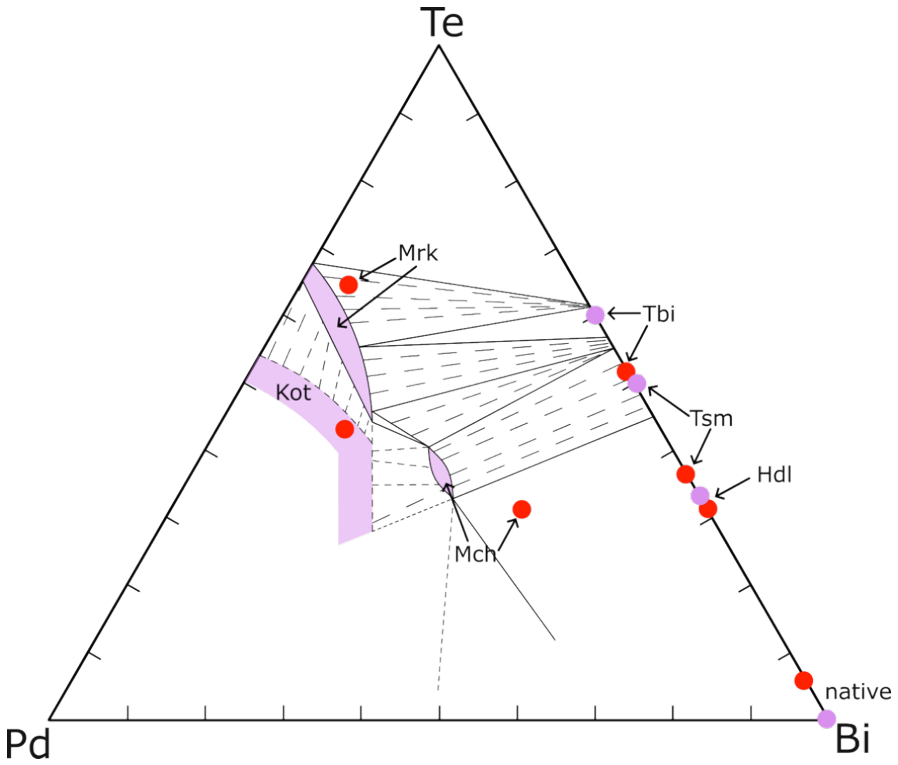

Figure 7.1.3 Selected portion of the Pd-Bi-Te phase system at 489ºC. Purple shaded areas and points represent the stability fields for the given minerals. Red points represent the average abundances of the same phases found in this study. Based on Hoffman and MacLean (1976) and Makovicky (2002). Refer to Table 6.1 for mineral abbreviations.

The spatial variation in PGM assemblages complicates the determination of their precise crystallization pathway. In the Inner Vein, composite grains consisting of michenerite, merenskyite, kotulskite, and hessite are associated with the margins of violarite II. In contrast, PGM in the Outer Vein include matildite and native gold and are not associated with violarite II. This distribution suggests that PGM likely crystallized through a complex interplay of options 2 and 3. Option 1 is considered less probable, as small, isolated grains of michenerite – primarily located in the Inner Vein and hosted by chalcopyrite – are not accompanied by other PMM. It is

more plausible that this michenerite crystallized directly from the residual sulfide melt, largely unaffected by the magmatic fluids associated with option 3.

Most PGM are concentrated in the larger volume of residual melt found in the Inner Vein, where they were likely mobilized by late-stage magmatic fluids and deposited proximal to Ni-rich minerals (Fig. 7.1.2D). These fluids also appear to have facilitated the replacement of pentlandite by violarite II and promoted the formation of composite grains associated with quartz-chlorite inclusions in the Inner Vein.

The crystallization sequence of these PGM grains can be roughly constrained using their textural relationships and maximum temperature of stability. Merenskyite, stable up to 740°C, likely formed first, followed by Te-rich kotulskite and michenerite; the bismuth content in these phases lowers their stability to <600°C (Hoffman and MacLean, 1976; Makovicky, 2002). The presence of kotulskite within the Inner Vein intergrown with hessite indicates limited bismuth availability to palladium, likely due to the abundance of Bi-rich tsumoite, with hedleyite cores, accessory Bi-tellurides and native bismuth hosted within altered pyrrhotite in the Inner Vein (Fig. 7.1.3). This abundance decreases towards the Outer Vein and matildite replaces hessite in the PGM composites in the immediate contact. This may reflect local variations in Pd, Bi, and Te availability, and potentially different cooling rates, residence times or fluid compositions. Native gold, limited to the immediate contact and associated with PGM and violarite II, may similarly reflect the variation in fluid compositions and gold availability.

Thus, the primary magmatic crystallization sequence involved: (1) ISS segregation and chalcopyrite crystallization, (2) residual melt migration and enrichment, (3) early magnetite crystallization, (4) early sperrylite crystallization, (5) unmixing of BMS and formation of pyrrhotite and violarite II, and (6) crystallization of Pd-Te-Bi PGM composites and exsolution of Ag-bearing minerals.

7.2 Late-stage fluid evolution and sulfide modification

Many studies have suggested post-formational hydrothermal overprinting and fluid input from the footwall played a role in modifying sulfide textures in the Sudbury offset dykes (Springer, 1989; Farrow et al., 1994; Hanley et al., 2005). However, such interpretations are often based on experimental work and observations from the more thoroughly studied South Range deposits (Farrow et al., 1994; Lightfoot and Farrow, 2002) and western North Range deposits (Springer, 1989; Farrow and Watkinson, 1996; Hanley et al., 2005). While the South Range experienced a complex post-magmatic metamorphic and deformation history (Bailey et al., 2006; Lightfoot, 2016), the same mineralization models cannot be broadly applied to the eastern North Range that remained relatively unmodified by deformation (Fleet et al., 1987; Easton, 2000; Szabó and Halls, 2006). At the Podolsky North Zone, multiple lines of evidence indicate that fluid-mediated

reactions within the sulfide vein were driven by an exsolved, late-magmatic fluid, rather than by a secondary hydrothermal overprint. The fluid responsible was likely Cl-rich, H_2O-poor and enriched in iron, playing a key role in modifying the original sulfide assemblage.

One of the clearest indicators of a magmatic fluid phase in the Inner Vein is the presence of complex daughter mineral assemblages within fluid inclusions. These include Cl-bearing ferropyrosmalite, hibbingite, halite, chlorargyrite and cotunnite, as well as base-metal minerals such as magnetite, pyrrhotite, sphalerite and cassiterite, many of which are Fe-rich. Using the classification system defined by Molnar et al. (2001) for fluid inclusions hosted by quartz in footwall granophyre within the PGM-bearing vein deposits, the inclusions found within our studied samples are comparable to the type I saturated aqueous inclusions and possibly type II unsaturated aqueous inclusions. While the compositions of daughter minerals found in this study differ slightly from the original publication, the textural relationships remain consistent. The mineralogical variety of daughter minerals the present study most closely resembles those identified by (Farrow et al., 1994) in chalcopyrite veins from the Barnet property.

The fluid inclusion assemblage of the studied samples points to the exsolution of a halide-rich, relatively anhydrous fluid phase from the crystallizing sulfide melt (Fig. 7.1.2 C,D; Mungall and Brenan, 2003). Hydrated daughter minerals, ferropyrosmalite and hibbingite incorporate both Cl and OH, indicative of a high-temperature, metal-rich fluid (Springer, 1989; Mungall and Brenan, 2003; Koděra et al., 2003; Koděra et al., 2022). The occurrence of ferropyrosmalite at temperatures of ~510-430°C (Dong and Pollard, 1997) constrains the timing of fluid activity to the late-magmatic stage – coinciding with the final crystallization of the residual melt and overlapping the temperature stability field of PGM formation.

Additional evidence for a late-magmatic fluid is provided by mineral replacement textures within the Inner Vein and their absence in the Outer Vein. Pyrrhotite replacement by marcasite (and pentlandite replacement by violarite II), described in Chapter 6 and illustrated in Figure 7.1.2D, mirror those described by Arnold and Malik (1974) from the Whistle property. The intensity of pyrrhotite-marcasite alteration increases toward the Inner Vein with complete replacement more often associated with fluid inclusion trails (Fig. 7.1.1).

Nelles (2012) attributed the formation of bornite-millerite veins at the Morrison deposit to Fe-loss of the sulfide melt where excess sulfur was removed as S-rich vapour (also containing iron and copper) by interaction with the wall rock and deep groundwaters. Their model also states that the thicker sulfide veins would be Fe-deficient at vein margins with the vein center preserving primary compositions due to buffering by the remaining sulfide melt. In contrast to this model, our samples suggest Fe-loss and S-enrichment of primary magmatic sulfides in the vein center (Inner Vein), observed as intense pyrrhotite to marcasite replacement, and preserve relative Fe-enrichment at the vein margin (Outer Vein), as unaltered pyrrhotite (Fig. 7.1.1). The contradicting

trends suggest an internally derived magmatic fluid source originating and escaping the vein instead of fluids penetrating the vein from wall rock interactions and groundwaters as proposed by Nelles (2012).

The pyrrhotite-marcasite textures imply interaction with a low temperature, somewhat acidic fluid (between 25º and 160ºC with pH ~5; Schoonen and Barnes, 1991). The conversion rate of pyrrhotite replacement above 100ºC depends on the fluid composition and pH. Marcasite forms more readily in fluids containing excess sulfur as thiosulfate- and polysulfide-rich species – without which the conversion is significantly slower (Schoonen and Barnes, 1991). Therefore, the spatial relationship of this replacement in our channel suggests sulfidation occurred rapidly in the Inner Vein with concurrent Fe-loss by elemental sulfur or by complexation to form marcasite, while the Outer Vein pyrrhotite remained largely unaffected by fluids, preserving its original chemistry.

Violarite II is ubiquitously distributed throughout the Inner Vein and may reflect the susceptibility of pentlandite to alteration (Michener and Yates, 1944). The regular spatial association of violarite II with quartz and chlorite within silicate inclusions also supports its origin as a product of fluid-related replacement. The contrasting textures and compositions of violarite I and II point to distinct fluid-sulfide interactions and pathways. Violarite I forms Ni-rich, crack-free grains intergrown with millerite within fractures and inclusions in the Inner Vein. The presence of violarite I+millerite in open fractures rather than along replacement fronts implies that it may represent a primary phase precipitated from a Fe-Ni-rich fluid (cf. Li and Naldrett, 1993), rather than a secondary alteration product. Depending on the timing of vein deformation, it is possible that these phases formed from the same late-magmatic fluids that produced marcasite in the Inner Vein.

Homogeneous and relatively heavy $\delta^{34}S$ values in chalcopyrite (Chapter 6.5) may or may not indicate that sulfur isotope fractionation has occurred. One straightforward explanation is that the sulfur assimilated from the country rocks into the SIC impact melt sheet was initially enriched in ^{34}S. However, this interpretation contrasts with the generally heavier $\delta^{34}S$ values observed in our study when compared to silicate samples from the Whistle mine analyzed by Ripley et al. (2015). Alternatively, ^{34}S enrichment may have resulted from the settling and differentiation of lighter ^{32}S-rich MSS or from isotopic fractionation of ^{32}S into a vapour or fluid phase during the crystallization of the ISS. In both scenarios, the residual Cu-rich melt would become relatively enriched in ^{34}S (Schwarcz, 1973). Chalcopyrite from the pre-Sudbury Event Grey Gabbro at the Podolsky 2000 deposit, studied by MacInnis et al. (2014), also exhibits heavy $\delta^{34}S$ values ranging from 3.4‰ to 4.5‰, which were interpreted as the product of a homogeneous crustal sulfur reservoir, likely sourced from the melt sheet. Slightly heavier $\delta^{34}S$ values in the Podolsky North Zone may reflect larger-scale (metre- to kilometre-scale) fractionation processes along the Whistle offset, with the most ^{34}S-enriched residual melt transported furthest from the SIC. A more

comprehensive isotopic study along the entire offset is required to fully resolve these interpretations.

Halogen-rich alteration haloes around Sudbury footwall-style deposits are commonly interpreted as products of residual magmatic fluid interaction with the host rock and have been proposed as potential pathfinder indicators for concealed sulfide mineralization (McCormick et al., 2002; Hanley and Mungall, 2003; Hanley et al., 2004). In our channel, the chloritic alteration halo of the Contact Zone and the gneissic metabreccia host rock show no petrographic or chemical evidence for heavy halogen enrichment – specifically the absence of Cl-bearing minerals such as amphibole (e.g., actinolite or hornblende), biotite, or Cl-apatite.

EPMA analyses of chlorite (chamosite) indicate compositions that vary from vein to gneiss, being slightly Fe- and Ni-enriched in the vein and becoming progressively Fe-Ni-depleted through the Contact Zone towards the gneiss. The enrichment is likely attributed to migrating magmatic fluids originating from within the vein mobilizing iron and nickel. The depletion outside the vein could be a consequence of a later event erasing any trace of magmatic fluid transport in the gneiss and outer Contact Zone. If iron and nickel can be used as proxies for fluid movement in lieu of more direct halogen analyses of these samples, then magmatic fluids only minimally penetrated the host rock and instead concentrated at the vein-host contact and formed Fe-rich chamosite. A subsequent fluid event could have diluted any halogen signature away from the sulfide vein (cf. Marshall et al., 1999; McCormick et al., 2002; Hanley et al., 2004) leaving the magmatic-formed Contact Zone and Outer Vein halogen-free. This overprint may also account for the observed darker green chlorite in the Contact Zone that brought in a more Ti-rich fluid, revealed by μXRF mapping of the contact, and may explain the abundance of Ca-Ti-rich phases observed within the gneiss's more Mg-rich chamosite.

The epidote-chlorite-quartz bands observed in the Outer Vein and Contact Zone are challenging to interpret. These selvages are confined to narrow, vertical bands in the Outer Vein and the constituent silicates are devoid of internal deformation features. Although earlier fluid inclusion studies documented $CaCl_2$ precipitates from fractured inclusions and interpreted them as indicators of footwall fluid influence (Li and Naldrett, 1993; Farrow et al., 1994), inclusions and daughter minerals analyzed in the present study are notably Ca-depleted. Aside from epidote, the only Ca-bearing phases we identified include sparse daughter anhydrite grains and liquid fluid inclusions with minor amounts of calcium in the Inner Vein, apatite in the Contact Zone and gneiss, and two Na-rich plagioclase grains and aggregates of Ca-Ti-rich phases within the gneiss. The low solubility of calcium in sulfide melt (due to its lithophile behaviour; Mungall and Brenan, 2003) and the absence of strongly calcic phases in the vein implies that late-magmatic fluids exsolved from the sulfide body were inherently Ca-poor and calcium was instead enriched by an external fluid source (Fig. 7.1.2D).

Epidote veining in the North Range is typically interpreted as the product of hydrothermal overprinting, with calcium obtained through leaching of the adjacent footwall rocks (Farrow and Watkinson, 1996; Molnar et al., 2001; Carter et al., 2009). While such a model may plausibly explain the trace epidote within the Levack gneiss and minor occurrences in the Contact Zone, it does not adequately account for the well-defined, epidote-rich bands in the massive sulfide vein (Fig. 6.1.2A). We therefore propose that the parallel epidote-bearing bands may reflect a late- to post-crystallization hydrothermal event in which a Ca-rich fluid exploited structural pathways (fractures) generated by earlier deformation, described in Chapter 7.1.

The alignment of the epidote bands parallel to the vein-silicate contact suggests structurally controlled low-energy fluid flow. The sharp outer margins of the bands imply a Ca-rich fluid encountered a dense, low-permeability chalcopyrite matrix. Towards the bands center, chlorite is more abundant and micaceous, and quartz fills the remaining pore space. It is likely that the Ca-rich fluid injected into the fracture became stagnant, allowing crystallization of the fluid to occur as a closed system.

This mineralogical assemblage is consistent with the infiltration of a single-stage, low-temperature, brine-derived, Ca-rich fluid originating from the Canadian Shield during a late- to post-crystallization (<1.7 Ga) hydrothermal event (Farrow and Watkinson, 1996; Molnar et al., 2001; Hanley et al., 2011). The event, described by Molnar et al. (2001), is commonly linked to the northwestern region of the SIC, however these fluids also exploited the North Range's footwall contact, migrating along the northeastern fractures of earlier formed Cu-Ni-PGE veins. The Podolsky North Zone is a footwall deposit located northeast of the SIC with tensional structures associated with the massive sulfides (Chapter 4.3) suggesting fluids were perhaps capable of penetrating the vein with relatively low energy. This could have allowed for the fluid to pool in existing fractures and initiate crystallization.

The crystallization sequence began with epidote, followed by chlorite as a result of Ca-depletion, then quartz from the excess silica. Some areas within the bands show texturally distinct zones of chlorite with quartz, potentially representing recrystallized primary magmatic silicate inclusions, resembling those observed in TS 2. The sourced fluids were particularly elevated in calcium and strontium (Hanley and Mungall, 2003; Hanley et al., 2011). EPMA analysis of the Podolsky North Zone epidote revealed no significant chemical variation across the bands or Contact Zone. Strontium was not analyzed with EPMA but μXRF element mapping indicate that the epidote bands of the Contact Zone are enriched in strontium (Appendix A9), implying the bands within the vein are likely Sr-enriched too. This signifies that the epidote-forming fluids were compositionally distinct from the Na-Fe-rich magmatic fluids and could have locally overprinted earlier magmatic textures. The fluids were also capable of mobilizing precious ore metals (Hanley et al., 2011), potentially accounting for the PGM-poor hessite-tsumoite composite grains within

the epidote bands. The influence of volatiles on precious metal transport are discussed in detail in the next section.

7.3 Linking evidence for volatile activity to precious metal mineralization

Platinum group elements (PGE) and halogens are generally incompatible during the crystallization of MSS and ISS and thus become progressively concentrated in the residual sulfide liquid as fractionation proceeds (Mungall and Brenan, 2003). Although the solubility of the PGE in aqueous fluids is typically low, numerous studies have demonstrated that their mobility can be significantly enhanced in the presence of the halogens, especially chlorine, and form stable complexes with metals such as platinum and palladium under magmatic conditions (Wood, 2002; Mungall and Brenan, 2003; Hanley, 2006; Sullivan et al., 2022). The enrichment of the PGE in the Inner Vein of the Podolsky North Zone is interpreted as the result of a highly saline magmatic fluid phase exsolved from the most PGE- and volatile-rich portion of the residual sulfide liquid.

Fluid inclusions hosted in chalcopyrite from the Inner sulfide Vein include cavities containing halite daughter minerals, and Cl-phases such as cotunnite ($PbCl_2$) and chlorargyrite (AgCl). While cotunnite has been commonly documented in Sudbury inclusions, chlorargyrite has only been reported but not discussed in the Barnet property and the Strathcona Deep Copper Zone (Farrow, 1994), and not previously from offset dyke sulfides. If the silver in chlorargyrite was magmatic in origin and not due to hydrothermal remobilization, this could provide direct evidence of precious metal transport by chloride complexation. Trace palladium contents observed in a few halite grains may also directly represent PGE species transported in the exsolved chloride-rich melt, though more grains would need to be analyzed to confirm this.

The higher volatile content of the Inner Vein correlates with more abundant and compositionally complex PGM occurrences. In this zone, sperrylite and Bi-tellurides are common, and large violarite II grains are closely associated with rounded Bi-rich Pd-PGM and quartz-chlorite inclusions. The absence of textural modifications or satellite PGM grains suggests that these composites crystallized directly from the fluid rather than representing relict PGM left behind following sulfide dissolution by a later fluid phase (cf. Hanley, 2006; Dare et al., 2014). Additionally, trails of decrepitated fluid inclusions oriented inward and upward toward the center and upper portions of the vein (Fig. 7.1.1) provide further evidence for the exsolution and short distance (≤0.5 mm) migration of a pressurized volatile phase. In the Outer Vein, PGM are more rare, primarily as small sperrylite grains enclosed within chalcopyrite, Bi-Te phases are absent in unaltered pyrrhotite, and violarite II grains are small and not associated with PGM except close to the vein contact. The distribution pattern and the preservation of PGM textures of our samples support a model in which halogens and associated metals migrated inward via a metal-bearing magmatic fluid, concentrating PGE from the Outer to Inner Vein.

Experimental and thermodynamic studies indicate that platinum and palladium can efficiently form chloride complexes in magmatic systems between 25 and 300°C, particularly under mildly to highly acidic and strongly oxidizing conditions (Gammons et al., 1992; Wood, 2002; Sullivan et al., 2022). This presents a paradox, as the presence of chalcopyrite, pyrrhotite, and marcasite in Sudbury footwall deposits in general, typically indicate near-neutral pH and reducing conditions (Wood, 2002; Sullivan et al., 2022). Farrow and Watkinson (1996) proposed that log fO_2 as high as -27 and pH values between 3 and 8 could be attained through the progressive evolution of sulfide melts, while Wood (2002) argued that to achieve even 1 ng/kg of Pt or Pd in solution at pH >3, fluid conditions would need to be sufficiently oxidizing to stabilize in the magnetite-hematite field.

Hibbingite [$Fe^{2+}_2(OH)_3Cl$], a relatively abundant daughter mineral within the decrepitated Inner Vein inclusions, forms from moderately reducing and mildly acidic brines (Nemer et al., 2011). This phase may act as the oxygen buffer needed to increase the solubility and efficiently transport significant quantities of platinum and palladium as chloride complexes in fluids at temperatures above 300ºC in less acidic (pH >3) and reduced conditions (Wood, 2002; Gammons and Allin, 2022). In this context, Cl-rich fluids exsolved during late-stage sulfide crystallization in the North Zone were capable of mobilizing the PGE toward the vein interior, where longer residence times and slower cooling promoted complex mineral growth and composite PGM assemblages.

Although Pd-PGM are not observed in direct association with Cl-bearing daughter minerals, they are frequently hosted along the boundaries of violarite II. This suggests that palladium transport may have occurred via other volatile complexes, such as bisulfide ligands, rather than chloride complexes. Bisulfide transport of PGE has been proposed in several Sudbury studies (Schoonen and Barnes, 1991; Gammons et al., 1992; Wood, 2002; Hanley, 2006; Sullivan et al., 2022), particularly in settings lacking the low-pH, high-fO_2 conditions required for chloride complexation below 300°C. However, the identification of hibbingite and the Cl-poor oxide daughter minerals magnetite and trace hematite in our vein may reflect a more oxidizing fluid regime in the North Zone. This suggests that chloride complexation of precious metals cannot be entirely ruled out, particularly during the higher-temperature stages of fluid evolution.

Hanley (2006) noted, based on that of Wood (2002) experiments, that platinum and palladium are effectively insoluble in chloride-rich fluids under the reduced and near-neutral pH conditions common in Sudbury. Furthermore, the presence of chalcophile ligands such as S, Fe, Te, Se, As, Sn, Cu, Bi, and Ag in natural systems can limit PGE solubility in hydrothermal fluids (Dare et al., 2014), thus implying a predominantly magmatic origin for PGE transport in halogen-rich systems (Mungall and Brenan, 2003). Recent studies show that dry (H_2O-poor) chloride-rich brines can efficiently extract Pd, Pt, and other chalcophile elements from immiscible sulfide liquids

or residual melt fractions, transporting them short distances before saturation and precipitation occurs (Mungall and Brenan, 2003; Sullivan et al., 2022).

Deformation in the Outer Vein caused by slowing internal lateral flow, provided pathways for later hydrothermal fluids. The timing and extent of deformation and its impact on magmatic PGE signatures in the Outer Vein are difficult to constrain. No PGM were observed within the epidote bands. This does not mean that no magmatic fluids were present and had formed the same Pd-PGM-hosting chlorite-quartz inclusions as the Inner Vein, only that they may have been overprinted by the hydrothermal event that was capable of remobilizing the PGM. If the Bi-tellurides associated with pyrrhotite in the Inner Vein had originally been present in the Outer Vein too, they may have been removed by this fluid as they are most susceptible to dissolution or remobilization (Dare et al., 2014), which may explain the Bi-enrichment of PGM in the immediate contact. The few intergrowths of hessite and tsumoite located in the epidote bands were likely stabilized due to the higher Te-content from hessite.

The Outer Vein also lacks fluid inclusion trails; instead, only densely packed vapour-only inclusions are present near the Contact Zone and between bands. This may indicate the formation of a low-permeability barrier during late-stage sulfide crystallization or early volatile loss, which restricted volatile migration and concentrated metal-laden aqueous fluids in the center of the vein with the residual sulfide melt. Such a barrier would be more susceptible to deformation, possibly aiding the volatile loss, and could explain the pronounced concentration of Pd-PGM, Cl-bearing phases, and larger fluid inclusions in the Inner Vein compared to the Outer Vein. While the precise processes affecting the Outer Vein remain uncertain, it is clear that the Inner Vein better preserves primary magmatic PGE signatures, whereas those in the exterior have been either overprinted or erased.

These observations support a model in which the transition from a sulfide-saturated melt to a volatile-depleted solid was mediated by the exsolution of a chloride-bearing magmatic fluid. This fluid facilitated at minimum short-range PGE mobilization and local enrichment, ultimately contributing to the high metal tenor and complex PGM mineralogy observed in the inner portions of the sulfide vein.

8. Conclusion

Footwall-style Cu-PGE sulfide deposits in the Sudbury Structure have become increasingly important for economic development and precious metal exploration. New insights presented in this study of the Podolsky North Zone, located within the Whistle Offset dyke, broaden our understanding of volatile mobility and volatile-metal interactions in magmatic sulfide systems. By integrating petrographic, mineral chemical, and sulfur isotopic data from a chalcopyrite-rich sulfide vein, chloritic alteration halo, and associated host lithologies, this study explores Podolsky North's sulfide differentiation, volatile mobilization, and precious metal enrichment.

Petrographic and mineral chemistry observations reveal that sulfide differentiation follows a complex, yet traceable crystallization sequence dominated by ISS, followed by localized enrichment of PGE within a late-stage, chalcopyrite-dominated residual sulfide melt in the interior of the vein. Notably, platinum-group minerals – particularly those bearing Pd, Bi, and Te – are intimately associated with violarite, chlorite, and quartz in microstructures within and along the margins of the sulfide veins. Sulfur isotopic signatures further support a model involving late-stage, oxidizing fluids interacting with the crystallizing sulfide system. Epidote-bearing bands within the vein and the chlorite-dominated Contact Zone exhibit evidence for ductile deformation and fluid overprinting, suggesting that multiple fluid events have occurred.

These findings highlight the dynamic interplay between sulfide melt crystallization and volatile exsolution in the formation of high-tenor ore zones in the Sudbury footwall environment. Halogens, especially chlorine, appear to enhance metal solubility and transport, either through complexation in magmatic fluids or via late-stage hydrothermal processes. The presence of well-developed directional fluid inclusion trails and precious metal-bearing daughter minerals within the interior of the vein supports the hypothesis that volatile-rich fluids actively participated in PGE enrichment and redistribution during vein crystallization.

By investigating the Podolsky North Zone, this thesis expands current genetic models for offset dyke mineralization in the SIC, demonstrating that even distal footwall-style mineralization preserves a complex history of magmatic differentiation, fluid interaction, and metal enrichment.

Future Work

Looking forward, future research should focus on the systematic quantification of halogen abundances across sulfide veins, alteration haloes, and silicate hosts to compliment petrographic observations. Innovative techniques such as Neutron-Irradiation Noble Gas Mass Spectrometry (NI-NGMS) offer the potential to precisely measure heavy halogen abundances in small sample masses (cf. Ruzié-Hamilton et al., 2016). Samples from this study have been prepared for NI-NGMS and are currently awaiting analysis for a future paper. These analyses will focus on the fractionation of halogens – particularly Cl, Br, and I – as a consequence of sulfide melt

differentiation. Because halogens exhibit different compatibilities in silicate and sulfide phases, their distribution can provide insights into the evolution of magmatic-hydrothermal systems. Understanding how halogens partition between melt, fluid, and sulfide phases during segregation and crystallization may help trace the processes leading to metal enrichment in offset dykes. The application of halogen geochemistry in this way may serve as a valuable "pathfinder" tool for massive sulfide mineral exploration and further refine exploration models in magmatic ore systems worldwide.

References

Ames, D.E., and Farrow, C.E.G. (2007). Metallogeny of the Sudbury mining camp, Ontario. *In* W.D. Goodfellow (Ed.), *Mineral Deposits of Canada: A synthesis of major deposit types, district metallogeny, the evolution of geological provinces, and exploration methods* (p. 329-350). Geological Association of Canada, Special Publication Volume 5.

Ames, D.E., Golightly, J.P., Lightfoot, P.C., and Gibson, H.L. (2002). Vitric compositions in the Onaping Formation and their relationship to the Sudbury igneous complex, Sudbury Structure. *Economic Geology*, **97**(7), 1541-1562.

Ariskin, A.A., Deutsch, A., Ostermann, M. (1999). Sudbury Igneous Complex: Simulating phase equilibria and in situ differentiation for two proposed parental magmas. *In* B.O. Dressler, and V.L. Sharpton (Eds.), *Large Meteorite Impacts and Planetary Evolution II.* Geological Society of America Special Paper 339.

Arnold, R.G., and Malik, O.P. (1974). Violarite in some nickel ores from Lynn Lake and Thompson, Manitoba, and Sudbury, Ontario, Canada. *Canadian Mineralogist*, **12**, 320-326.

Bai, L., Barnes, S.-J., and Baker, D.R. (2017). Sperrylite saturation in magmatic sulfide melts: Implications for formation of PGE-bearing arsenides and sulfarsenides. *American Mineralogist*, **102**(5), 966-974.

Bailey, J., McDonald, A.M., Lafrance, B., and Fedorowich, J.S. (2006). Variations in Ni content in sheared magmatic sulfide ore at the Thayer Lindsley mine, Sudbury, Ontario. *The Canadian Mineralogist*, **44**(5), 1063-1077.

Ballhaus, C.G., and Stumpfl, E.F. (1986). Sulfide and platinum mineralization in the Merensky Reef: Evidence from hydrous silicates and fluid inclusions. *Contributions to Mineralogy and Petrology*, **94**, 193-204.

Ballhaus, C.G., Tredoux, M., and Spath, A. (2001). Phase Relations in the Fe-Ni-Cu-PGE-S System at Magmatic Temperature and Application to Massive Sulphide Ores of the Sudbury Igneous Complex. *Journal of Petrology*, **42**(10), 1911-1926.

Barnes, S.-J., Taranovic, V., Schoneveld, L.E., Mansur, E.T., Le Vaillant, M., Dare, S.A.S, Staude, S., Evans, N.J., and Blanks, D. (2020). The occurrence and origin of pentlandite-chalcopyrite-pyrrhotite loop textures in magmatic Ni-Cu sulfide ores. *Economic Geology*, **115**(8), 1777-1798.

Barnes, S.-J., Makovicky, E., Makovicky, M., Rose-Hansen, J., and Karup-Moller, S. (1997). Partition coefficients for Ni, Cu, Pd, Pt, Rh, and Ir between monosulfide solid solution and sulfide liquid and the formation of compositionally zoned Ni-Cu sulfide bodies by fractional crystallization of sulfide liquid. *Canadian Journal of Earth Sciences*, **34**(4), 366-374.

Boast, M., and Spray, J.G. (2006). Superimposition of a thrust-transfer fault system on a large impact structure: implications for Ni-Cu-PGE exploration at Sudbury. *Economic Geology*, **101**, 1583-1594.

Boerner, D.E., Milkereit, B. (1999). Structural evolution of the Sudbury impact structure in the light of seismic reflection data. *In* B.O. Dressler, and V.L. Sharpton (Eds.), *Large Meteorite Impacts and Planetary Evolution II*. Geological Society of America Special Paper 339.

Boudreau, A.E. (2016). The Stillwater Complex, Montana – Overview and the significance of volatiles. *Mineralogical Magazine*, **80**(4), 585-637.

Card, K. D. (1994). Geology of the Levack Gneiss Complex, the northern footwall of the Sudbury Structure, Ontario. In *Canadian Shield, Geological Survey of Canada, Current Research, 1994-C*, 269-278. Natural Resources Canada.

Card, K.D., Gupta, V.K., McGrath, P.H., and Grant, F.S. (1984). The Sudbury Structure: Its regional geological and geophysical setting. *In* E. Pye, A.J. Naldrett, and P.E. Giblin (Eds.), *The Geology and Ore Deposits of the Sudbury Structure* (p. 25-44). Ontario Geological Survey Special Volume 1.

Carter, W.M. (2005). *Field Relationships, Petrology, Geochemistry, and Petrogenesis of Quartz Dioritic Magmas, Whistle Offset, Sudbury Structure, Canada* [MSc Thesis]. Carleton University.

Carter, W.M., Watkinson, D.H., Ames, D.E., and Jones, P.C. (2009). Quartz dioritic magmas and Cu-(Ni)-PGE mineralization, Podolsky Deposit, Whistle Offset Structure, Sudbury, Ontario. *Geological Survey of Canada, Open File 6134*. Natural Resources Canada.

Chyi, L.L., and Crocket, J.H. (1976). Partition of Platinum, Palladium, Iridium, and Gold among Coexisting Minerals from the Deep Ore Zone, Strathcona Mine, Sudbury, Ontario. *Economic Geology*, **71**, 1196-1205.

Corfu, F., and Andrews, A.J. (1986). A U-Pb age for mineralized Nipissing diabase, Gowganda, Ontario. *Canadian Journal of Earth Sciences*, **23**(1), 107-109.

Dare, S.A.S., Barnes, S.-J., and Prichard, H.M. (2010). The distribution of platinum group elements (PGE) and other chalcophile elements among sulfides from the Creighton Ni-Cu-PGE sulfide deposit, Sudbury, Canada, and the origin of palladium in pentlandite. *Mineralium Deposita*, **45**(8), 765-793.

Dare, S.A.S., Barnes, S.-J., Prichard, H.M., and Fisher, P.C. (2011). Chalcophile and platinum-group element (PGE) concentrations in the sulfide minerals from the McCreedy East deposit, Sudbury, Canada, and the origin of PGE in pyrite. *Mineralium Deposita*, **46**(4), 381-407.

Dare, S.A.S., Barnes, S.-J., Prichard, H.M., and Fisher, P.C. (2014). Mineralogy and Geochemistry of Cu-rich Ores from the McCreedy East Ni-Cu-PGE Deposit (Sudbury, Canada): Implications for the Behavior of Platinum Group and Chalcophile Elements at the End of Crystallization of a Sulfide Liquid. *Economic Geology*, **109**(2), 343-366.

Deutsch, A., Grieve, R.A.F., Avermann, M., Bischoff, L., Brockmeyer, P., Buhl, D., Lakomy, R., Muller-Mohr, V., Ostermann, M., and Stoffler, D. (1995). The Sudbury Structure (Ontario, Canada): a tectonically deformed multi-ring impact basin. *Geologische Rundschau*, **84**, 697-709.

Dong, G., and Pollard, P.J. (1997). Identification of ferropyrosmalite by Laser Raman microprobe in fluid inclusions from metalliferous deposits in the Cloncurry District, NW Queensland, Australia. *Mineralogical Magazine*, **61**, 291-293.

Dressler, B.O. (1984). The effects of the Sudbury event and the intrusion of the Sudbury Igneous Complex on the footwall rocks of the Sudbury Structure. *In* E.G. Pye, A.J. Naldrett, and P.E. Giblin (Eds.), *The Geology and Ore Deposits of the Sudbury Structure* (p. 97-136). Ontario Geological Survey Special Volume 1.

Duran, C.J., Barnes, S.-J., Pleše, P., Kudrna Prašek, M., Zientek, M.L., and Pagé, P. (2017). Fractional crystallization-induced variations in sulfides from the Noril'sk-Talnakh mining district (polar Siberia, Russia). *Ore Geology Reviews*, **90**, 326-351.

Dutrizac, J.E. (1976). Reactions in Cubanite and Chalcopyrite. *Canadian Mineralogist*, **14**, 172-181.

Easton, M.R. (2000). Metamorphism of the Canadian Shield, Ontario, Canada. II Proterozoic Metamorphic History. *The Canadian Mineralogist*, **38**, 319-344.

Farrow, C.E.G. (1994). *Geology, alteration, and the role of fluids in Cu-Ni-PGE mineralization of the footwall rocks to the Sudbury Igneous Complex, Levack and Morgan Townships, Sudbury District, Ontario* [PhD Thesis]. Carleton University.

Farrow, C.E.G., Everest, J.O., King, D.M., and Jolette, C. (2005). Sudbury Cu(-Ni)-PGE systems: Refining the classification using McCreedy West mine and Podolsky project case studies. In J.E. Mungall (Ed.), *Exploration for Platinum-Group Element Deposits* (p. 163-180). Mineralogical Association of Canada Short Course.

Farrow, C.E.G., and Lightfoot, P.C. (2002). Sudbury PGE Revisited: Toward an Integrated Model. *In* L.J. Cabri (Ed.), *The Geology, Geochemistry, Mineralogy and Mineral Beneficiation of Platinum-Group Elements* (p. 273-297). Canadian Institute of Mining, Metallurgy and Petroleum Special Volume 54.

Farrow, C.E.G., and Watkinson, D.H. (1992). Alteration and the role of fluids in Ni, Cu and platinum-group element deposition, Sudbury Igneous Complex contact, Onaping-Levack area, Ontario. *Mineralogy and Petrology*, **46**, 67-83.

Farrow, C.E.G., and Watkinson, D.H. (1996). Geochemical Evolution of the Epidote Zone, Fraser Mine, Sudbury, Ontario: Ni-Cu-PGE Remobilization by Saline Fluids. *Exploration and Mining Geology*, **5**(1), 17-31.

Farrow, C.E.G., Watkinson, D.H., and Jones, P.C. (1994). Fluid inclusions in sulfides from North and South Range Cu-Ni-PGE deposits, Sudbury Structure, Ontario. *Economic Geology*, **89**, 647-655.

Fleet, M.E., Barnett, R.L., and Morris, W.A. (1987). Prograde Metamorphism of the Sudbury Igneous Complex. *Canadian Mineralogist*, **25**, 499-514.

Fleet, M.E., and Wu, T.-W. (1993). Volatile transport of platinum-group elements in sulfide-chloride assemblages at 1000°C. *Geochimica et Cosmochimica Acta*, **57**(15), 3519-3531.

Gammons, C.H., and Allin, N.C. (2022). Stability of aqueous Fe(III) chloride complexes and the solubility of hematite between 150 and 300 °C. *Geochimica et Cosmochimica Acta*, **330**, 148-164.

Gammons, C.H., Bloom, M.S., and Yu, Y. (1992). Experimental investigation of the hydrothermal geochemistry of platinum and palladium: I. Solubility of platinum and palladium sulfide minerals in $NaCl/H_2SO_4$ solutions at 300°C. *Geochimica et Cosmochimica Acta*, **56**, 3881-3894.

Golightly, J.P. (1994). The Sudbury Igneous Complex as an impact melt: Evolution and ore genesis. *In* P.C. Lightfoot and A.J. Naldrett (Eds*.), Proceedings of the Sudbury - Noril'sk Symposium* (p. 105-117). Ontario Geological Survey Special Volume 5.

Grieve, R.A.F. (1994). An Impact Model of the Sudbury Structure. *In* P.C. Lightfoot and A.J. Naldrett (Eds.), *Proceedings of the Sudbury - Noril'sk Symposium* (p. 119-132). Ontario Geological Survey Special Volume 5.

Grieve, R.A.F., Stoffler, D., and Deutsch, A. (1991). The Sudbury Structure: controversial or misunderstood? *Journal of Geophysical Research*, **96**, 22753-22764.

Hanley, J.J. (2006). *Experimental and Fluid Inclusion Constraints on the Ore Metal Content and Origin of Volatiles Associated with Large Ni-Cu-PGE Deposits* [PhD Thesis]. University of Toronto.

Hanley, J.J., Ames, D.E., Barnes, J., Sharp, Z., and Guillong, M. (2011). Interaction of magmatic fluids and silicate melt residues with saline groundwater in the footwall of the Sudbury Igneous Complex, Ontario, Canada: New evidence from bulk rock geochemistry, fluid inclusions and stable isotopes. *Chemical Geology*, **281**(1-2), 1-25.

Hanley, J.J., and Mungall, J.E. (2003). Chlorine Enrichment and Hydrous Alteration of the Sudbury Breccia Hosting Footwall Cu-Ni-PGE Mineralization at the Fraser Mine, Sudbury, Ontario, Canada. *Canadian Mineralogist*, **41**(4), 857-881.

Hanley, J.J., Mungall, J.E., Bray, C.J., and Gorton, M.P. (2004). The Origin of Bulk and Water-Soluble Cl and Br Enrichments in Ore-hosting Sudbury Breccia in the Fraser Copper Zone, Strathcona Embayment, Sudbury, Ontario, Canada. *The Canadian Mineralogist*, **42**, 1777-1798.

Hanley, J.J., Mungall, J.E., Pettke, T., Spooner, E.T.C., and Bray, C.J. (2005). Ore metal redistribution by hydrocarbon-brine and hydrocarbon-halide melt phases, North Range footwall of the Sudbury Igneous Complex, Ontario, Canada. *Mineralium Deposita*, **40**(3), 237-256.

Hanley, J.J., Mungall, J.E., Pettke, T., Spooner, E.T.C., and Bray, C.J. (2008). Fluid and halide melt Inclusions of magmatic origin in the ultramafic and lower banded series, Stillwater complex, Montana, USA. *Journal of Petrology*, **49**(6), 1133-1160.

Hawley, J.E. (1965). Upside-Down Zoning at Frood, Sudbury, Ontario. *Economic Geology*, **60**, 529-575.

Hoffman, E., and MacLean, W.H. (1976). Phase Relations of Michenerite and Merenskyite in the Pd-Bi-Te System. *Economic Geology*, **71**, 1461-1468.

Jorgensen, T.R.C., Tinkham, D.K., and Lesher, C.M. (2018) Low-*P* and high-*T* metamorphism of basalts: Insights from the Sudbury impact melt sheet aureole and thermodynamic modelling. *Journal of Metamorphic Geology*, **37**, 271-313.

Kanitpanyacharoen, W., and Boudreau, A.E. (2013). Sulfide-associated mineral assemblages in the Bushveld Complex, South Africa: Platinum-group element enrichment by vapor refining by chloride-carbonate fluids. *Mineralium Deposita*, **48**(2), 193-210.

Keays, R.R. (1995). The role of komatiitic and picritic magmatism and S-saturation in the formation of ore deposits. *Lithos*, **34**(1), 1-18.

Keays, R.R., and Crocket, J.H. (1970). A Study of Precious Metals in the Sudbury Nickel Irruptive Ores. *Economic Geology*, **65**, 438-450.

Keays, R.R., and Lightfoot, P.C. (2004). Formation of Ni-Cu-Platinum Group Element sulfide mineralization in the Sudbury Impact Melt Sheet. *Mineralogy and Petrology*, **82**, 217-258.

Koděra, P., Majzlan, J., Pollok, K., Kiefer, S., Šimko, F., Scholtzová, E., Luptáková, J., and Cawthorn, G. (2022). Ferrous hydroxychlorides hibbingite [γ-$Fe_2(OH)_3Cl$] and parahibbingite [β-$Fe_2(OH)_3Cl$] as a concealed sink of Cl and H_2O in ultrabasic and granitic systems. *American Mineralogist*, **107**(5), 826-841.

Koděra, P., Murphy, P.J., and Rankin, A.H. (2003). Retrograde mineral reactions in saline fluid inclusions: The transformation ferropyrosmalite ↔ clinopyroxene. *American Mineralogist*, **88**(1), 151-158.

Kojima, S., and Sugaki, A. (1984). Phase relations in the central portion of the Cu-Fe-Zn-S system between 800º and 500ºC. *Mineralogical Journal*, **12**, 15-28.

Krogh, T.E., Davis, D.W., and Corfu, F. (1984). Precise U-Pb Zircon and Baddeleyite Ages for the Sudbury Area. *In* E.G. Pye, A.J. Naldrett, and P.E. Giblin (Eds.), *The Geology and Ore Deposits of the Sudbury Structure* (p. 431-446). Ontario Geological Survey Special Volume 1.

Krogh, T.E., Kamo, S.L., and Bohor, B.F. (1996). Shock metamorphosed zircons with correlated U-Pb discordance and melt rocks with concordant protolith ages indicate an impact origin for the Sudbury structure. *In* A. Basu and S. Hart (Eds.), *Earth Processes: Reading the Isotopic Code* (p. 343-353). Volume 95.

Lafrance, B., Bygnes, L., and McDonald, A.M. (2014). Emplacement of metabreccia along the Whistle offset dike, Sudbury: Implications for post-impact modification of the Sudbury impact structure. *Canadian Journal of Earth Sciences*, **51**(5), 466-484.

Lafrance, B., Legault, D., and Ames, D.E. (2008). The formation of the Sudbury breccia in the North Range of the Sudbury impact structure. *Precambrian Research*, **165**(3-4), 107-119.

Lesher, C.M. (2017). Roles of xenomelts, xenoliths, xenocrysts, xenovolatiles, residues, and skarns in the genesis, transport, and localization of magmatic Fe-Ni-Cu-PGE sulfides and chromite. *Ore Geology Reviews*, **90**, 465-484.

Li, C., and Naldrett, A.J. (1993). Platinum-group minerals from the Deep Copper Zone of the Strathcona Deposit, Sudbury, Ontario. *Canadian Mineralogist*, **31**, 31-44.

Li, C., Naldrett, A.J., Coats, C.J.A., and Johannessen, P. (1992) Platinum, Palladium, Gold, and Copper-Rich Stringers at the Strathcona Mine, Sudbury: Their Enrichment by Fractionation of a Sulfide Liquid. *Economic Geology*, **87**, 1584-1598.

Li, C., and Ripley, E.M. (2005). Empirical equations to predict the sulfur content of mafic magmas at sulfide saturation and applications to magmatic sulfide deposits. *Mineralium Deposita*, **40**, 218-230.

Lightfoot, P.C. (2016). *Nickel Sulfide Ores and Impact Melts: Origin of the Sudbury Igneous Complex*. Elsevier.

Lightfoot, P.C., and Farrow, C.E.G. (2002). Geology, Geochemistry, and Mineralogy of the Worthington Offset Dike: A Genetic Model for Offset Dike Mineralization in the Sudbury Igneous Complex. *Economic Geology*, **97**, 1419-1446.

Lightfoot, P.C., Keays, R.R., and Doherty, W. (2001). Chemical Evolution and Origin of Nickel Sulfide Mineralization in the Sudbury Igneous Complex, Ontario, Canada. *Economic Geology*, **96**, 1855-1875.

Lightfoot, P.C., Keays, R.R., Morrison, G.G., Bite, A., and Farrell, K.P. (1997a). Geochemical Relationships in the Sudbury Igneous Complex: Origin of the Main Mass and Offset Dikes. *Economic Geology*, **92**, 289-307.

Lightfoot, P.C., Keays, R.R., Morrison, G.G., Bite, A., and Farrell, K.P. (1997b). Geologic and Geochemical Relationships between the Contact Sublayer, Inclusions, and the Main Mass of the Sudbury Igneous Complex: A Case Study of the Whistle Mine Embayment. *Economic Geology*, **92**(6), 647-673.

Lightfoot, P.C., and Zotov, I.A. (2005). Geology and Geochemistry of the Sudbury Igneous Complex, Ontario, Canada: Origin of Nickel Sulfide Mineralization Associated with an Impact-Generated Melt Sheet. *Geology of Ore Deposits*, **47**(5), 349-381.

MacInnis, L. (2019). *Constraining Alteration in the Footwall of the Sudbury Igneous Complex: A Case Study of the Alteration Footprint to the Podolsky, Cu(-Ni)-PGE Deposit, Sudbury* [MSc Thesis]. Laurentian University.

MacInnis, L.M., Kontak, D.J., Ames, D.E., and Joyce, N.L. (2014). *Alteration proximal to the sharp-walled Cu-(Ni)-PGE vein footwall mineralization of the Podolsky deposit, Sudbury Ontario*. Geological Survey of Canada Open File 7666.

Makovicky, E. (2002). Ternary and Quaternary Phase Systems with PGE. *In* L.J. Cabri (Ed.), *The Geology, Geochemistry, Mineralogy and Mineral Beneficiation of Platinum-Group Elements* (p. 131-175). Canadian Institute of Mining, Metallurgy and Petroleum Special Volume 54.

Mansur, E.T., Barnes, S.-J., and Duran, C.J. (2021). An overview of chalcophile element contents of pyrrhotite, pentlandite, chalcopyrite, and pyrite from magmatic Ni-Cu-PGE sulfide deposits. *Mineralium Deposita*, **56**(1), 179-204.

Marshall, D., Watkinson, D., Farrow, C., Molnar, F., and Fouillac, A.-M. (1999). Multiple fluid generations in the Sudbury igneous complex: fluid inclusion, Ar, O, H, Rb and Sr evidence. *Chemical Geology*, **154**, 1-19.

McCormick, K.A., Lesher, C.M., McDonald, A.M., Fedorowich, J.S., and James, R.S. (2002). Chlorine and Alkali Geochemical Halos in the Footwall Breccia and Sublayer Norite at the Margin of the Strathcona Embayment, Sudbury Structure, Ontario. *Economic Geology*, **97**, 1509-1519.

Meldrum, A., Abdel-Rahman, A.-F.M., Martin, R.F., and Wodicka, N. (1997). The nature, age and petrogenesis of the Cartier Batholith, northern flank of the Sudbury Structure, Ontario, Canada. *Precambrian Research*, **82**(3-4), 265-285.

Michener, C.E., and Yates, A.B. (1944). Oxidation of primary nickel sulphides. *Economic Geology,* **39**, 506-514.

Molnar, F., Watkinson, D.H., and Jones, P.C. (2001). Multiple Hydrothermal Processes in Footwall Units of the North Range, Sudbury Igneous Complex, Canada, and Implications for the Genesis of Vein-Type Cu-Ni-PGE Deposits. *Economic Geology*, **96**(7), 1645-1670.

Mukwakwami, J., Lafrance, B., Lesher, C.M. (2012). Back-thrusting and overturning of the southern margin of the 1.85 Ga Sudbury Igneous Complex at the Garson mine, Sudbury, Ontario. *Precambrian Research*, **196-197**, 81-105.

Mungall, J.E., Andrews, D.R.A., Cabri, L.J., Sylvester, P.J., and Tubrett, M. (2005). Partitioning of Cu, Ni, Au, and platinum-group elements between monosulfide solid solution and sulfide melt under controlled oxygen and sulfur fugacities. *Geochimica et Cosmochimica Acta*, **69**(17), 4349-4360.

Mungall, J.E., and Brenan, J.M. (2003). Experimental evidence for the chalcophile behavior of the halogens. *The Canadian Mineralogist*, **41**, 207-220.

Murphy, A.J., and Spray, J.G. (2002). Geology, Mineralization, and Emplacement of the Whistle-Parkin Offset Dike, Sudbury. *Economic Geology*, **97**, 1399-1418.

Naldrett, A.J. (1969). A Portion of the System Fe-S-0 between 900 and 1080 °C and its Application to Sulfide Ore Magmas. *Journal of Petrology*, **10**, 171-201.

Naldrett, A.J. (2004). *Magmatic Sulfide Deposits: Geology, Geochemistry and Exploration* (1st ed.). Springer.

Naldrett, A.J., Ebel, D.S., Asif, M., Morrison, G., and Moore, C.M. (1997). Fractional crystallization of sulfide melts as illustrated at Noril'sk and Sudbury. *European Journal of Mineralogy*, **9**, 365-377.

Naldrett, A.J., and Hewins, R.H. (1984). The Main Mass of the Sudbury Igneous Complex. *In* E. Pye, A.J. Naldrett, and P.E. Giblin (Eds.), *The Geology and Ore Deposits of the Sudbury Structure* (p. 235-251). Ontario Geological Survey Special Volume 1.

Nelles, E.W. (2012). *Genesis of Cu-PGE-rich Footwall-Type Mineralization in the Morrison Deposit, Sudbury* [MSc Thesis]. Laurentian University.

Nemer, M.B., Xiong, Y., Ismail, A.E., and Jang, J.H. (2011). Solubility of $Fe_2(OH)_3Cl$ (pure-iron endmember of hibbingite) in NaCl and Na_2SO_4 brines. *Chemical Geology*, **280**(1-2), 26-32.

Parker, A.P., Clay, P.L., Boudreau, A.E., Burgess, R., and O'Driscoll, B. (2022). Magmatic volatiles and platinum-group element mineralization in the Stillwater layered intrusion, U.S.A. *American Mineralogist*, **107**(5), 797-814.

Parker, A.P., Clay, P.L., Burgess, R., Balcone-Boissard, H., Bürckel, P., and O'Driscoll, B. (2019). Halogen cycling and precious metal enrichment in sub-volcanic magmatic systems: Insights from the Rum layered intrusion, Scotland. *Earth and Planetary Science Letters*, **526**, 115769.

Pattison, E.F. (1979). The Sudbury Sublayer. *Canadian Mineralogist*, **17**, 257-274.

Petrus, J.A., Ames, D.E., and Kamber, B.S. (2015). On the track of the elusive Sudbury impact: geochemical evidence for a chondrite or comet bolide. *Terra Nova*, **27**, 9-20.

Pilles, E.A., Osinski, G.R., and Grieve, R.A.F. (2022). The Offset Dykes in the North and East Range of the Sudbury impact structure, Canada: A synthesis. *Earth-Science Reviews*, **235**, 104268.

Pilles, E.A., Osinski, G.R., Grieve, R.A.F., Smith, D., and Bailey, J. (2018). Formation of large-scale impact melt dikes: A case study of the Foy Offset Dike at the Sudbury impact structure, Canada. *Earth and Planetary Science Letters*, **495**, 224-233.

Reimold, W.U., and Gibson, R.L. (2005). "Pseudotachylites" in Large Impact Structures. In C. Koeberl and H. Henkel (Eds.), *Impact Tectonics* (p. 1-53). Springer.

Ripley, E.M., Lightfoot, P.C., Stifter, E.C., Underwood, B., Taranovic, V., Dunlop, M., and Donoghue, K.A. (2015). Heterogeneity of S isotope compositions in the Sudbury Igneous Complex, Canada: Significance to formation of Ni-Cu sulfide ores and the host rocks. *Economic Geology*, **110**, 1125-1135.

Rousell, D.H. (1984). Structural Geology of the Sudbury Basin. In E. Pye, A.J. Naldrett, and P.E. Giblin (Eds.), *The Geology and Ore Deposits of the Sudbury Structure* (p. 89-95). Ontario Geological Survey Special Volume 1.

Rousell, D.H., Fedorowich, J.S., and Dressler, B.O. (2003). Sudbury Breccia (Canada): a product of the 1850 Ma Sudbury Event and host to footwall Cu-Ni-PGE deposits. *Earth-Science Reviews*, **60**, 147-174.

Rousell, D.H., Gibson, H.L., and Jonasson, I.R. (1997). The Tectonic, Magmatic and Mineralization History of the Sudbury Structure. *Exploration and Mining Geology*, **6**, 1-22.

Ruzié-Hamilton, L., Clay, P.L., Burgess, R., Joachim, B., Ballentine, C.J., and Turner, G. (2016). Determination of halogen abundances in terrestrial and extraterrestrial samples by the analysis of noble gases produced by neutron irradiation. *Chemical Geology*, **437**, 77-87.

Saini-Eidukat, B., Kucha, H., and Keppler, H. (1994). Hibbingite, y-$Fe_2(OH)_3Cl$, a new mineral from the Duluth Complex, Minnesota, with implications for the oxidation of Fe-bearing compounds and the transport of metals. *American Mineralogist*, **79**, 555-561.

Schoonen, M.A.A., and Barnes, H.L. (1991). Mechanisms of pyrite and marcasite formation from solution: III. Hydrothermal processes. *Geochimica et Cosmochimica Acta*, **55**, 3491-3504.

Schwarcz, H.P. (1973). Sulfur Isotope Analyses of Some Sudbury, Ontario, Ores. *Canadian Journal of Earth Sciences*, **10**(9), 1444-1459.

Scott, R.G., and Benn, K. (2002). Emplacement of Sulfide Deposits in the Copper Cliff Offset Dike during Collapse of the Sudbury Crater Rim: Evidence from Magnetic Fabric Studies. *Economic Geology*, **97**, 1447-1458.

Scott, R.G., and Spray, J.G. (1999). Magnetic fabric constraints on friction melt flow regimes and ore emplacement direction within the South Range Breccia Belt, Sudbury Impact Structure. *Tectonophysics*, **307**, 163-189.

Shanks W.S., and Schwerdtner, W.M. (1991). Structural analysis of the central and southwestern Sudbury structure, Southern province, Canadian shield. *Canadian Journal of Earth Sciences*, **28**, 411-430.

Sims, P.K., Van Schmus, W.R., Schulz, K.J., and Peterman, Z.E. (1989). Tectono-stratigraphic evolution of the Early Proterozoic Wisconsin magmatic terranes of the Penokean Orogen. *Canadian Journal of Earth Sciences*, **26**, 2145-2158.

Sinyakova, E.F., and Kosyakov, V.I. (2007). Experimental modeling of zoning in copper-nickel sulfide ores. *Doklady Earth Sciences*, **417**(2), 1380-1385.

Springer, G. (1989). Chlorine-bearing and other uncommon minerals in the Strathcona Deep Copper Zone, Sudbury District, Ontario. *Canadian Mineralogist*, **27**, 311-313.

Sullivan, N.A., Zajacz, Z., Brenan, J.M., and Tsay, A. (2022). The solubility of platinum in magmatic brines: Insights into the mobility of PGE in ore-forming environments. *Geochimica et Cosmochimica Acta*, **316**, 253-272.

Szabó, E., and Halls, H.C. (2006). Deformation of the Sudbury Structure: Paleomagnetic evidence from the Sudbury breccia. *Precambrian Research*, **150**(1-2), 27-48.

Therriault, A.M., Fowler, A.D., and Grieve, R.A.F. (2002). The Sudbury Igneous Complex: A Differentiated Impact Melt Sheet. *Economic Geology*, **97**, 1521-1540.

Thompson, L.M., Spray, J.G., and Kelley, S.P. (1998). Laser probe argon-40/argon-39 dating of pseudotachylyte from the Sudbury structure: Evidence for postimpact thermal overprinting in the North Range. *Meteoritics and Planetary Science*, **33**(6), 1259-1269.

Thomson, R. (1935). The “Offset Dykes” of the Nickel Intrusive, Sudbury, Ontario. *American Journal of Science*, **30**, 356-367.

Tuba, G., Molnár, F., Ames, D.E., Péntek, A., Watkinson, D.H., and Jones, P.C. (2014). Multi-stage hydrothermal processes involved in “low-sulfide” Cu(-Ni)-PGE mineralization in the footwall of the Sudbury Igneous Complex (Canada): Amy Lake PGE zone, East Range. *Mineralium Deposita*, **49**(1), 7-47.

Wodicka, N. (1997). Sudbury Structure: Northern footwall rocks and Sudbury Igneous complex. in Timmins to Sudbury Transect: New Insights into the Regional Geology and Setting of Mineral Deposits. In D.E. Ames (Ed.), *Joint Annual Meeting* (p. 73-93). Geological Association of Canada-Mineralogical Association of Canada.

Wood, S.A. (2002). The Aqueous Geochemistry of the Platinum-Group Elements with Applications to Ore Deposits. In L.J. Cabri (Ed.), *The Geology, Geochemistry, Mineralogy, and Mineral Beneficiation of Platinum-Group Elements* (p. 211-249). Canadian Institute of Mining, Metallurgy and Petroleum Special Volume 54.

Wood, C.R., and Spray, J.G. (1998). Origin and emplacement of Offset Dykes in the Sudbury impact structure: Constraints from Hess. *Meteoritics and Planetary Science*, **33**(2), 337-347.

Zieg, M.J., and Marsh, B.D. (2005). The Sudbury Igneous Complex: Viscous emulsion differentiation of a superheated impact melt sheet. *Bulletin of the Geological Society of America*, **117**(11-12), 1427-1450.

Appendix

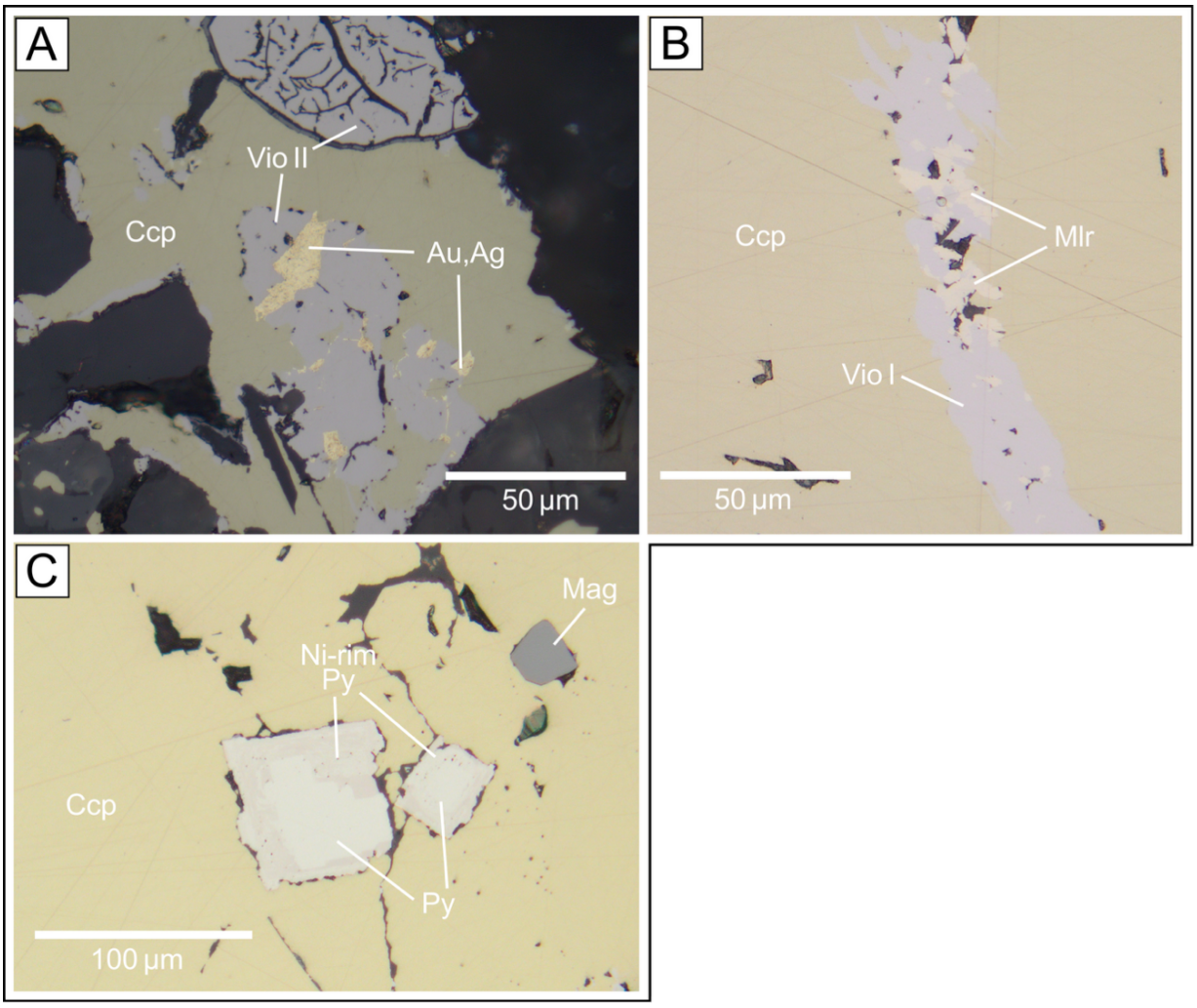

Figure A1. Additional reflected light photomicrographs. A) Native gold hosted by violarite II from the immediate contact in TS 7. Note the unique fracturing of the violarite due to its formation by replacement of pentlandite. B) Small veinlet of violarite I intergrown with millerite from the Inner Vein, TS 3. C) Zoned pyrite with pinker Ni-rich rims from TS 1.

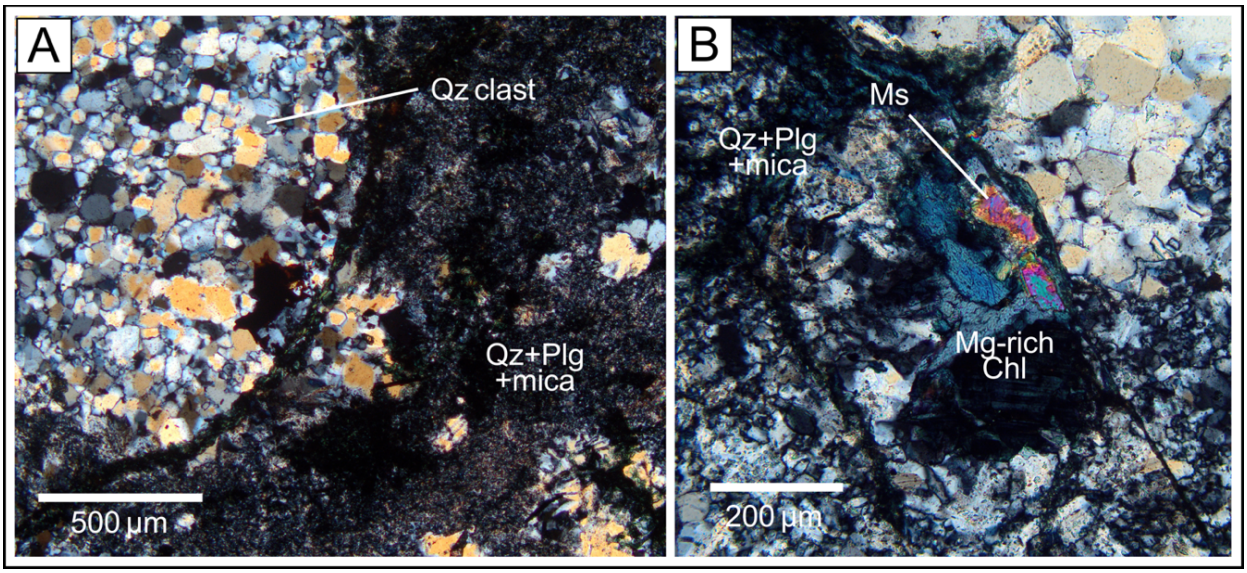

Figure A2. Additional crossed polarized light photomicrographs. A) Quartz clast located within the host rock metabreccia (TS 10). The clast is hosted by the very fine-grained highly altered quartz, plagioclase, and mica-rich matrix. B) Anomalous blue chlorite located furthest from the sulfide vein (TS 15).

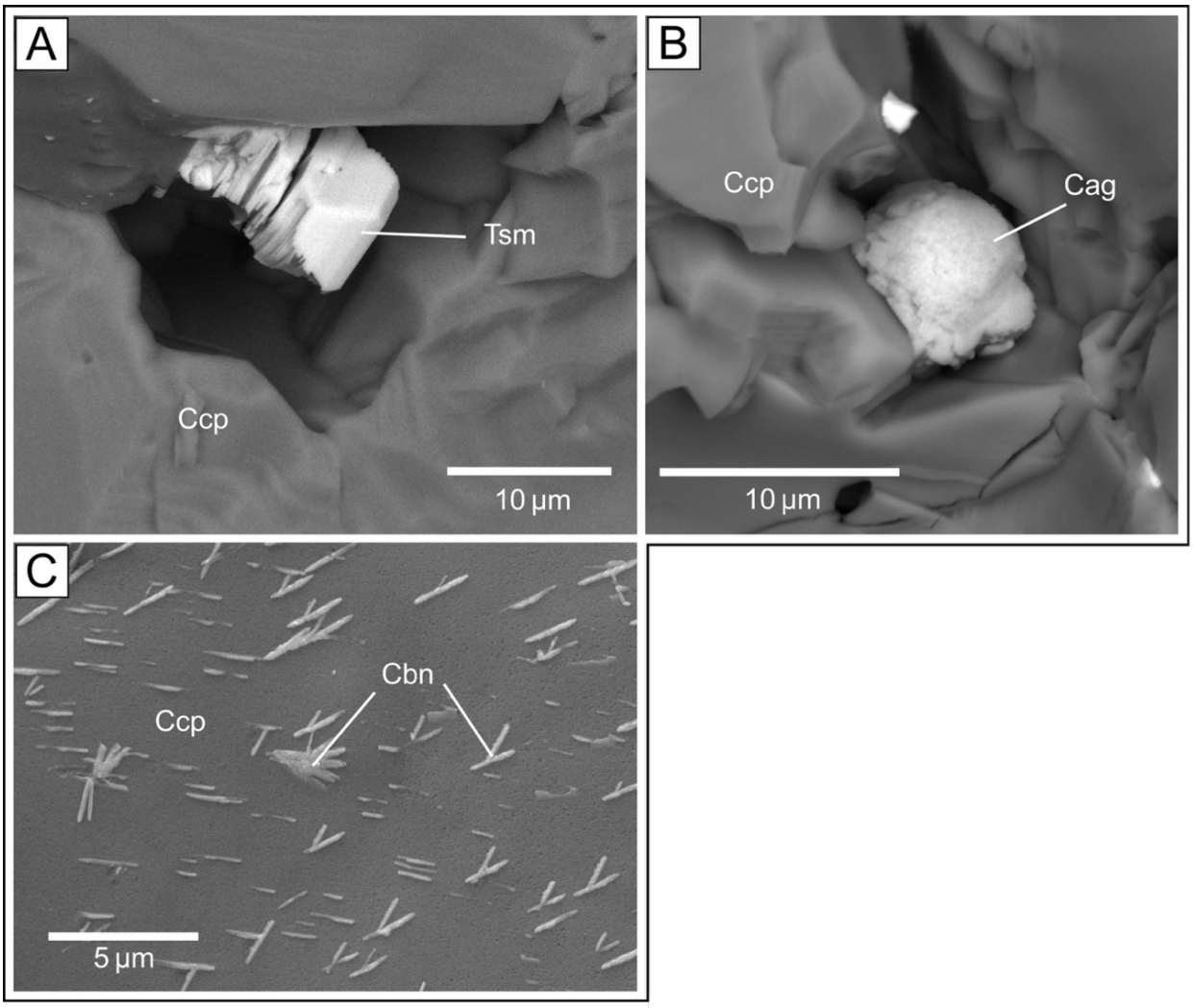

Figure A3. Additional backscattered electron images from the FE-SEM. A) Stacked hexagonal plates of daughter tsumoite growing within a vacant fluid inclusion from TS 1. B) Crust-like chlorargyrite (daughter mineral) also growing within a fluid inclusion in TS 1. C) Cubanite exsolutions showing preferred orientation, though SEM spot analysis does not confirm the composition of cubanite (see Chapter 6.2.3).

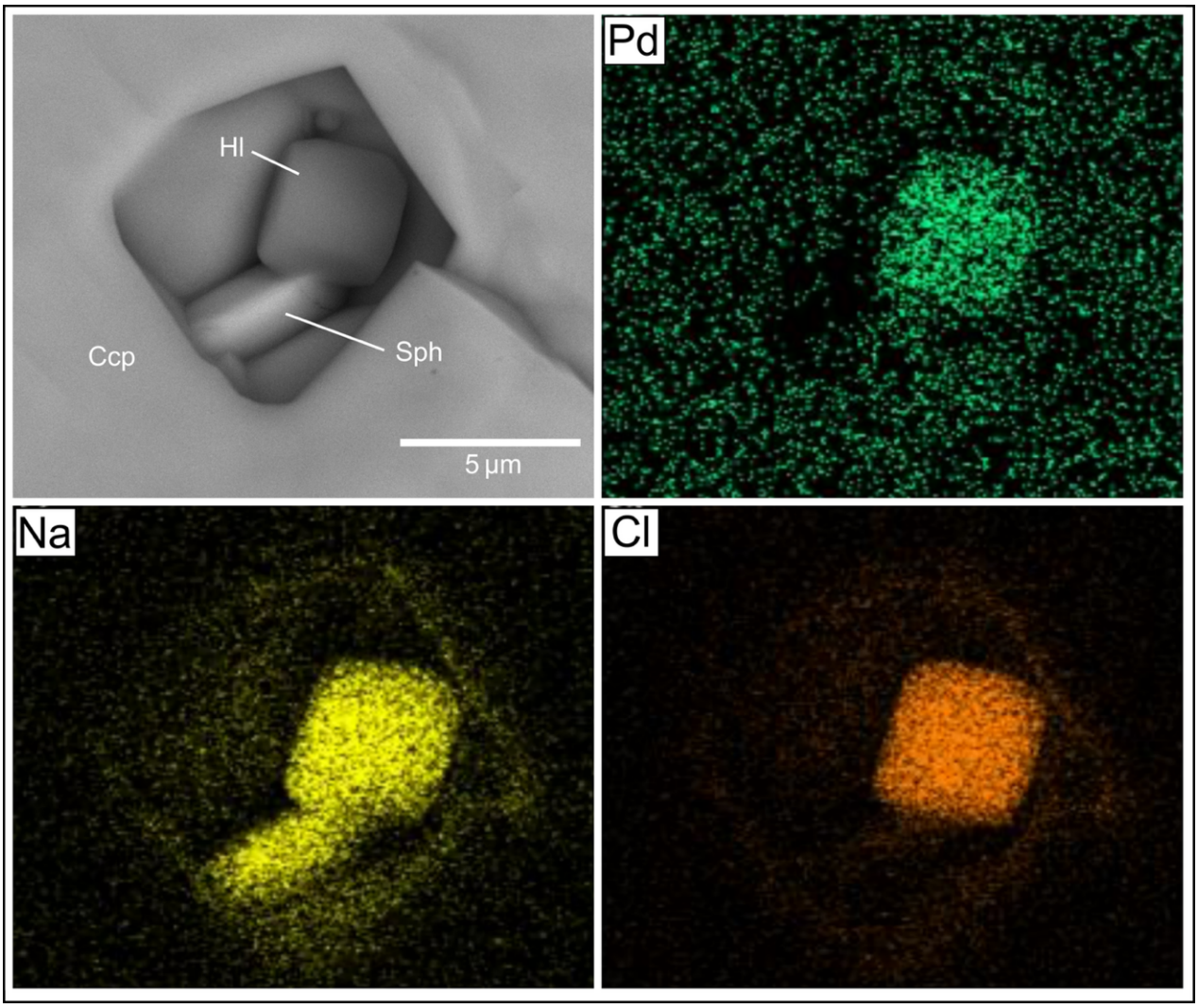

Figure A4. Backscattered electron image of daughter minerals within a fluid inclusion (TS 1) using the FE-SEM's mapping feature. Element maps coinciding with the first image, show the composition of halite as sodium (yellow) and chlorine (orange) with a concentration of palladium (green). The highlighted sphalerite in map Na is due to the peak overlap typical of Na and Zn.

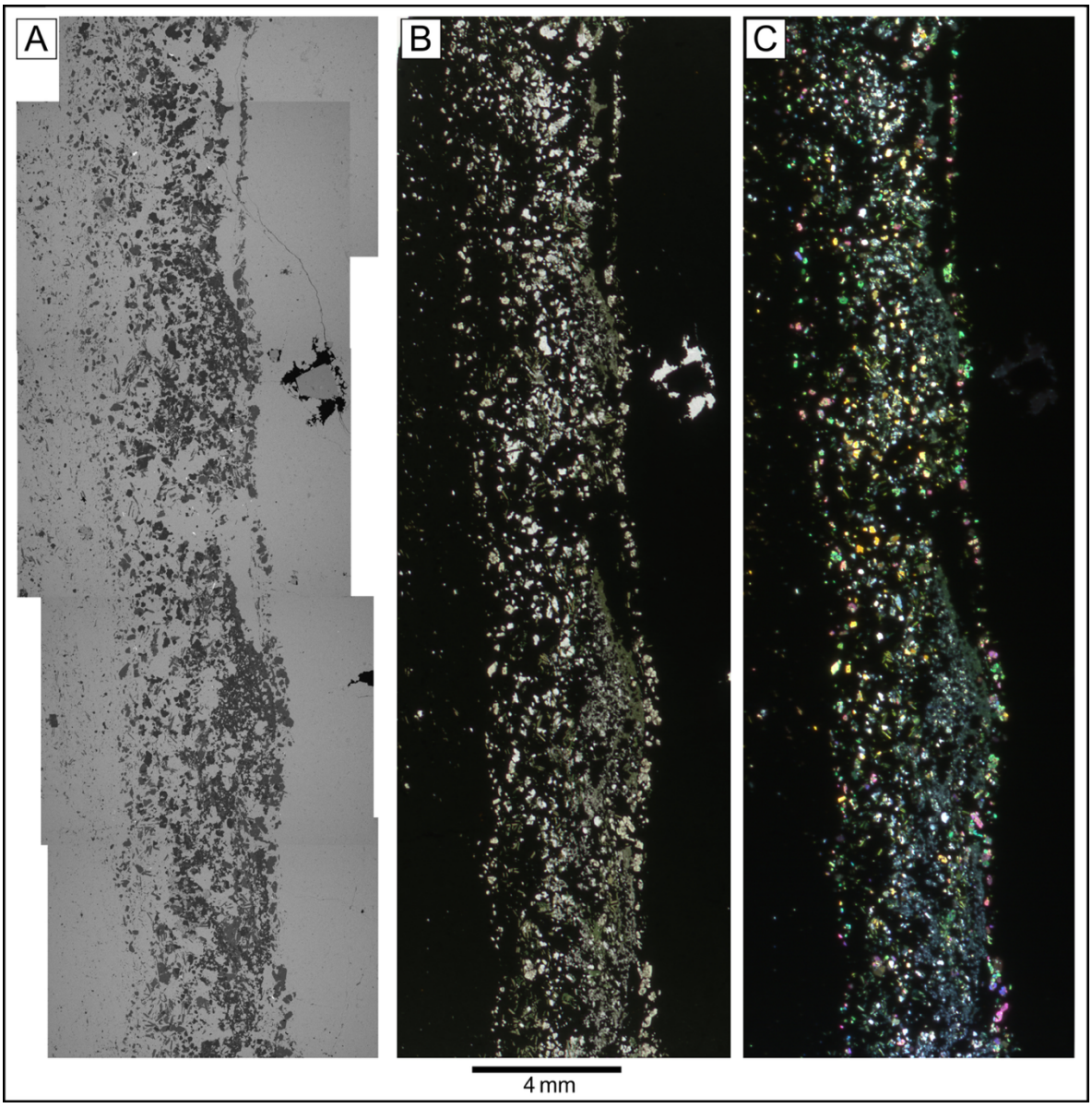

Figure A5. Parallel images of the epidote band closest to the Contact Zone, located within the Outer Vein (TS 6). Note the lack of fluid inclusions in the sulfide to the right of band and a more diffuse left margin of the band visible in A). Images are in the following formats: A) Composite backscattered electron. B) Plane polarized light. C) Crossed polarized light.

Table A6. Mineral chemistry for all minerals identified with scanning electron microscopy. The calculated formula is given as an average of analysis from multiple grains and spots.

Mineral	Abbr.	Ideal Formula	Calculated Formula
		Major and minor minerals	
Chalcopyrite	Ccp	$CuFeS_2$	$Cu_{1.03}Fe_{1.00}S_{1.99}$
Pyrrhotite	Po	Fe_7S_8	$Fe_{7.14}S_{8.00}$
Magnetite	Mag	Fe_3O_4	$Fe_{3.10}O_{4.08}$
Violarite	Vio	$FeNi_2S_4$	$(Fe_{0.69},Co_{0.07})_{=0.76}Ni_{2.30}S_{4.00}$
Marcasite	Mrc	FeS_2	$Fe_{0.99}S_{2.00}$
Quartz	Qz	SiO_2	$Si_{2.00}O_{2.43}$
Chamosite	Chl	$(Fe,Mg,Al)_6(Si,Al)_4O_{10}(OH,O)_8$	$(Fe_{4.02},Mg_{1.27},Al_{1.59})_{=6.88}(Si_{3.00},Al_{1.60})_{=4.60}O_{10.00}(OH,O)_{8.13}$
Epidote	Epi	$Ca_2(Al_2Fe)Si_2O_7(SiO_4)O(OH)$	$Ca_{2.00}(Al_{2.10}Fe_{0.73})Si_{2.00}O_{7.00}(Si_{0.66}O_{4.00})O_{1.35}(OH)_{1.20}$
Mineral	**Abbr.**	**Ideal Formula**	**Calculated Formula**
		Trace and rare minerals	
Fe-, Ni-bearing			
Millerite	Mlr	NiS	$Ni_{0.99}S_{1.00}$
(Ni-)Pyrite	Py	$(Fe,Ni)S_2$	$(Fe_{0.92},Ni_{0.20},Co_{0.02})_{=1.14}S_{1.99}$
Siegenite	Seg	$(Co,Ni,Fe)_3S_4$	$(Co_{0.43},Ni_{2.15},Fe_{0.44})_{=3.02}S_{4.01}$
Hematite	Hem	Fe_2O_3	$Fe_{1.78}O_{2.85}$
Goethite	Gth	$FeO(OH)$	$Fe_{1.01}O_{1.00}(OH)_{0.93}$
Cu-bearing			
Covellite	Cv	CuS	$Cu_{0.97}S_{0.99}$
Cubanite	Cbn	$CuFe_2S_3$	$Cu_{1.28}Fe_{2.09}S_{2.78}$
Co-, Ni-arsenides			
Cobaltite-Gersdorffite	Cbt-Gdf	(Co,Ni)AsS	$(Co_{0.46},Ni_{0.43})_{=0.89}As_{1.03}S_{1.00}$
Sn-bearing			
Cassiterite	Cst	SnO_2	$Sn_{1.00}O_{2.45}$
Other base metal minerals			
Sphalerite	Sph	ZnS	$(Zn_{0.98},Cd_{0.02},Fe_{0.10})_{=1.10}S_{1.09}$
Galena	Gn	PbS	$Pb_{1.05}S_{1.05}$
Bi-, Te-bearing			
Tsumoite	Tsm	BiTe	$Bi_{1.03}Te_{0.98}$
Hedleyite	Hdl	Bi_2Te	$Bi_{2.00}Te_{1.11}$
Tetradymite-Kawazulite	Ttd-Kaw	$Bi_2Te_2(S,Se)$	$Bi_{2.10}Te_{1.76}(S_{0.77},Se_{0.38})_{=1.15}$
Sulphotsumoite	Stsm	Bi_3Te_2S	$Bi_{3.00}Te_{2.15}S_{1.04}$
Tellurite	Tlr	TeO_2	$Te_{0.98}O_{2.03}$
Native bismuth		Bi>Te	$Bi_{0.98}$:$Te_{0.02}$
Precious metal minerals (Ag, Au)			
Hessite	Hes	Ag_2Te	$Ag_{2.14}Te_{0.98}$
Matildite-Bohdanowizite	Mtd-Boh	$AgBi(S,Se)_2$	$Ag_{0.99}Bi_{1.02}(S_{1.40},Se_{0.54})_{=1.93}$
Acanthite	Aca	Ag_2S	$Ag_{2.00}S_{1.09}$
Naumannite	Nau	Ag_2Se	$Ag_{2.00}(Se_{0.85},S_{0.58})_{=1.43}$
Native gold		Au>Ag	$Au_{0.67}$:$Ag_{0.33}$

Table A6 (con't). Mineral chemistry for all minerals identified with scanning electron microscopy. The calculated formula is given as an average of analysis from multiple grains and spots.

Mineral	Abbr.	Formula	Calculated Formula
		Trace and rare minerals (con't)	
Platinum-Group Minerals (Pd, Pt)			
Sperrylite	Spy	$PtAs_2$	$Pt_{1.00}As_{1.98}$
Merenskyite	Mrk	$PdTe_2$	$Pd_{1.00}(Te_{1.79},Bi_{0.16})_{=1.95}$
Kotulskite	Kot	Pd(Te,Bi)	$Pd_{1.00}(Te_{0.89},Bi_{0.20})_{=1.09}$
Michenerite	Mch	PdBiTe	$Pd_{1.02}Bi_{0.98}Te_{1.10}$
Cl-bearing			
Halite	Hl	NaCl	$Na_{1.00}Cl_{0.85}$
Chlorargyrite	Cag	AgCl	$Ag_{0.98}(Cl_{0.73},I_{0.05})_{=0.78}$
Cotunnite	Cot	$PbCl_2$	$Pb_{1.00}Cl_{2.48}$
Hibbingite	Hib	$Fe_2(OH)_3Cl$	$Fe_{1.87}(OH)_{2.69}Cl_{1.43}$
Ferropyrosmalite	Pys-Fe	$(Fe,Mn)_8Si_6O_{15}(OH,Cl)_{10}$	$(Fe_{7.68},Mn_{0.46})_{=8.14}Si_{6.00}O_{15.00}(OH_{8.48},Cl_{1.63})_{=10.11}$
Ti-bearing			
Rutile	Rt	TiO_2	$Ti_{1.01}O_{2.24}$
Ilmenite	Ilm	$FeTiO_3$	$Fe_{0.94}Ti_{0.98}O_{3.21}$
Titanite	Ttn	$CaTiSiO_5$	$Ca_{1.18}Ti_{0.96}Si_{1.09}O_{4.96}$
Phosphates			
Apatite	Ap	$Ca_5(PO_4)_3F$	$Ca_{5.00}(PO_{4.35})_{2.73}F_{0.86}$
Monazite- Ce	Mnz	$Ce(PO_4)$	$(Ce_{0.37},La_{0.22},Nd_{0.13},Sm_{0.02})(PO_{4.06})$
Sulfates			
Barite	Brt	$Ba(SO_4)$	$Ba_{1.01}(S_{0.97}O_{3.74})$
Anhydrite	Anh	$Ca(SO_4)$	$Ca_{1.03}(S_{0.92}O_{3.63})$
Silicates			
Albite-Anorthite	Ab-An	$(Na,Ca)AlSi_3O_8$	$(Na_{0.80},Ca_{0.20})_{=1.00}Al_{1.04}Si_{2.43}O_{7.54}$
K-feldspar	Ksp	$KAlSi_3O_8$	$K_{1.00}Al_{1.13}Si_{3.00}O_{8.35}$
Muscovite	mica	$KAl_2(Si_3Al)O_{10}(OH)_2$	$K_{1.00}Al_{1.60}(Si_{3.27}Al_{0.94})O_{10}(OH)_{2.20}$
Zircon	Zrn	$ZrSiO_4$	$Zr_{0.96}Si_{1.00}O_{4.13}$
Kaolinite	mica	$Al_2Si_2O_5(OH)_4$	$Al_{2.22}Si_{2.00}O_{5.10}(OH)_{4.36}$

Table A7. Electron probe micro-analysis for spot analyses on chlorite. Grid locations are provided at the end of Table A8.

TS	Grid	cm	SiO_2	TiO_2	Al_2O_3	Cr_2O_3	FeO	NiO	MnO	MgO	CaO	Na_2O	K_2O	Cl	O	H_2O
Chlorite Upper transect																
6	1	14.1	22.85	0.03	19.52		36.62	0.96	0.38	6.81	0.00		0.02	0.01	0.00	10.73
6	2	14.3	23.16	0.03	19.75	0.02	36.18	1.07	0.46	6.84			0.03	0.02	0.00	10.76
6	3	15.1	22.84	0.04	18.96		39.83	1.03	0.49	4.44	0.00		0.03	0.02	0.00	10.55
7	7	17.2	23.32	0.03	19.77	0.03	35.90	0.83	0.43	7.16	0.01		0.03	0.01	0.00	10.79
7	10	19.1	23.06	0.02	19.72	0.02	36.30	0.69	0.42	7.09	0.01	0.00	0.02	0.02	0.00	10.77
8	11	20	23.33	0.03	20.10		36.40	0.47	0.38	7.08			0.04	0.02	0.00	10.79
8	12	20.8	23.13	0.01	19.83		36.85	0.34	0.46	7.17	0.00		0.03	0.01	0.00	10.76
8	13	21.1	23.21	0.03	19.77		37.05	0.35	0.44	7.09	0.01		0.01	0.02	0.00	10.75
8	14	21.8	23.21	0.02	20.07		36.19	0.41	0.40	7.27	0.01	0.02	0.05	0.02	-0.01	10.80
8	14.5	22.1	24.10	0.08	19.50		35.18	0.54	0.44	8.48	0.00		0.05	0.02	0.00	10.86
8	16	23.5	23.04	0.04	20.02		37.97	0.63	0.47	6.27	0.03		0.01	0.01	0.00	10.69
10	19	24.6	23.16	0.03	19.84	0.01	38.18	0.17	0.47	6.78	0.02		0.03	0.02	0.00	10.70
10	19.5	24.8	22.96	0.04	20.15	0.05	38.01	0.17	0.45	6.69	0.02	0.02	0.04	0.02	0.00	10.70
10	21	25.4	23.24	0.04	20.07	0.02	36.90	0.14	0.44	7.34	0.02		0.05	0.02	0.00	10.77
10	23	27	21.13	0.03	18.39		34.39	0.09	0.44	7.35	0.01	0.02	0.04	0.03	-0.01	10.85
10	23.5	27.5	24.25	0.04	20.67		36.27	0.08	0.42	7.54	0.02	0.02	0.03	0.01	0.00	10.85
10	24	28.2	23.35	0.03	20.12		35.64	0.11	0.38	7.98	0.02	0.03	0.03	0.02	0.00	10.85
Chlorite Middle transect																
6	1	13.9	22.48	0.04	19.15		41.79	1.02	0.48	3.57	0.00		0.03	0.01	0.00	10.43
6	1.5	14.2	22.71	0.01	19.33		39.34	1.01	0.50	5.12	0.01	0.01	0.02	0.01	0.00	10.57
6	2	14.4	23.60	0.02	19.51		36.50	0.61	0.33	6.55	0.03		0.04	0.02	-0.01	10.79
6	2.5	14.5	23.07	0.03	19.90	0.02	35.50	0.92	0.39	7.30	0.00	0.01	0.03	0.01	0.00	10.81
6	3	15.3	22.75	0.04	19.58	0.02	39.02	1.06	0.48	5.41	0.01		0.02	0.01	0.00	10.59
7	8	17.5	22.74	0.03	19.97		37.35	1.00	0.47	6.23		0.01	0.02	0.02	0.00	10.69
7	8.5	17.9	23.09	0.02	19.67		36.54	0.83	0.38	7.30			0.02	0.01	0.00	10.75
8	15	22.4	23.12	0.03	19.87		36.45	0.54	0.47	7.31	0.01	0.00	0.01	0.01	0.00	10.77
8	15.3	22.5	22.91	0.03	19.86	0.00	37.97	0.52	0.44	6.41	0.02	0.01	0.05	0.02	0.00	10.68
8	15.7	22.6	24.07	0.02	19.44		35.66	0.52	0.41	7.02	0.01	0.01	0.06	0.02	0.00	10.85
10	20	25	22.99	0.03	20.10	0.04	37.37	0.18	0.44	7.12	0.01	0.00	0.02	0.02	0.00	10.74
10	24	28	25.42	0.03	18.04		34.79	0.06	0.41	9.73	0.04		0.04	0.02	0.00	10.92

Table A7 (con't). Electron probe micro-analysis for spot analyses on chlorite. Grid locations are provided at the end of Table A8.

TS	Grid	cm	SiO_2	TiO_2	Al_2O_3	Cr_2O_3	FeO	NiO	MnO	MgO	CaO	Na_2O	K_2O	Cl	O	H_2O
Chlorite Lower transect																
6	1	14.3	22.70	0.03	19.81		36.88	1.05	0.42	6.27			0.03	0.01	0.00	10.71
6	2	14.6	22.66	0.03	19.69		37.70	1.04	0.42	6.21	0.00	0.01	0.03	0.01	0.00	10.66
6	3	15.4	21.90	0.02	19.27	0.04	42.24	0.66	0.43	2.86	0.01		0.02	0.03	-0.01	10.41
7	8	18	23.05	0.03	19.78		36.56	0.84	0.41	6.97	0.00		0.03	0.02	-0.01	10.75
7	9	18.4	23.71	0.02	19.06	0.02	35.86	0.69	0.34	7.91	0.02		0.03	0.02	0.00	10.81
7	9.33	18.6	22.99	0.03	20.00		36.28	0.74	0.39	6.85	0.02	0.00	0.01	0.02	0.00	10.78
7	9.67	18.8	23.24	0.04	19.99		36.85	0.64	0.42	7.19	0.00	0.01	0.01	0.02	0.00	10.75
7	10	19.1	23.12	0.03	20.09		36.48	0.65	0.41	7.11	0.02		0.03	0.02	0.00	10.77
7	11	20	23.13	0.04	20.00		36.76	0.46	0.42	7.02	0.01	0.01	0.02	0.02	0.00	10.76
8	12	20.5	23.10	0.05	19.92		37.06	0.36	0.40	7.39	0.01	0.02	0.02	0.02	0.00	10.75
8	15	22.7	23.18	0.03	19.79		36.61	0.57	0.42	7.02	0.01		0.03	0.02	0.00	10.77
8	16	23.4	23.47	0.03	19.83	0.04	36.54	0.61	0.48	7.30	0.01	0.01	0.01	0.02	0.00	10.77
10	21	25.4	23.62	0.03	19.26		36.34	0.22	0.43	7.96	0.01	0.00	0.02	0.02	0.00	10.80
10	22	26.3	23.16	0.03	20.13	0.05	36.88	0.10	0.45	7.56	0.00		0.05	0.02	0.00	10.77
10	22.5	26.5	23.05	0.14	19.88		36.78	0.07	0.44	7.25	0.04		0.03	0.01	0.00	10.78

Table A8. Electron probe micro-analysis for spot analyses on epidote. Grid locations are provided at the end of Table A8.

TS	Grid	cm	SiO_2	TiO_2	Al_2O_3	Cr_2O_3	FeO	NiO	MnO	MgO	CaO	Na_2O	K_2O	Cl	O	H_2O
Epidote Upper transect																
6	1	14.1	37.24	0.04	22.89	0.02	13.61	0.00	0.12		23.26		0.01		0.00	1.88
6	1.5	14.2	37.39	0.03	23.38	0.03	13.03	0.00	0.11	0.00	23.31	0.01	0.01		0.00	1.89
6	2	14.5	37.42	0.03	23.17	0.01	12.97	0.01	0.14	0.02	22.94		0.02	0.00	0.00	1.88
7	7	17.3	36.93	0.04	23.21	0.01	13.08	0.02	0.11		23.09	0.01	0.02	0.00	0.00	1.89
7	10	19.3	37.23	0.05	23.14	0.02	12.67	0.00	0.14	0.01	23.23		0.02			1.89
7	11	19.9	37.51	0.04	23.16	0.01	13.39	0.01	0.16	0.03	23.07	0.00	0.02	0.01	0.00	1.89
8	12	20.9	37.46	0.03	23.36	0.00	13.36	0.02	0.14	0.02	23.04	0.01	0.01	0.00	0.00	1.89
8	13	21.1	37.55	0.03	23.06	0.06	13.43		0.14		23.17	0.00	0.02	0.00	0.00	1.89
8	14	21.8	37.51	0.06	23.19		13.13	0.02	0.13		23.05		0.07			1.89
8	14.5	22.1	37.41	0.03	22.82	0.01	13.64	0.00	0.18	0.01	22.94	0.00	0.02	0.00	0.00	1.89
8	15	22.5	37.51	0.03	22.97	0.02	13.48	0.02	0.20		22.93	0.00	0.02	0.00	0.00	1.89
8	16	23	37.53	0.03	22.90	0.02	13.48	0.01	0.14	0.01	23.01	0.01	0.02	0.00	0.00	1.89
8	16.5	23.5	37.79	0.02	23.35		12.83		0.19		23.05	0.01	0.02			1.89
8	17	24	37.68	0.07	23.12		13.01		0.15	0.01	22.83	0.03	0.02	0.01	0.00	1.89
10	19	24.7	37.71	0.03	23.06	0.01	13.84	0.01	0.13	0.01	23.09	0.03	0.03	0.01	0.00	1.89
Epidote Middle transect																
6	1	14	37.40	0.02	22.52	0.05	14.00	0.02	0.08	0.02	23.18		0.02			1.88
6	1.5	14.2	37.23	0.06	23.02	0.03	13.14	0.02	0.15	0.00	23.24	0.01	0.02	0.00	0.00	1.89
6	2	14.5	37.41	0.01	23.26		13.05	0.00	0.13		23.26	0.01	0.01	0.00	0.00	1.89
6	2.5	14.6	37.25	0.03	23.23		12.90	0.03	0.14	0.00	23.12	0.01	0.02	0.00	0.00	1.89
6	3	15.3	37.33	0.08	22.71	0.01	13.43	0.04	0.15		22.92	0.02	0.01			1.89
7	8	18.1	36.75	0.02	22.30		14.04		0.12	0.00	22.79	0.01	0.02			1.88
8	15	22.4	37.38	0.02	22.58	0.03	13.99	0.02	0.10		23.19	0.01	0.02		0.00	1.88
8	15.5	22.7	37.58	0.06	23.02	0.03	13.16	0.01	0.15		23.05	0.00	0.02	0.00	0.00	1.89
10	20	24.9	37.60	0.02	23.35		13.24		0.13		23.34		0.02			1.89
10	24	28.2	37.86	0.04	22.83		14.03		0.12		22.98		0.02	0.00	0.00	1.89

Table A8 (con't). Electron probe micro-analysis for spot analyses on epidote. Grid locations are provided at the end of Table A8.

TS	Grid	cm	SiO_2	TiO_2	Al_2O_3	Cr_2O_3	FeO	NiO	MnO	MgO	CaO	Na_2O	K_2O	Cl	O	H_2O
Epidote Lower transect																
6	1	14.4	37.46	0.04	23.23	0.01	13.06	0.01	0.15		23.24		0.01	0.00	0.00	1.89
6	2	14.7	37.31	0.08	23.24	0.00	13.09	0.01	0.15		23.23		0.01	0.01	0.00	1.89
7	7	17.1	37.08	0.04	23.28	0.03	12.77	0.01	0.17		22.98	0.01	0.02	0.00	0.00	1.89
7	8	18	37.42	0.01	22.99	0.01	13.36		0.10	0.00	23.22	0.00	0.02	0.00	0.00	1.89
7	8.33	18.1	37.20	0.04	22.79		13.57		0.09		23.19		0.02	0.00	0.00	1.88
7	8.67	18.2	37.20	0.02	23.54		12.75		0.13		23.12		0.01			1.89
7	9	18.4	37.24	0.10	22.89		13.01	0.01	0.13		23.06	0.01	0.03		0.00	1.89
7	9.33	18.7	37.26	0.02	23.06	0.03	13.30	0.01	0.19		22.80	0.00	0.02		0.00	1.89
7	9.67	18.9	37.22	0.09	23.36	0.02	13.05	0.01	0.13	0.17	22.81	0.01	0.02	0.01	0.00	1.89
7	10	19.2	37.26	0.01	23.10		13.76	0.00	0.15	0.14	22.47	0.00	0.03	0.00	0.00	1.89
7	11	19.7	37.23	0.02	23.04		13.11	0.03	0.15	0.00	22.91	0.01	0.01	0.00	0.00	1.89
8	12	20.4	37.36	0.04	23.38		13.31	0.01	0.16	0.00	23.11	0.00	0.02	0.00	0.00	1.89
8	15	22.5	37.19	0.03	22.24	0.01	13.88		0.07		22.98		0.01			1.88
8	16	23.3	37.39	0.05	23.06	0.01	13.11		0.14		23.07		0.02	0.00	0.00	1.89
8	17	23.8	37.39	0.20	22.85	0.04	13.31	0.00	0.12	0.00	23.28	0.01	0.02	0.00	0.00	1.89
10	20	25.1	37.54	0.09	23.14		13.02		0.24		22.88		0.01	0.01	0.00	1.89
10	21	25.4	37.83	0.09	23.15		13.27		0.21		23.00		0.01	0.00	0.00	1.89

Rough grid locations for chlorite and epidote, each vertical section is labelled 1 to 24. Some images may be upside down due to error in scan orientation, but data is adjusted to reflect this.

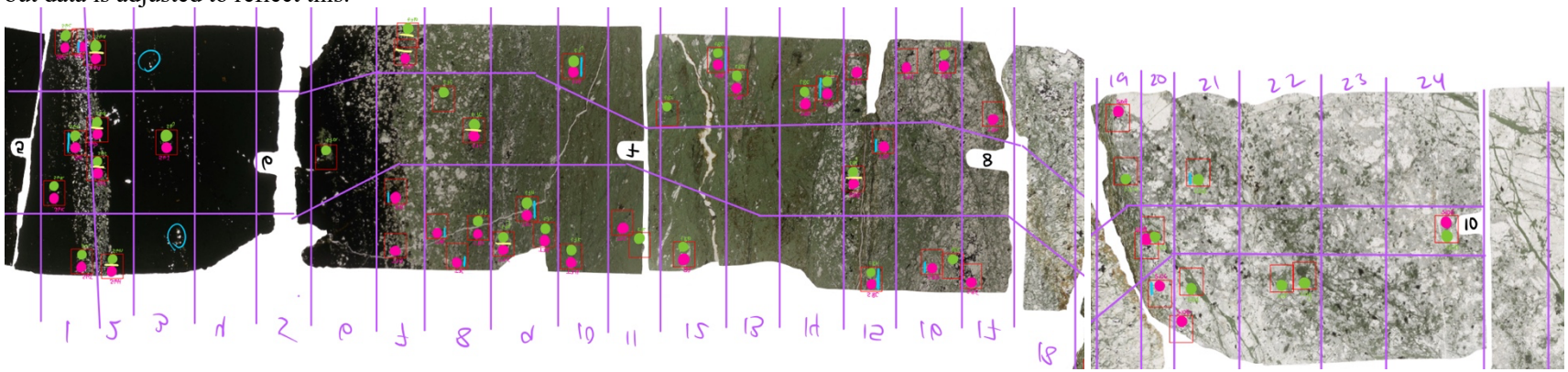

Table A9. μXRF maps of individual minerals and selected elements.

Chalcopyrite	***Chlorite***
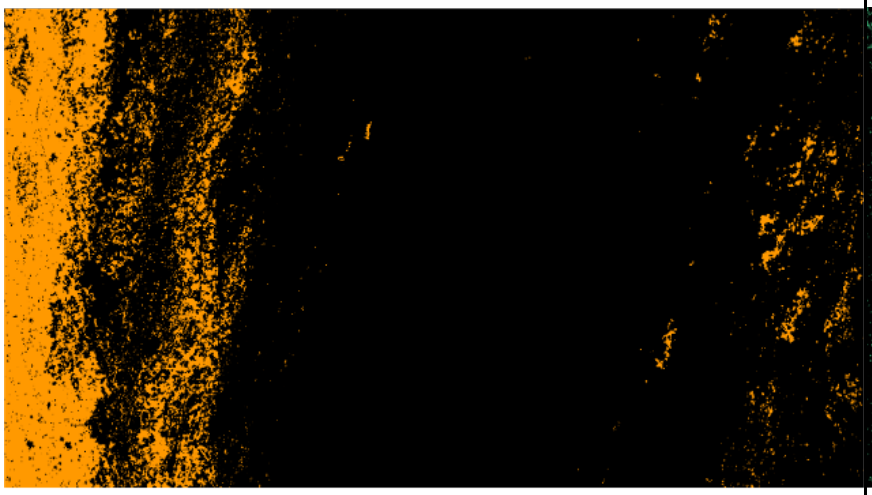	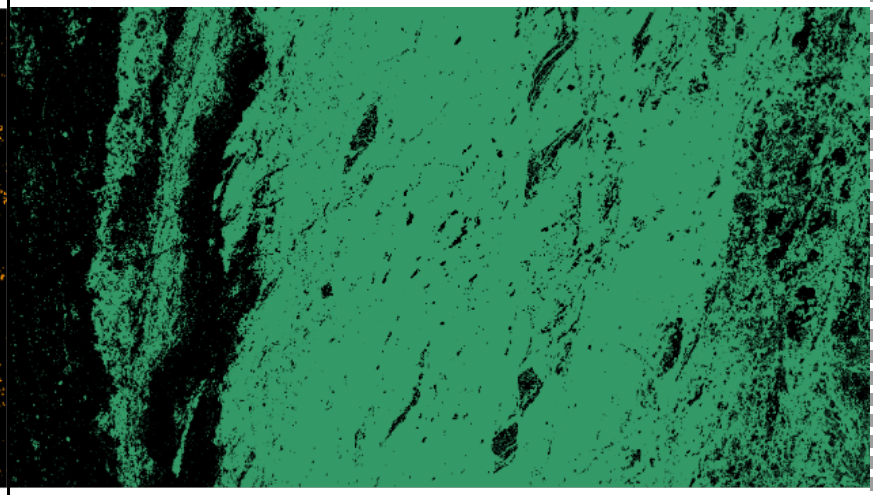
Epidote	***Violarite***
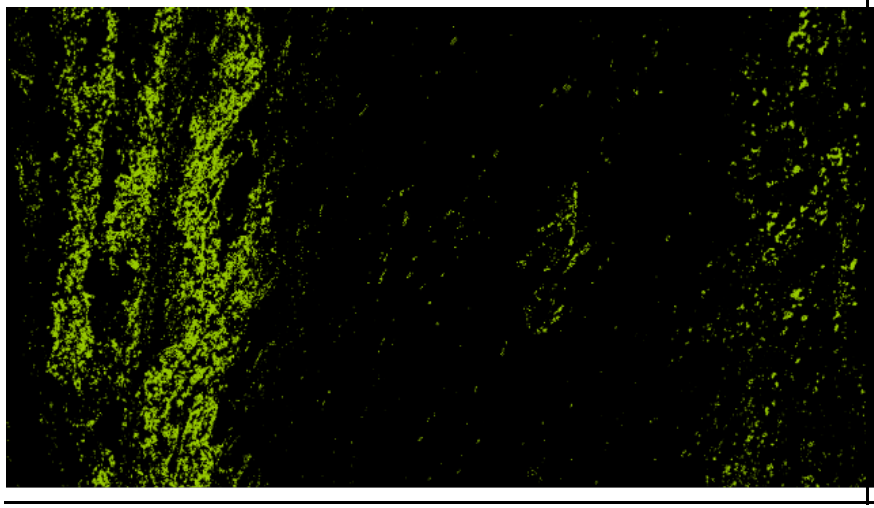	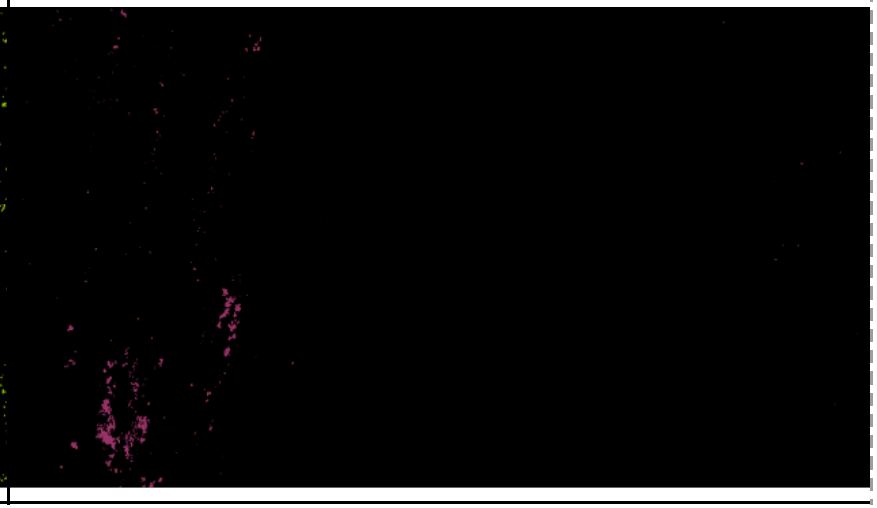

Quartz	*K-feldspar*
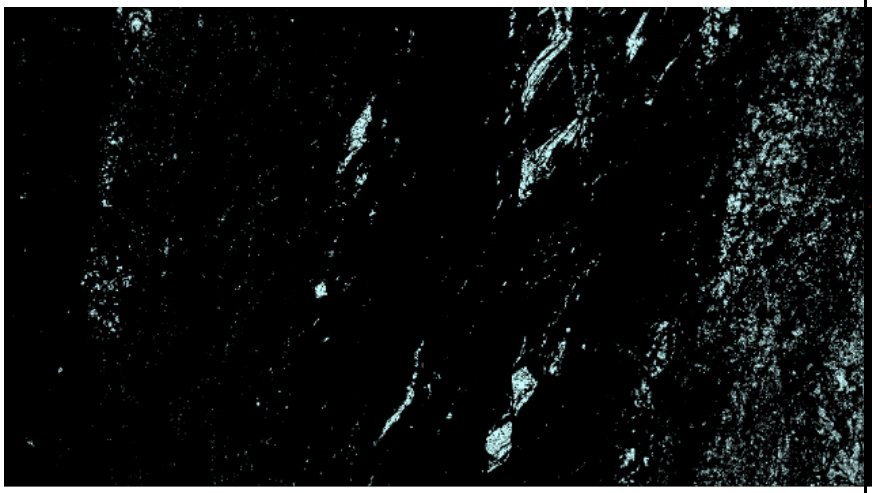	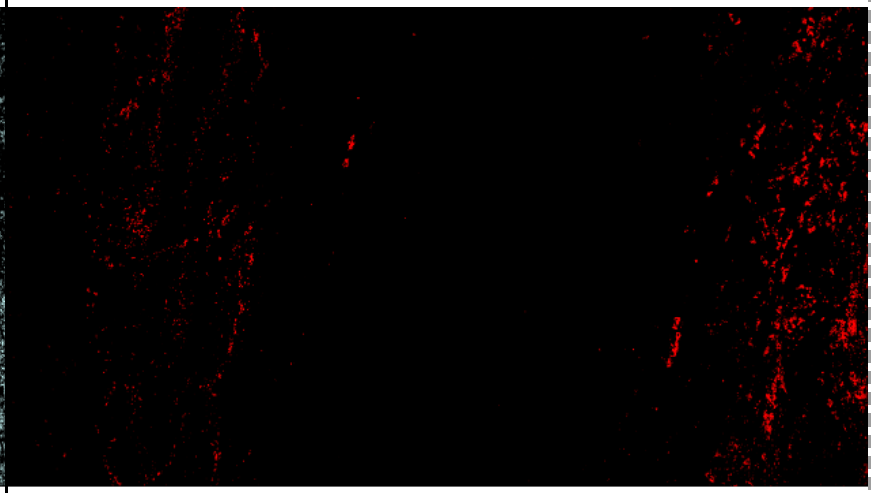
Apatite	***Titanite***
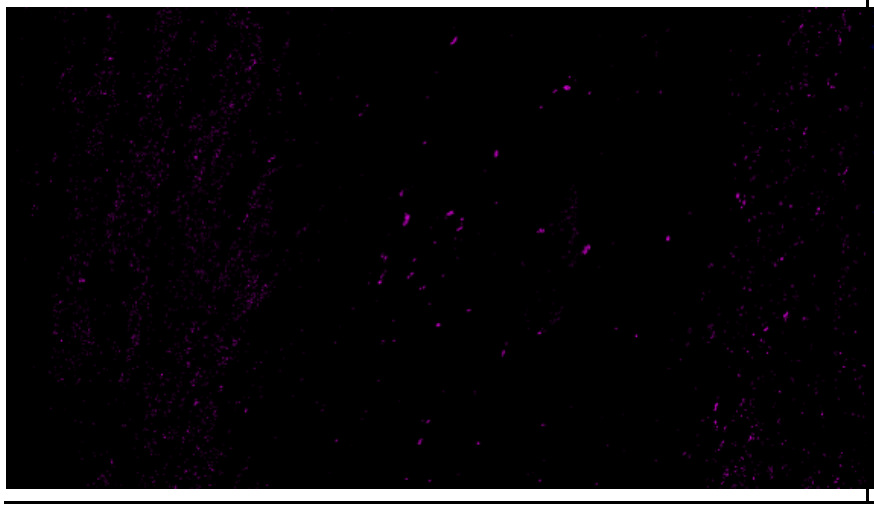	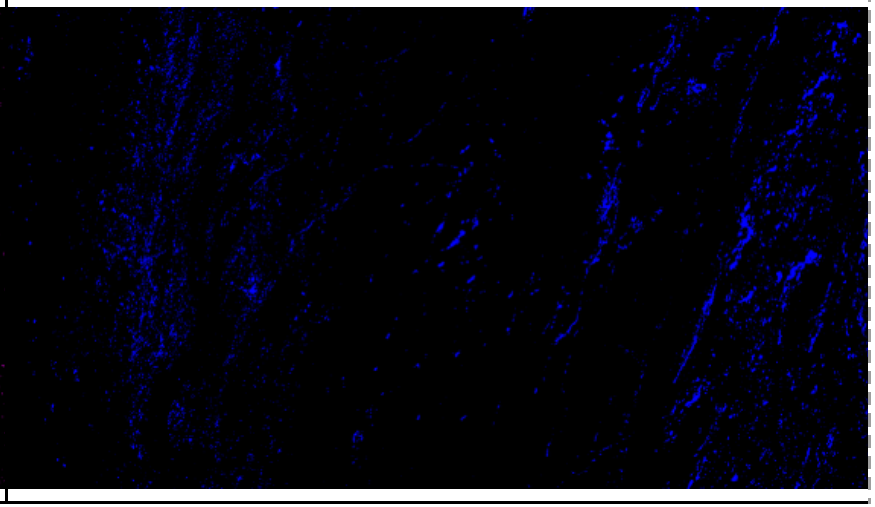

Strontium	***Calcium***
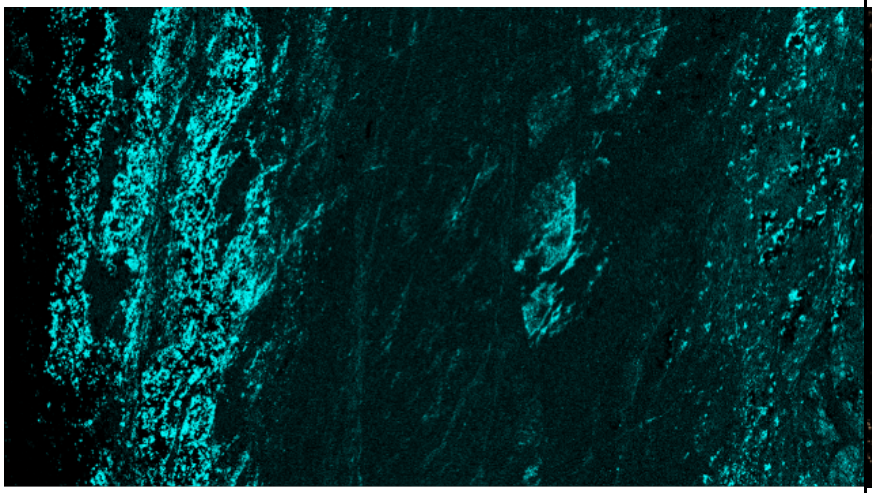	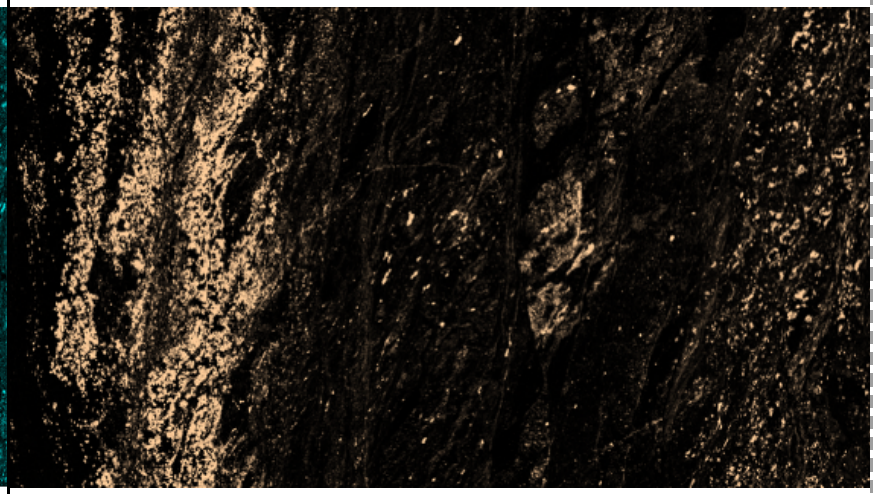
Sodium	***Titanium***
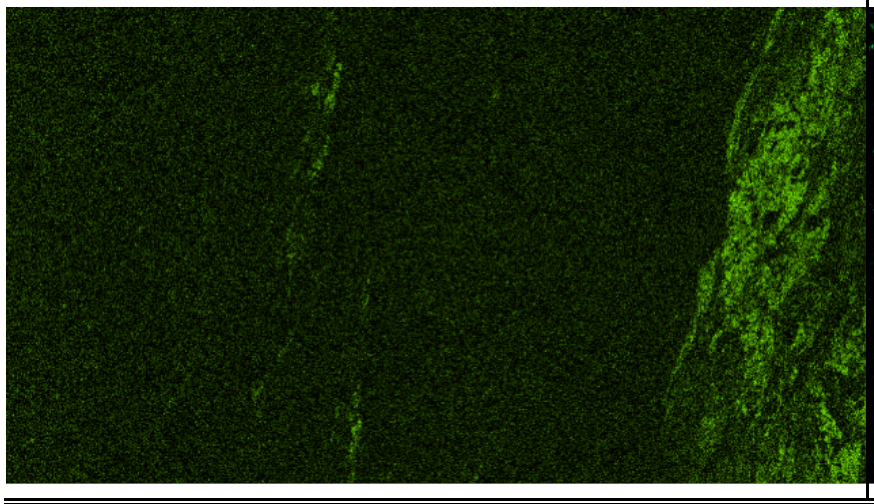	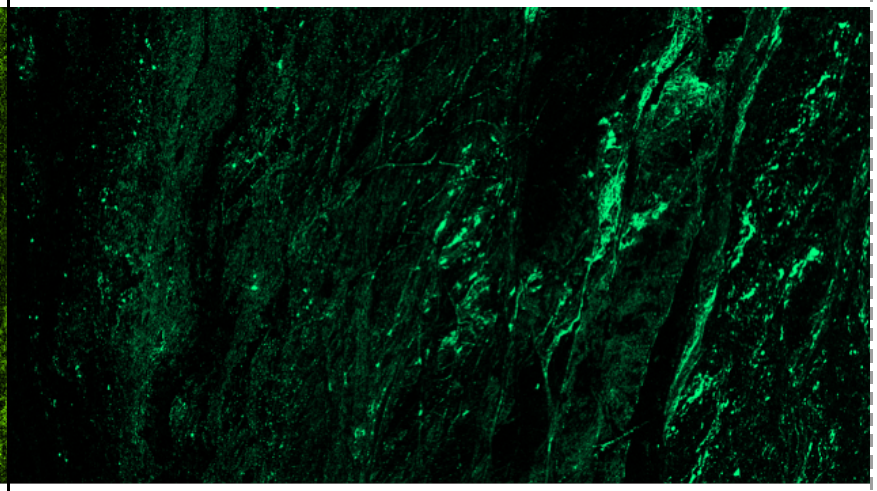

Table A10. Sulfide stable isotope analysis on chalcopyrite. Grid reference is provided.

Sample ID	Weight (mg)	Grid	cm	$\delta^{34}S$	Error (-0.3)	Error (+0.3)	%S
Upper Sulfide Transect							
P1-1	0.12	1.3	1	5.5	5.2	5.8	37.5
P1-5	0.137	1.6	2.4	4.3	4.0	4.6	38.3
P2-1	0.132	2	3.5	4.4	4.1	4.7	41.0
P2-5	0.144	2.7	5.5	4.6	4.3	4.9	35.6
P3-1	0.145	3	7	4.1	3.8	4.4	33.9
P3-4	0.147	3.8	9	4.6	4.3	4.9	33.9
P4-1	0.146	4	10	4.5	4.2	4.8	35.7
P4-4	0.138	4.9	12.3	4.6	4.3	4.9	35.6
P5-3	0.144	5.7	13.3	4.8	4.5	5.1	33.6
P6-4	0.144	6.3	14.3	4.3	4.0	4.6	29.2
P6-7	0.145	6.8	15.5	4.4	4.1	4.7	36.5
P7-3	0.151	7	16.1	2.3	2.0	2.6	20.5
P7-6	0.159	7.3	17.2	4.5	4.2	4.8	35.1
P9-2	0.146	9	23.9	4.4	4.1	4.7	35.8
Middle Sulfide Transect							
P1-2	0.131	1	0.3	4.0	3.7	4.3	25.7
P1-4	0.141	1.3	1.6	4.0	3.7	4.3	35.2
P2-2	0.144	2	4	4.4	4.1	4.7	33.2
P2-4	0.145	2.5	4.9	4.2	3.9	4.5	36.3
P3-3	0.145	3.5	7.9	4.2	3.9	4.5	30.7
P4-3	0.139	4.5	10.9	4.9	4.6	5.2	42.0
P4-5	0.144	4.9	12.1	4.7	4.4	5.0	34.0
P5-2	0.14	5	12.6	4.9	4.6	5.2	35.4
P6-2	0.147	6	13.8	4.9	4.6	5.2	33.9
P6-3	0.149	6.3	14.3	4.8	4.5	5.1	35.4
P6-6	0.143	6.6	15.1	4.3	4.0	4.6	35.1
P7-2	0.15	7	16.1	4.4	4.1	4.7	34.9
P7-5	0.155	7.3	17.2	5.2	4.9	5.5	32.7
P7-7	0.156	7.6	18.4	4.6	4.3	4.9	31.6
P8-1	0.16	8.5	22	6.0	5.7	6.3	30.3
P9-1	0.144	9	24.3	5.0	4.7	5.3	36.4
Lower Sulfide Transect							
P1-3	0.129	1	0.7	4.5	4.2	4.8	37.4
P1-6	0.13	1.8	2.8	4.2	3.9	4.5	32.7
P2-3	0.145	2	3.5	4.3	4.0	4.6	37.3
P2-6	0.139	2.9	6	4.6	4.3	4.9	37.8
P3-2	0.149	3	7	5.2	4.9	5.5	30.1
P3-5	0.143	3.8	8.8	4.1	3.8	4.4	38.2
P4-2	0.154	4	9.7	4.6	4.3	4.9	34.9
P4-6	0.145	4.75	11.5	6.0	5.7	6.3	35.5
P5-1	0.147	5.7	13.4	4.3	4.0	4.6	35.7
P6-1	0.14	6	13.9	5.2	4.9	5.5	34.8
P6-5	0.141	6.8	15.7	4.2	3.9	4.5	35.9
P7-4	0.147	7.3	17.2	4.6	4.3	4.9	29.4
P7-1	0.145	7.6	18	5.4	5.1	5.7	33.9
P8-2	0.156	8.8	23.2	5.9	5.6	6.2	35.8

Table A10 (con't). Grid location for stable isotope data.

Inner Vein

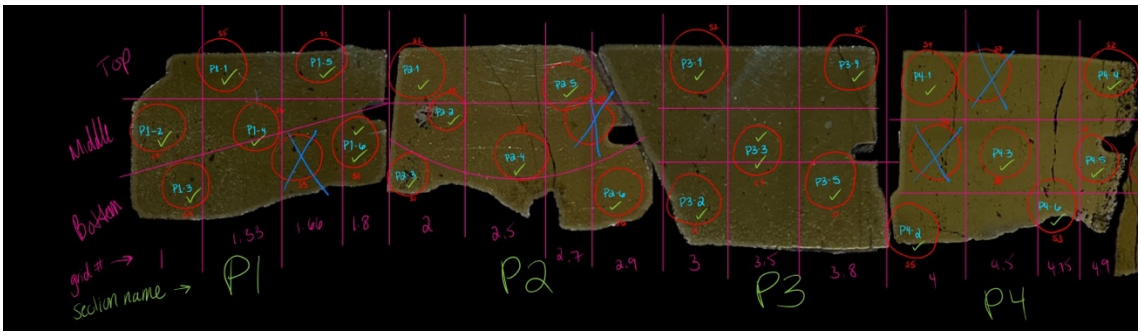

Outer Vein